Joanna Niedziółka

Preparation and properties of the electrodes modified with hydrophobic silicate film and redox liquid

Advisor: prof. dr hab. Marcin Opałło,
Department of Electrode Processes

The present dissertation was prepared within
the International Ph.D. in Chemistry Studies
at Institute of Physical Chemistry of the Polish Academy of Sciences

Warsaw 2006

This dissertation is dedicated to my Mother and the memory of my Father

„Don't accept everything even if you are not an expert"

H.W. Kroto

I wish to extend my gratitude to professor Marcin Opałło
for teaching me the meaning of those words,
as well as for being my patient guide
through the jungle that electrochemistry is.
He is an invaluable source of knowledge and inspiration.

Many grateful thanks for all help of
Dr Frank Marken
Dr Barbara Pałys
Dr hab. Robert Nowakowski

and all members of Department of Electrode Processes

This research was financially supported by Institute of Physical Chemistry, Polish Academy of Sciences, Ministry of Science and Higher Education (grant no. 3 T09A 01926), British Council and Committee for Scientific Research (Polish-British Partnership Program - project WAR/314/248) and Polish Academy of Sciences - CNRS (Project no. 16675).

Contents

Major abbreviations

AFM – atomic force microscopy

APTEOS – 3-aminopropyltriethoxysilane

bppg – basal plane pyrolytic graphite

CA – chronoamperometry

CCE – carbon ceramic electrode

CNFs – carbon nanofibres

CV – cyclic voltammetry

CVD – chemical vapor deposition

C_{10}mimN$(Tf)_2$ – 1-decyl-3-methylimidazolium bis(trifluoromethylsulfonyl)imide

C_4mimN$(Tf)_2$ – 1-butyl-3-methylimidazolium bis(trifluoromethylsulfonyl)imide

C_4mimPF_6 – 1-butyl-3-methylimidazolium hexafluorophosphate

DCE – 1,2-dichloroethane

DDPD – *N*,*N*,-didodecyl-*N'*,*N'*-diethylphenylenediamine

DmFc – decamethyferrocene

DPTPD - N^1-[4-(dihexylamino)phenyl]-N^1,N^4,N^4-trihexyl-1,4-phenylene-diamine

DPV – differential pulse voltammetry

Fc$(CH_2OH)_2$ – ferrocenedimethanol

FDAH – (ferrocenylmethyl)dimethyl(*w*-trimethoxysilyl) propylammonium hexafluorophosphate

FEGSEM – field emission gun scanning electron microscopy

Fe(III)-TPP-Cl – iron(III) tetraphenyl porphyrine chloride

FTIR – Fourier transform infrared spectroscopy

FTIRRAS – Fourier transform infrared reflection-absorption spectroscopy

HDOP - bis(2-ethylhexyl) phosphate

ITO – tin-doped indium oxide

MTMOS – methyltrimethoxysilane

MTEOS – methytriethoxysilane

MPS – (3-mercaptopropyl)trimethoxysilane

MWNTs – multi walled carbon nanotubes

NB – nitrobenzene

***n*BuFc** – *n*-butylferrocene

NPOE – 2-nitrophenyloctylether

PPA – phenylphosphonic acid

PVSA – poly(vinylsulfonic) acid

RTILs – room temperature ionic liquids

SEM – scanning electron microscopy

TBAP – tetrabutylammonium perchlorate

tBuFc – *t* -butylferrocene

TEM – transmission electron microscopy

TEOS – tetraethoxysilane

THxAP – tetrahexylammonium perchlorate

THPD – *N*,*N*,*N'*,*N'*-tetrahexylphenylene diamine

TMOS – tetramethoxysilane

TOAP – tetraoctylammonium perchlorate

SIS – bis[(3-triethoxysilyl)-propyl]tetrasulfide

SCE – saturated calomel electrode

W – tungsten electrode

Introduction

In general, all electrodes have modified surfaces. This is because of the presence of functional groups or adsorbed species from the environment e.g. air or solution. The dropping liquid metal electrode is the only exception on account of the continuously renewing drop.

The best situation is when the state of the electrode surface can be controlled. One of the first works devoted to deliberate surface modification was reported in 1973 by Hubbard. The chemisorption of functionalised olefin on platinum electrode was used to attach a variety of molecules to the electrode surface. From the electrochemical point of view immobilisation of the redox active groups was and still is the most important task. Numerous experiments were conducted to enhance their concentration on the electrode surface. For this reasons the species containing redox active groups were covalently bonded to the electrode surface or microparticles of a redox active solid were rubbed onto the electrode surface. Modification of the electrode surface with redox polymers probably represents the most frequent approach.

In 1997 Marken reported the pioneering study of pure redox liquid (redox active compound liquid at room temperature) microdroplets immobilised at the electrode surface. When it is immersed into aqueous solution a well-defined liquid|liquid boundary is formed. The lack of electrolyte in the oil phase requires the process to start at the three phase junction: electrode|redox liquid|aqueous solution. During the electrooxidation/reduction of redox liquid droplets electrogenerated ions are formed. To maintain the electrical neutrality of the organic phase two processes can occur: the transfer of charged product from the organic phase into the aqueous solution or/and insertion of the counterion from the aqueous solution into the organic phase. Their contribution to the overall electrode process depends on the hydrophobic properties of the redox liquid droplets and lipophilic properties of the counterions. Since 1997 numerous redox liquid modified electrodes were reported and much effort was devoted to the understanding of their electrochemical properties. Obviously, the efficiency of their electrode process depends on the length of three phase junction: electrode|redox liquid|aqueous solution. Therefore the development of suitable electrode support is highly desirable.

Electrodes modified with a thin porous film have attracted a lot of interest recently. This is because of the shorter path length for diffusion and therefore fast

electrochemical response. The silicates are one of the possible candidates for modification. Over the past 10 years, considerable effort has been placed in the development and study of silicate thin films fabricated by the sol-gel process as a host matrix for encapsulation of various substances including redox active molecules. From this point of view silica based materials are attractive because of their chemically inert nature and relative ease of preparation. Moreover, the presence of a micro- and meso-porous matrix opens up the possibility to prepare an electrode with a very high specific surface area, for example for sensing applications and for the immobilisation of biological redox systems. However, no attempts of organic liquid immobilisation within hydrophobic silicate film, being stable, when immersed into the aqueous solution were reported. Therefore the main goal of this work was preparation of the electrode modified with a hydrophobic thin film and investigations of their electrochemical properties after redox liquid immobilisation.

1. Literature review

1.1. Silicate films

Recently sol-gel processed silicate based hybrid materials attracted a lot of interest, because they can be employed as matrices for a large variety of functional molecules, molecular assemblies or biologically active substances [1]. The sol-gel process consists of hydrolysis, condensation and polycondensation reactions. Controlling of the reactions parameters allows to change the properties of the fabricated material [1,2]. Also the availability of numerous organoalkoxysilanes contributes to their features. These include pore size and pores distribution, density, transparency and hydrophobic or hydrophilic properties. Using the sol-gel method the formation of various forms of silicate like monoliths, powders, films and fibres in mild conditions is also possible [3].

The silicates can be divided into two groups: class I is characterised by weak interaction between the organic and inorganic components via hydrogen bonding, van der Waals or electrostatic forces and class II where organic and inorganic components are linked through strong covalent, iono-covalent or Lewis acid-base chemical bonds [4]. The latter materials are characterised by high porosity and large surface area with a number of functional groups accessible to external reagents.

The rigid silicate can act as a host matrix for numerous chemical or biological compounds. Moreover, inorganic-organic hybrids offer several advantages including photochemical, thermal and chemical stability, high abrasion resistivity, negligible swelling in aqueous and organic solutions, high biodegradational stability, excellent optical transparency and low intrinsic fluorescence [5]. These materials are useful for optical [6, 7], amperometric [8,9,10] and bio- [11,12] sensors, chromatography [13,14], power sources [15,16] and solid electrolytes [15,17,18], electrochromic devices [19], catalysis [20] or solid/liquid extraction [1,21]. They were also applied as dielectric materials [22] and protective layers against corrosion [23]. These new generation of hybrid materials opens the way of number applications like separation devices, coatings or photovoltaic fuel and solar cells [24].

Among numerous forms of silicate hybrid materials, herein special attention is devoted to thin films. Both homogenous and tailored inhomogeneous film can be formed applying the sol-gel process. The possibilities of such electrode surface modification [25] will be explored in this thesis. Further deposition of redox liquid on

the modified substrate gives the opportunity to create a new electrochemical system: electrode | thin film | redox liquid with unusual electrochemical properties.

In this chapter firstly, the properties of the silicate film will be presented and next the electrochemical behaviour of such a new system.

1.2. Sol-gel process

Among the numerous parameters affecting the sol-gel process only the most important from the point of view of this work will be presented below.

Silicon is the second most abundant element on the earth. It exists in many natural compounds like silicon dioxide, which is the main component of sand and glass. In 1824 Andrianov synthesised silicon tetrachloride [26] which was used by Ebelmen in 1845 to obtain tetraethoxysilane (TEOS) [27]. The hydrolysis of silicon tetrachloride yielded silicone tetrahydroxide. This compound undergoes condensation to form high-molecular weight polysiloxanes, which was discovered by Mendeleyev in 1850 [28,29]. The details about the sol-gel process, including parameters describing the mechanism of hydrolysis and condensation reactions, were elucidated in more details in the 1980's [29]. Metal or metalloid elements surrounded by various ligands are typical precursors applied in the sol-gel process. The most popular are inorganic metal salts such as nitrates, borates or metal alkoxides $M(OR)_x$ where M is e.g. Ti, V, Sn or Al. Nevertheless, the silicon alkoxides are the most commonly used precursors to obtain inorganic-organic hybrid materials [29]. Some of them were employed in this work for thin film preparation. For this reason the literature presented below will be limited to films obtained from silicon alkoxides.

As was said above, the sol-gel process consists of hydrolysis, condensation and polycondensation. After ageing, drying – solvent evaporation and densification the sol-gel materials are obtained (Fig.1). Their properties strongly depend on the conditions of these processes [3].

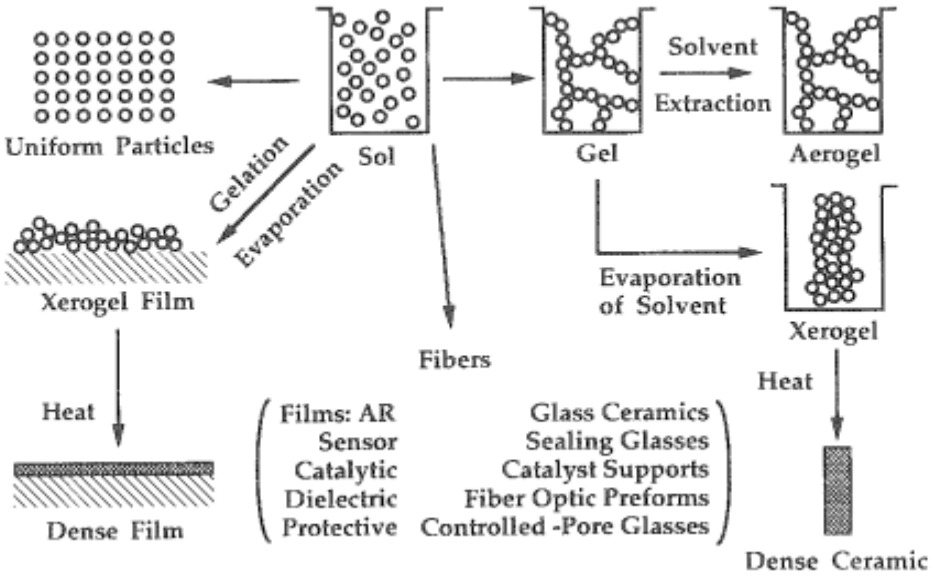

Fig.1. Scheme of sol-gel technology and its products [29].

First, colloidal particles of the silicon alkoxide precursor are suspended in a solvent (water, alcohol or their mixture) to prepare the appropriate sol. These particles should be bigger than 1 nm to demonstrate the Tyndall effect and smaller than 100 nm to prevent sedimentation [30]. Next, the acid or base catalysed hydrolysis takes place and is followed by the condensation. The rate of the hydrolysis depends on the type of catalyst [3] and precursor due to electronic and steric effects [31]. It is also affected by the type of solvent or ratio of water to co-solvent content because of hydrophobic/hydrophilic properties of the precursor [3] and solution pH.

acid hydrolysis (1)

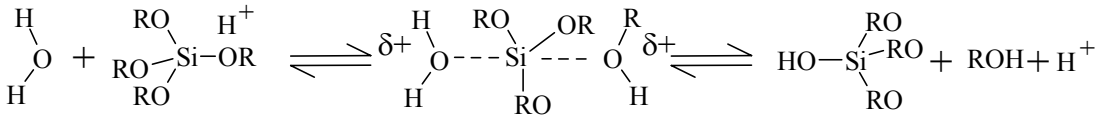

base hydrolysis (2)

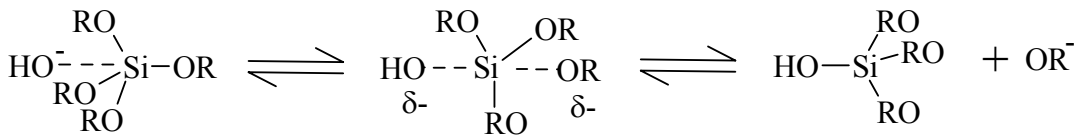

In the acid hydrolysis the positively-charged transition state is stabilised by electron donating groups. For this reason only the first protonation of silanol group is fast. Then the hydrolysis slows down. The replacement of alkoxy groups by hydroxyl ones causes decrease of electrodonicity of the silicon substituent. This is the reason why linear and later only a partially cross-linked network is formed. The obtained material has a relatively dense structure and small pores [3]. In base hydrolysis the negatively-charged transition state is stabilised by hydroxyl groups. After removing the first silanol group the reaction goes faster. A much more cross-linked network with numerous defects and bigger size pores is formed in the base catalysed process [3].

The condensation reaction of hydrolysed alkoxide molecules is the second step of the sol-gel process. It is followed by the gelation process, which consists of further condensation with entrapping of the remaining solution. At this stage a gel is formed. It can be defined as "a porous 3-dimensionally interconnected solid network that expands in a stable fashion throughout a liquid medium and is only limited by the size of container" [32]. Next, the ageing process take place. At this stage the structural evolution occurs, including changes of the pores shape and size. Then during the drying step two routes are possible: solvent extraction, which leads to aerogel formation, or evaporation of the solvents and volatile components with a following collapse of the material structure resulting in a xerogel [3,29]. This can be followed by densification through heat treatment in a final step to provide dense ceramics [3,29].

One can point out the advantages of the sol-gel process. In this way a large number of silicate based materials can be obtained under mild temperature conditions. Appropriate selection of precursors with different properties leads to production of high purity silicates with special properties, like e.g. porosity, and transparency. The functionalisation of the final product can be also achieved by the sol-gel process [33]. Since the reaction occurs at ambient temperature and low pressure there is no risk of organic substituent decomposition. The sol-gel process also brings some drawbacks, like time consumption, change of material volume in time caused by ageing and drying and it is not resistant to cracking.

1.3. Film preparation

Herein the most important information about thin film preparation methods is presented. During their sol-gel processing the drying stresses, like cracking can be easily overcame [32]. Moreover, the pore volume (0 - 65%), pore size (0.4 nm - 5.0

nm), surface area (1 - 250 m^2/g) and thickness (50 - 200 nm) can be precisely controlled by appropriate preparation methods [29,34]. These materials are transparent to visible light and can transmit, absorb, reflect radiation with a given wavelength. The films are chemically resistive and can act as abarrier against corrosion, oxidation, abrasion or scratching [32]. They can be obtained by dipping, spinning, electrodeposition, spraying, sputtering, screen-printing as well as electrophoretic and thermophoretic, chemical vapour or sol-drop deposition [29].

Dip-coating

The principle of this method is to dip the substrate material in a sol solution and then pull it out. Careful control of the rate of this process is necessary to obtain reproducible samples. The five steps of this process, immersion, start-up, deposition, drainage and evaporation, as demonstrated in Fig. 2 [29], were pointed out by Scriven [35]. The deposition seems to be the most important. While the substrate is removed from the sol solution the inner layer of the deposit remain on its surface and the outer layer goes back into the solution. Film thickness and other properties depend on "the viscous drag upward on the liquid by the moving substrate, force of gravity, resultant force of surface tension in the concavely curved meniscus, internal force of the boundary layer liquid arriving at the deposition region, surface tension gradient and the disjoining or conjoining pressure" [29].

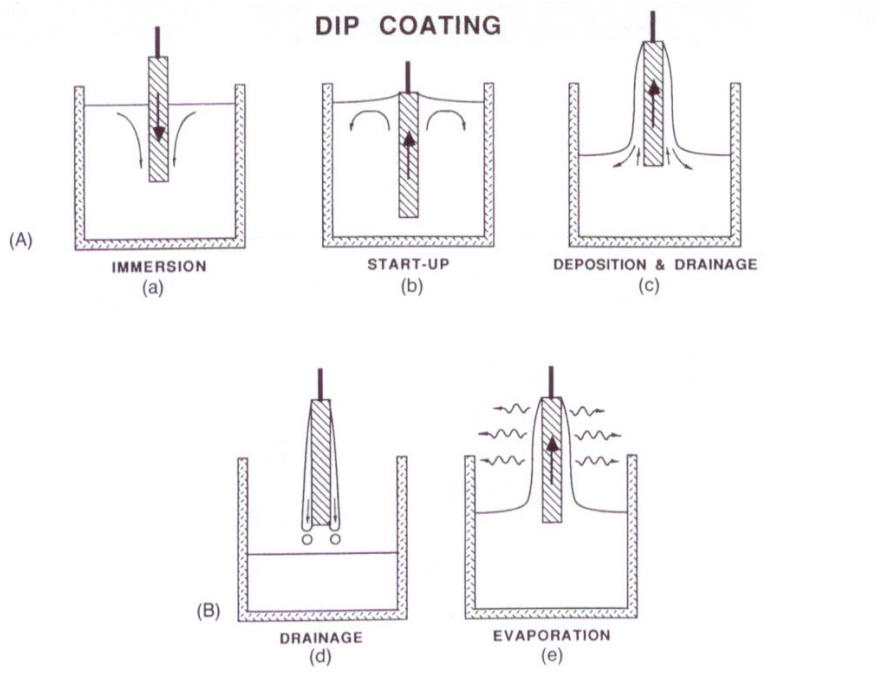

Fig.2. Stages of the dip coating process [29].

Next, elimination of the solvent is realised by evaporation. The rate of this process depends on the diffusion of the vapour away from the film surface, sol concentration and withdrawal speed. This method was employed in this work for some electrodes.

Spin-coating

This method relies on the spreading of sol solution on a rotating substrate. It consists of deposition, spin-up, spin-off and evaporation steps (Fig.3.) [29]. First, a small amount of liquid precursor solution is placed on the surface. Next, when the sample is rotated, the sol is spread radially outwards and approaches the perimeter to finally leave the excess in the form of droplets. This method allows to obtain an uniform film thickness depending on the volume of stock sol, speed rate of spin coating and centrifugal force and rate of evaporation.

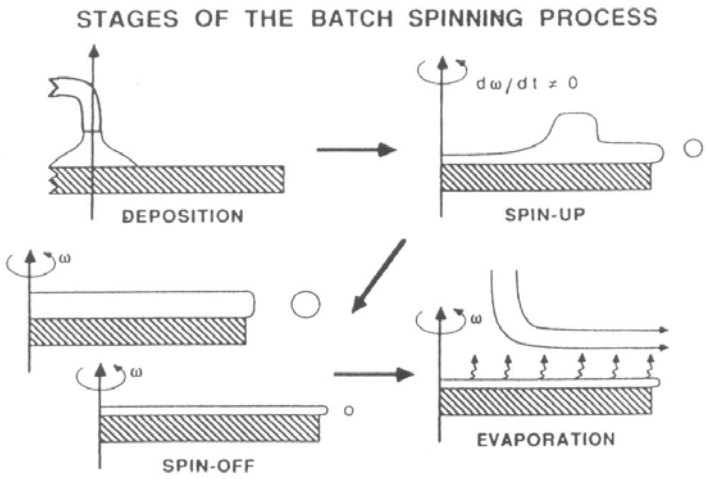

Fig.3. Stages of the spin-coating process [29].

Electrodeposition

The principle of the conventional electrodeposition process is the electroreduction of metal ions on a negatively charged substrate. Application of this method for silicate film preparation is impossible because silicon alkoxides are not electroactive. However, electrogeneration of catalysts can be employed for sol-gel film formation [36]. This can be done by applying a constant negative potential to an electrode immersed into the sol. In this way OH^- anions are produced by electroreduction of water molecules:

$$H_2O + e \rightarrow OH^- + 1/2\ H_2 \qquad (1)$$

This results in a local pH increase and the sol-gel process is accelerated near the electrode surface [36]. The film thickness depends on the applied potential and the type of the electrode material. For example, the growth of methyltrimethoxysilane (MTMOS) based matrix was observed with an increase of the negative potential on a tin-doped indium oxide (ITO) electrode [36]. Moreover, the film wettability can be also changed by the shift of the applied potential, e.g. the more negative potential applied the more hydrophobic surface is obtained. The wettability decreases when the thickness and roughness of the film increases, because the surface becomes more hydrophobic. Compared to bare ITO the MTMOS modified electrode exhibits smaller wettability. This result is important from the point of view of this work. It demonstrates that the presence of MTMOS matrix at the electrode changes its properties and its surface becomes hydrophobic [36].

Sol-drop deposition

The sol-drop deposition is one of the easiest methods to obtain the silicate film [37,38], because it dose not require any special equipment. After hydrolysis of the suspended precursor particles within a volatile solvent, the determined volume of sol is caste onto the substrate material. It is followed by a condensation and evaporation process and finally a sol-gel film is obtained. The thickness of the film depends on the volume of deposited liquid while the porosity depends on the type of precursors and the rate of evaporation. These films are less uniform than those obtained by dip or spin-coating. This method was also used in this work for electrode modification.

Spray-coating

In this technique the sol solution is sprayed onto the substrate material [39]. The obtained film is less uniform than those prepared by the dip or spin-coating methods.

Chemical vapour deposition

This method involves deposition a thin film from gaseous phase. The precursor is delivered into the reactor chamber and after heat treatment the formed vapours are caste onto the substrate material. The by-products are removed by gas flow. To limit decomposition occurring at high temperatures in conventional chemical vapour deposition (CVD) atmospheric pressure [40], low pressure, laser or plasma enhanced

CVD can be used. The last technique is also useful for thin organic-inorganic silicate film preparation [41].

Electrophoretic deposition

This technique utilizes an external electric field gradient. The charged species present in the sol solution are driven by the external potential difference flow. The film is deposited on the cathode or the anode (Fig.4). The film thickness, pore volume, surface area and pore size depends on the applied electric field, the particles charge and the duration of the experiment. The film thickness increases with deposition time and the density and hardness of the film is much higher than in the case of a dip-coated film [29].

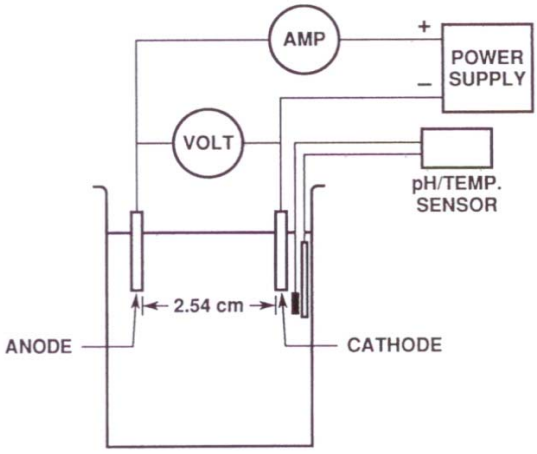

Fig.4. Scheme of an electrophoretic coating cell [29].

Thermophoretic deposition

In the thermophoretic method of film preparation a thermal gradient is used to move the particles suspended in the sol solution. The species are forced in the direction of lower temperature. Contrary to the electrophoretic method, thermophoresis does not require electrically conductive substrates [29].

Screen-printing

The sol solution is spread on the substrate material by a screen-printer and a film with well-defined shape is obtained. This method offers the possibility to obtain thicker films [42] than by the techniques described above.

It has to be emphasised, that careful selection of the method allows to obtain film with required structures. In most cases an overlap of the deposition and drying stages takes place. Also competition between evaporation responsible for film compactness and continuous condensation reactions, which stiffen the film, occurs. This influences the film porosity. Moreover, pH plays important role during the film formation as it affects the condensation rate. A decrease of the pH reduces the condensation rate during deposition and drying causing a decrease of the film porosity [29].

1.4. Film properties

The sol-gel process belongs to the "soft-chemistry", because of the mild conditions that allows obtaining inorganic-organic hybrid films at the nanometric scale [29,34,43]. Knowing the principles of this process and by changing the suitable parameters, different materials can be obtained. Below, the most important chemical and physical properties of silicate films and the way they can be controlled are presented.

1.4.1. Porosity

Porosity is the one of the most important properties of the silicate film which can be tailored during the sol-gel process. The porous materials are classified into the three main categories, depending on their pore diameter (d), as micro- ($d < 2$ nm), meso- (2 nm $< d >$ 50 nm) or macroporous ($d > 50$ nm) [44]. It is well known that silica solids are mesoporous [45]. Strategies for creating hierarchically organised and designed structures of porous hybrid materials were recently elaborated by Sanchez [46,47]. This helps in the development of well-organised mesostructures of thin films [33,48,49]. An ordered periodic porous matrix can be obtained by the sol-gel process in the presence of a surfactant as a template. After its removal, a regular three-dimensional structure is created with well-defined pore size. Embedding liquid crystalline phases [50] or nanocrystals [51] are also possible ways to synthesise ordered mesoporous structure films.

The physico-chemical properties of ordered periodic films can be tuned by pre- [52,53,54] or post-functionalisation [55,56,57] routes. The first method employs functional alkoxides, the latter grafting after film formation. The pore properties such as hydrophobicity, polarity, catalytic, optical and electronic activity depend on functional groups attached into the alkoxide precursor [58,59,60].

The final form of the periodic mesoporous silicate materials depends on cooperative organisation of inorganic and organic components into the three-dimensional structure. Different morphologies can be obtained by changing the acid concentration, which influences the rate of the hydrolysis and condensation steps. It was elucidated that only in precisely defined range of acid concentration a high-quality microporous [61] or mesoporous material can be obtained [61,62].

An example of the significant differences in TEOS based film topography when prepared in different ways is presented in Fig.5 [63]. The gradual transition from a relatively dense and smooth film obtained from acid hydrolysed sol to a rough one obtained from base hydrolysed sol can be observed [63].

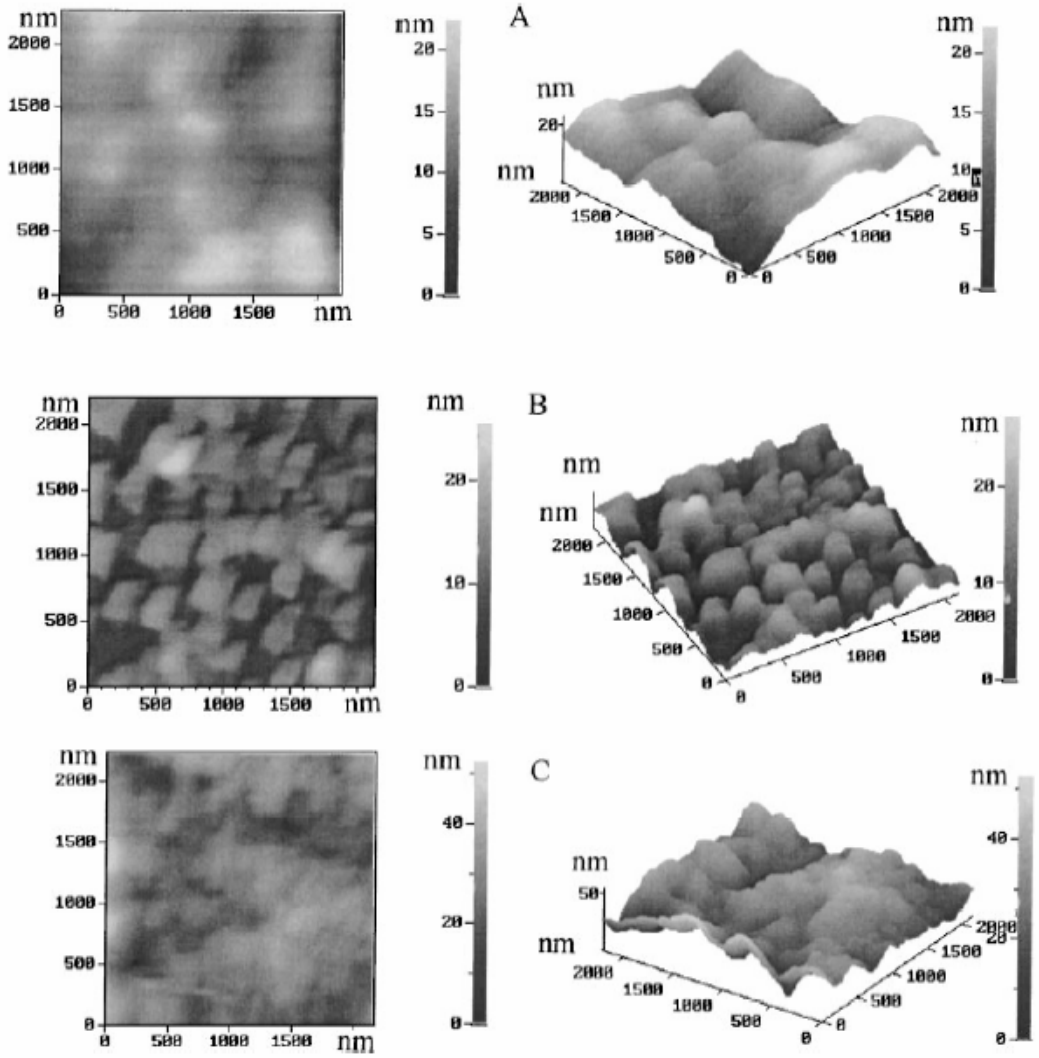

Fig.5. Atomic force microscopy (AFM) images of the TEOS based films, obtained by (A) acid, (B) base catalysis, (C) base/acid [63].

The organisation of nanostructured mesoporous silicate films depends on the surfactant concentration [64,65]. Changing the ratio of silicate precursor to non-ionic surfactant allows obtaining films with cubic, hexagonal or lamellar structure. The porosity and pore size of mesoporous silicate films can be also tailored by the ratio of hydrophilic TEOS to hydrophobic methyltriethoxysilane (MTEOS) precursor. When decreasing this factor a more porous film with bigger pore size was obtained [66] (Fig.6, 7).

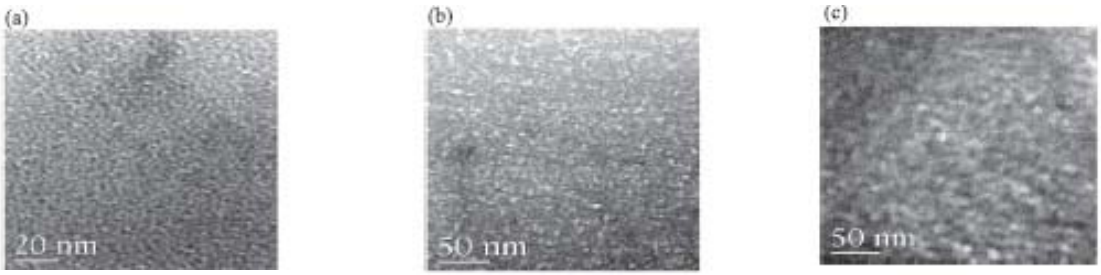

Fig.6. Transmission Electron Microscopy (TEM)images of the microstructure of films obtained using different ratio of precursors (a) TEOS/MTEOS = 2.0 (b) TEOS/MTEOS = 1.0 (c) TEOS/MTEOS = 0.5 [66].

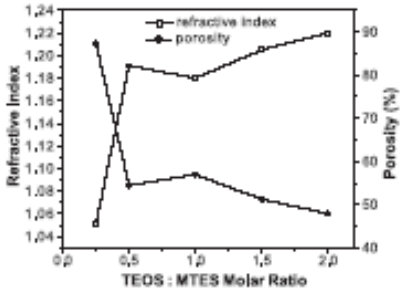

Fig.7. The refractive index and porosity of the films as a function of TEOS:MTEOS molar ratio [66].

The MTMOS based film structure may strongly depend on the hydrolysis time [67] (Fig.8). With its increase the transition from a macroscopically flat morphology with submicrometer sized pores to a film rich in narrow sized internal macropores was observed and their size gradually decrease with time. The withdrawal speed (Fig.9) also influences the film morphology. Its enhancement increases the film thickness. From a macroscopically flat film it also becomes internally rich in macropores.

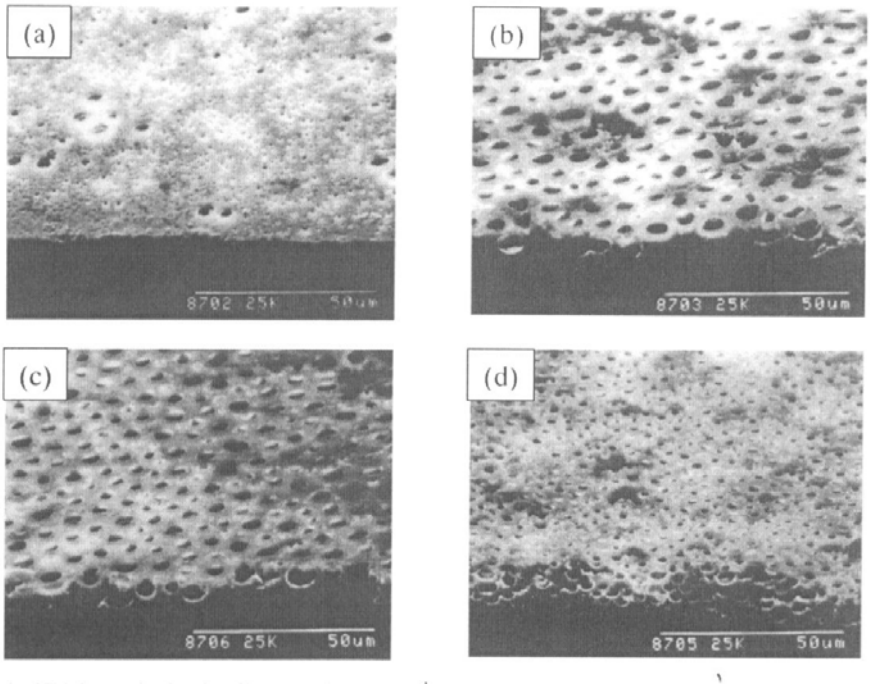

Fig.8. Scanning electron microscopy (SEM) images of resultant MTMOS films prepared at 2 cm min^{-1}; reaction times of the coating solution are (a) 210, (b) 215, (c) 220, (d) 225 min. View angle is 60° [67].

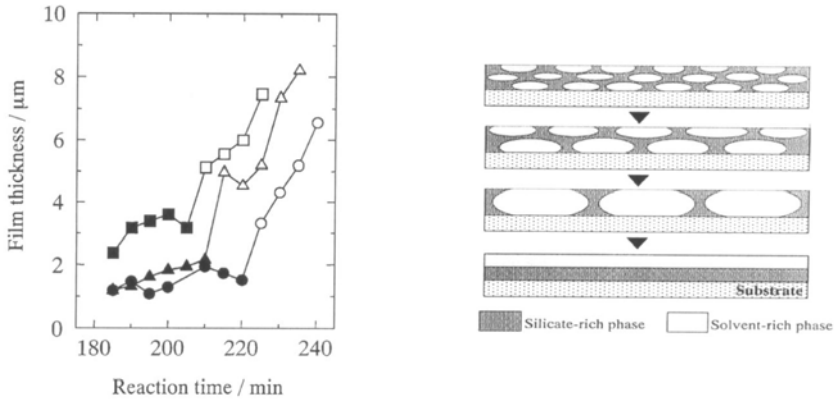

Fig.9. Dependence of MTMOS film thickness on reaction time and withdrawal speed; ○ ● 1 cm min $^{-1}$, Δ ▲ 2 cm min $^{-1}$, □ ■ 4 cm min $^{-1}$. The closed and open symbols denote macroscopically flat and macroporous morphologies respectively (left side). Schematic model of the coarsening of phase separating domains (right side) [67].

Besides changing the ratio of sol ingredients also the method of film preparation affects film porosity and topography. For example when comparing films based on TMOS precursor electrodeposited or spin-coated on a glassy carbon surface significant differences are observed (Fig.10) [68]. Numerous protrusions randomly distributed within the matrix are present in the electrodeposited film formed from base-catalysed sol. The authors suggest that aggregates of particles are formed. The differences

between the film structure obtained by the electrodeposition and spin-coating method results from the formation process. In the latter case a competition between evaporation and continuous condensation takes place, whereas during electrodeposition only gelation occurs. A smoother surface was obtained by spin-coating. As mentioned above, similar differences of surface topography can be obtained by going from base to acid catalysis. A more compact, smoother and denser matrix with low pore volume was prepared from acid catalysed sol. This results from the nature of the hydrolysis process where in acidic conditions mainly linear silicate chains are formed.

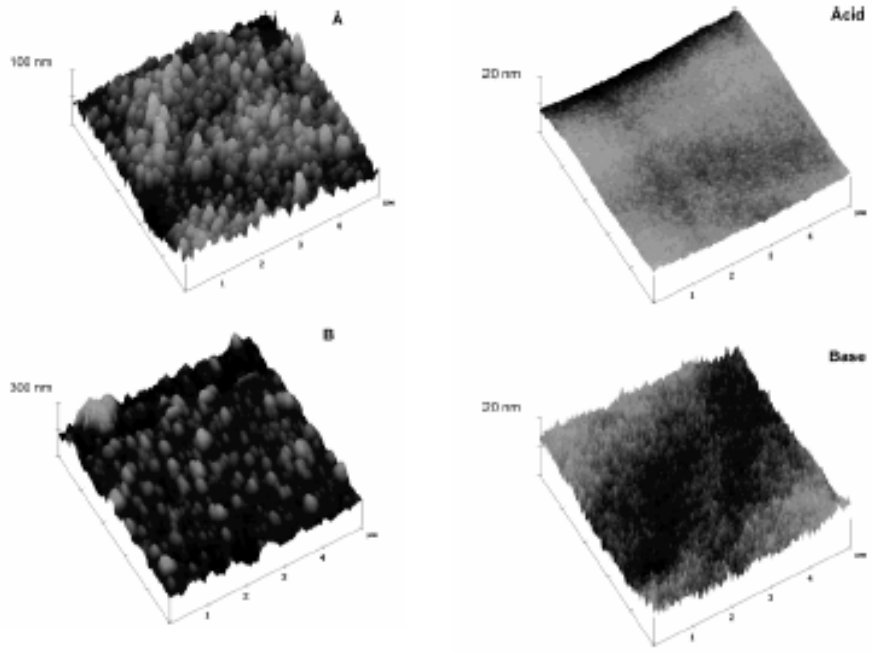

Fig.10. AFM images of a TMOS based film (A, blue/brown film; B, blue/yellow film) electrodeposited on a glassy carbon electrode (left side) or spin-cast from an acid- or base-catalysed sol (right side) [68].

A macroporous silicate film can be created by templated synthesis in the presence of large micrometer size particles (Fig.11). For example suspended polystyrene latex spheres can be used as templates. After gelation they are removed by dissolution in an organic solvent [69]. In this way uniform pore size with dimensions defined by the diameter of spheres is obtained. The removal of the template and exposure of the support was confirmed by the successful electrodeposition of metal. The film porosity can be controlled by the microspheres size and their concentration in the sol.

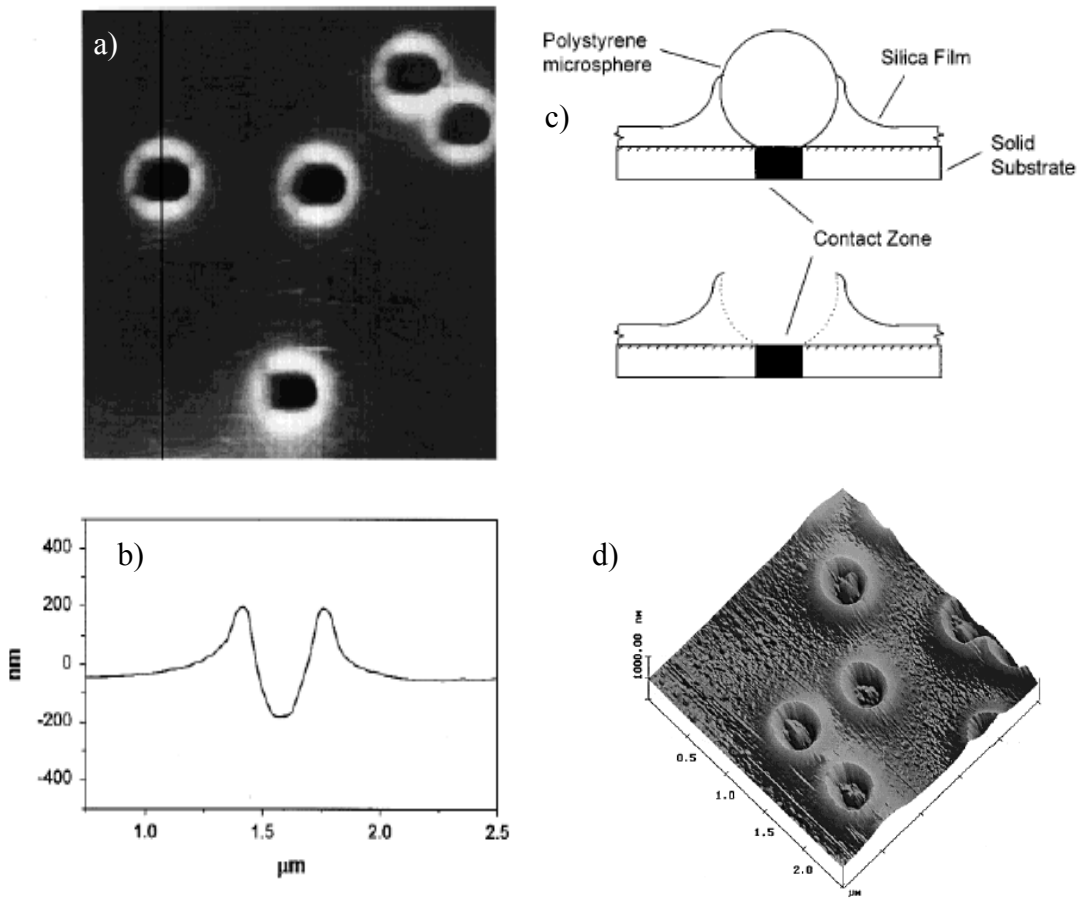

Fig.11. a) AFM image, b) cross section view of a single hole in a silicate film prepared from sol containing 0.5 µm polystyrene microspheres after chloroform treatment, c) schematic representation of the templating of a silica film with polystyrene, d) AFM image of silicate film after copper electrodeposition [69].

The number of pores can be increased by up to two orders of magnitude by packing the spheres in a closely packed array [70,71] (Fig.12). This is because the polystyrene latex microspheres arrange in a hexagonal close-packed array independently of particles size or water content into a sol solution [71] (Fig.13, 14) It should be mentioned, that except microsphere size also the sol concentration influences the matrix porosity.

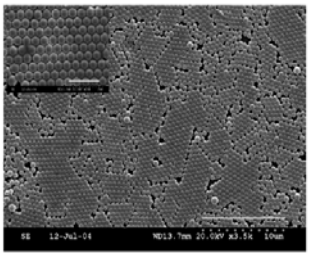

Fig.12. SEM image of 500 nm diameter latex spheres embedded in a silicate film on glassy carbon substrate [71].

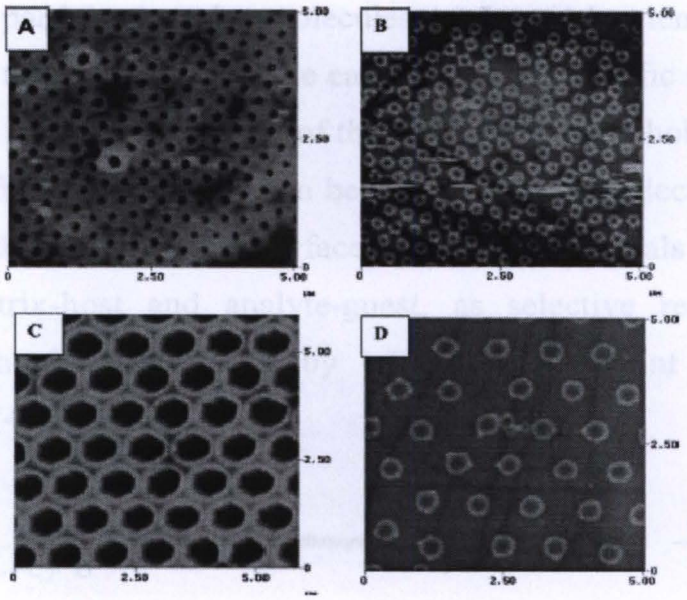

Fig.13. AFM images of the cavities formed in a silicate film after the 300 nm diameter (A,B) and the 1000 nm diameter (C,D) spheres were removed from the film [71].

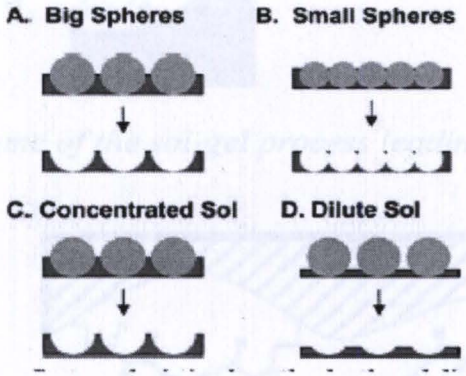

Fig.14. Cartoon depicting how the depth and diameter of the cavities can changed by varying the size of the template and/or the sol composition [71].

One of the novel methods of porous silicate film fabrication is electrodeposition from a sol containing uniform discrete nanoparticles, e.g. Ludox colloidal silica 7-22 nm in diameter [72], stabilised at high pH. This sol is stable because negatively charged silica particles exhibit electrostatic repulsion at high pH. A film with thickness around 300 nm can be deposited by decreasing the sol pH. The electrooxidation of H_2O_2 causes the generation of H^+ in the vicinity of the electrode surface, which destabilises the silica sol, thus causing its deposition on the electrode surface, according to the reaction below:

$$H_2O_2 \rightarrow O_2 + 2H^+ + 2e \qquad (2)$$

Not only particles but also molecules can be used as templates in the sol-gel process [1,73]. After template removal the cavities having specific shape and size are present in the film (Fig.15). The properties of their walls as hydrophobicity, hydrophilicity and the presence of functional groups can be also tuned. The selective adsorption of molecules depends on the specific pore surface [73]. Such materials show host-guest interaction between matrix-host and analyte-guest, as selective recognition, sodium salts of phenylphosphonic acid (PPA) by one-point, two-point or non-specific host-guest interaction [74] (Fig.15).

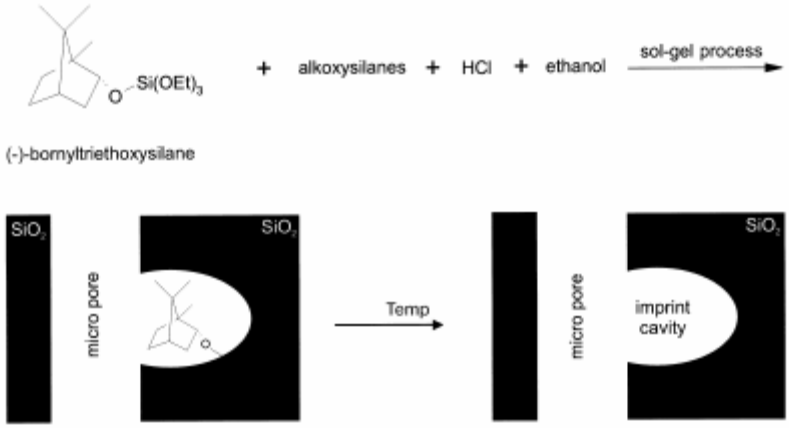

Fig.15. Scheme of the sol-gel process leading to imprinted porous materials [73].

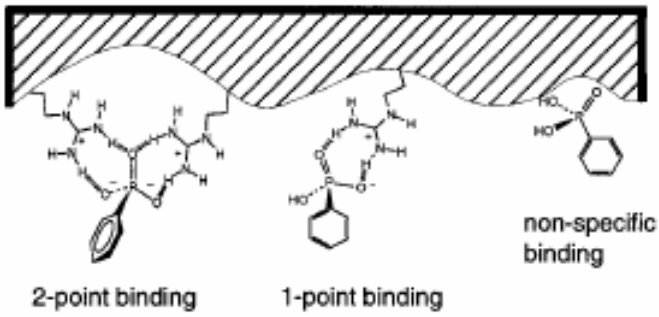

Fig.16. Scheme of the various binding models of PPA to functionalised xerogel surface [74].

The thin film lets the analyte freely diffuse in and out of the matrix because of its thickness and porosity [2]. Due to the combined effects of porosity, hydrophobicity/hydrophylicity and electrostatic repulsion even the low symmetry, flat and compact molecules, like dopamine can be selectively recognised in the solution [75,76]. Recently the imprinting method was even used for the preparation of enantioselective sol-gel processed silicate matrix materials [77].

The sol-gel silicate films are rigid. To make them more flexible a polymer component can be added [78]. However, with increasing polymer content such materials loose their porosity and roughness.

1.4.2. Stability

The mechanical stability of the silicate film deposited on a substrate depends on its adhesion to the support, the method the matrix was obtained and other conditions, like relative humidity or time of drying [29,79,80].

It is already known that preparation of silicate thin films with thickness below 1 μm allows to quickly obtaining well-adhered crack free films [29].

The used catalyst influences the film stability [63]. For example TEOS based films obtained from base hydrolysed sol has very poor abrasion-resistance on silicon wafer, because the matrix is only physically adsorbed to the surface. On the other hand the film prepared via acid catalysis exhibits excellent mechanical properties, because it is anchored to the silicone wafer by Si-O-Si bonds.

The stability of the silicate thin film in solution depends on relative humidity and time of drying during preparation [79] (Fig.17). The films dried for 48 h at 25% humidity stays at the electrode surface for several days, whereas those dried at 75% humidity for 3 h peel off from the electrode surface within 24 h. The immersion time also affects the quality of the film. The initially compact and dense TMOS based matrix dried at 50% relative humidity for 12 hours, changed its topography after it was placed into electrolyte solution. Over an extended period of time the film surface becomes more rough, which is confirmed by electrochemical experiments. An increase of the sigmoidal voltammetric response, typical for ultramicroelectrodes, indicates the formation of holes in the film, allowing the redox probe to be transported directly to the electrically conductive surface.

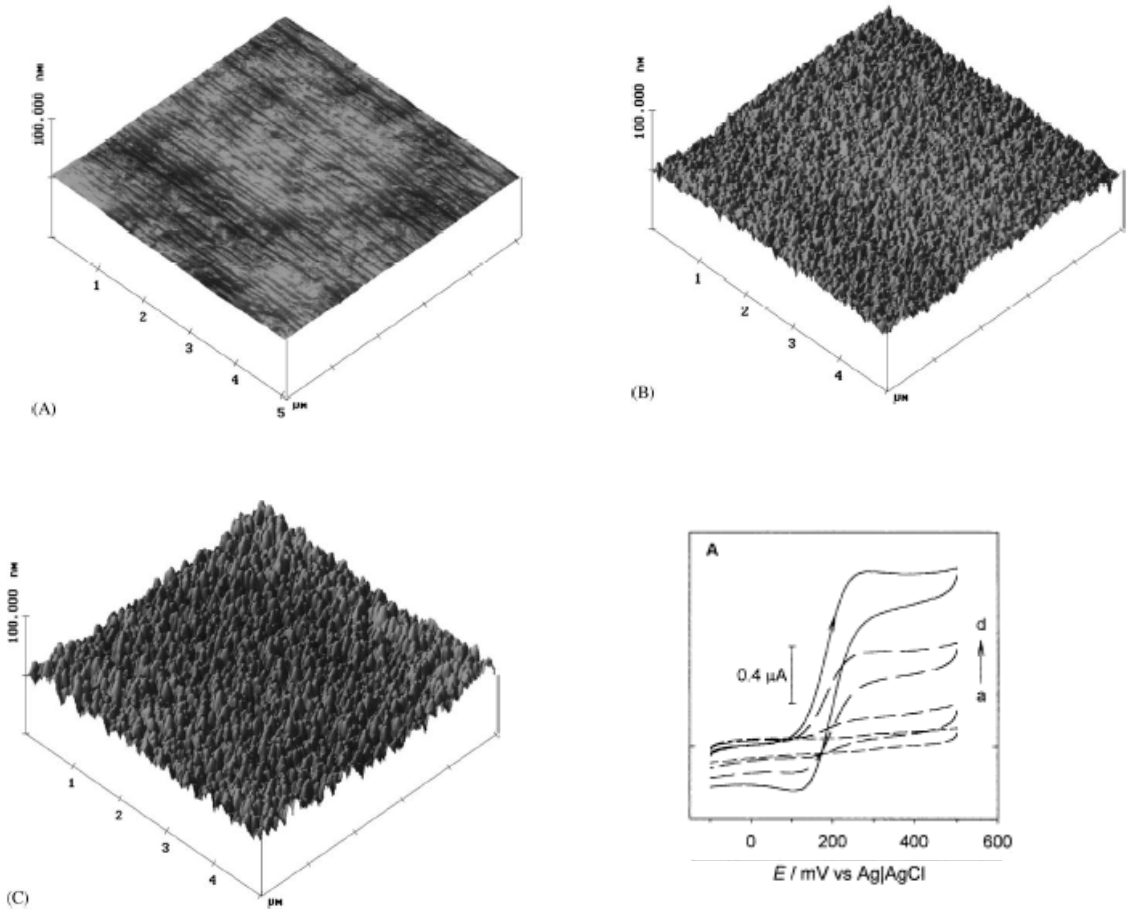

Fig.17. AFM images of a TEOS based film on glassy carbon electrode dried at 50% relative humidity for 12 h after (A) 0, (B) 70 and (C) 120 h in electrolyte solution and cyclic voltammetry of 1 mM ferrocene dimethanol after (a) 0, (b) 24, (c) 56 and (d) 72 h in 0.1 mol dm^{-3} KNO_3 solution [79].

It is understandable that silicate films, which also are named "soft glass", adheres well to glass surfaces. This is because of its good affinity to hydroxyl groups present on glass. On the other hand the film easily peels off from metal surfaces. For this reason the use of functional hybrid materials containing groups which can strongly interact with metal supports, is advantageous. Many studies were devoted to self-assembled alkanethiol monolayers on gold [81,82,83], silver [82], copper [84] and platinum [85] surfaces. It has been shown that an alkanethiol monolayer chemisorbed on gold is stable in a wide range of potentials [81]. Also, three-dimensional thiolated silica gel surface networks with controlled porosity, based on the coupling of self-assembled monolayer and the sol-gel process, were obtained [83] (Fig.18). This feature was used to anchor the silicate matrix to the substrate. The silicate with thiol groups is also employed as intermediate layer for stable film preparation at gold electrodes in this work.

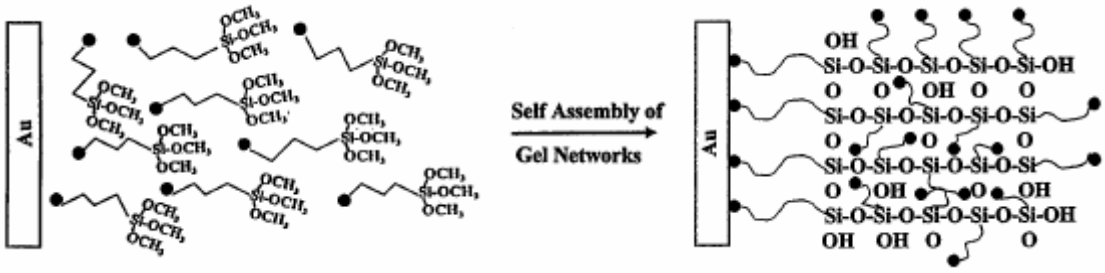

Fig.18. Schematic drawing showing the formation of sol-gel layers based on the self-assembly of thiol-containing precursors [83].

The comparison of the images of thiol- and non-functionalised silica films, electrogenerated and spin-coated, shows the important role of sulphur [80] (Fig.19). A homogeneous, thin matrix was formed only at the electrode surface during electrodeposition of thiolated silicate. In the other cases a heterogeneous film with numerous cracks was obtained. The spin-coated nonfunctionalised matrix exhibited poor adhesion to the metal support which is easy to see in the SEM images.

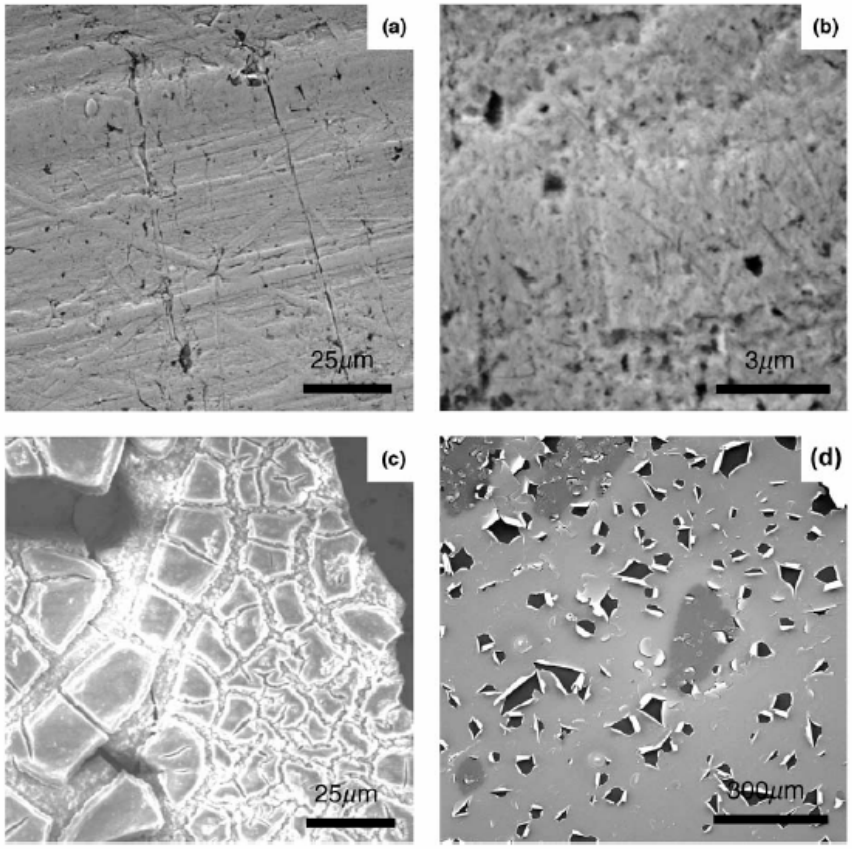

Fig.19. SEM images of (a,b) a thiol-functionalised silica film electrogenerated on gold, (c) a nonfunctionalised silica film electrogenerated on gold from a pure TEOS sol solution, and (d) a silica sol-gel film spin-coated on glassy carbon electrode [80].

Interestingly, thiolated silicate can replace the transition-metal underlayer and be used to improve the adhesion of silver or gold evaporated films onto glass and SiO_2 supports [86].

1.4.3. Loaded films

It is well known, that silicates provide good framework for particles to obtain nanocomposites [87]. This is because of the possibility to disperse different kind of particles within the sol. For example, in this way a new class of composite electrodes were constructed by Lev and co-workers [87,88]. Carbon particles were dispersed into silicate sol and bulk, as well as thin film, silicate based conducting materials, known as carbon ceramic electrodes, were obtained. It is also possible to obtain nanocomposite films rich in carbon nanopowders or nanofibres. Such matrices adhere well to silicon wafers and exhibit good mechanical stability [89] (Fig.20).

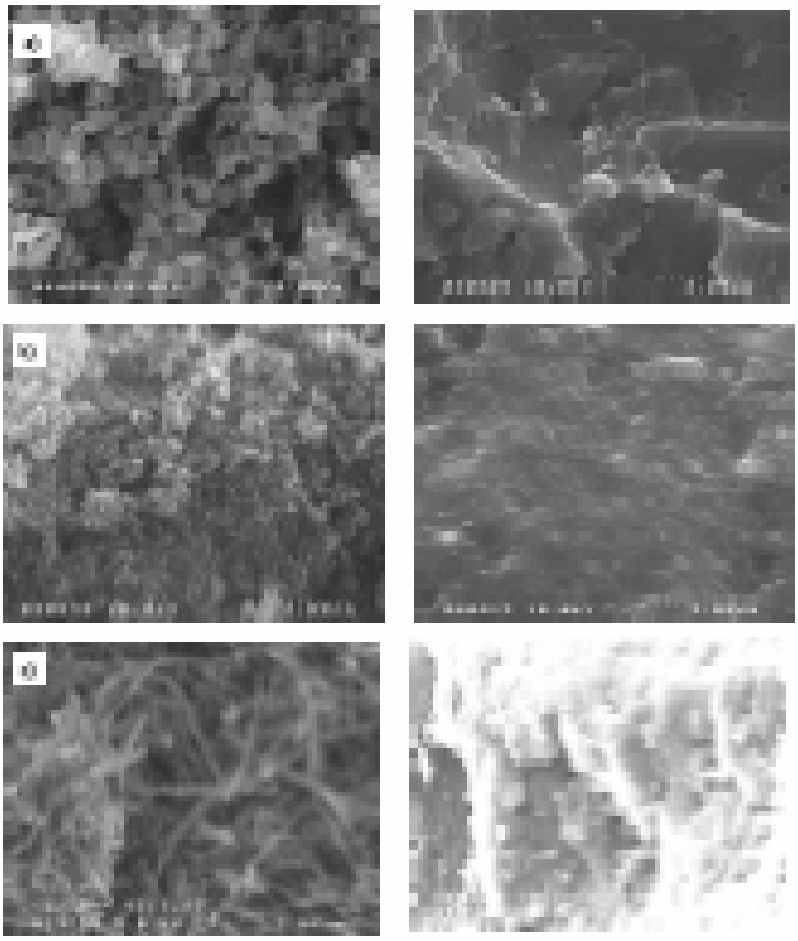

Fig.20. SEM images of various carbon fillers (left side) and the corresponding sol-gel derived thick films (right side), containing 5% (v/v) C: a) and b) particles, c) fibres [89].

Recently, also carbon nanotubes were trapped into a silicate matrix [90]. Multi-walled carbon nanotubes (MWNTs) – silicate films exhibit unique structure and properties. The hydrophobic nanotube sidewalls interact with the hydrophobic MTMOS and this noncovalent adsorption allows the nanotubes to remain separated and limits the aggregation process [90] (Fig.21).

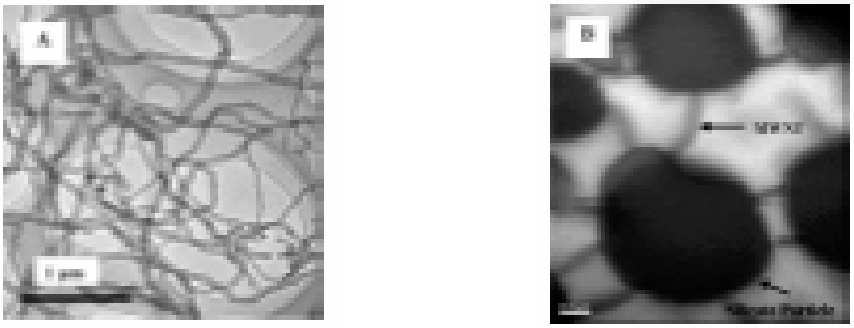

Fig.21. Typical TEM images of the MWNTs used (A) and the MWNT/sol-gel nano-composite prepared by dispersing 0.5 mg/ml MWNTs into the silica sol (B) [90].

Addition of conductive particles into an insulating matrix provides electrical conductivity and offers new applications. For instance, films containing gold or platinum particles [91] are employed in optics, and silver or copper oxide as antibacterial materials [92,93,94]. Zn, Fe, Cu and Ce dispersed in silicate film forms loose aggregates with various sizes depending on the type of metal [95] (Fig.22). The place where they are immobilised also depends on the type of metal particles.

Summarising, the properties of the thin silicate films depend on the type of precursor used or the ratio of precursors with different hydrophilic – hydrophobic properties, the catalyst, the surfactant and the time of preparation. Moreover, silicates provide good framework for particles which opens the way to create new materials. It also has to be emphasised that these materials are much better matrices for nanoparticle dispersions than commonly used organic polymers. This is because of much better stability of the former.

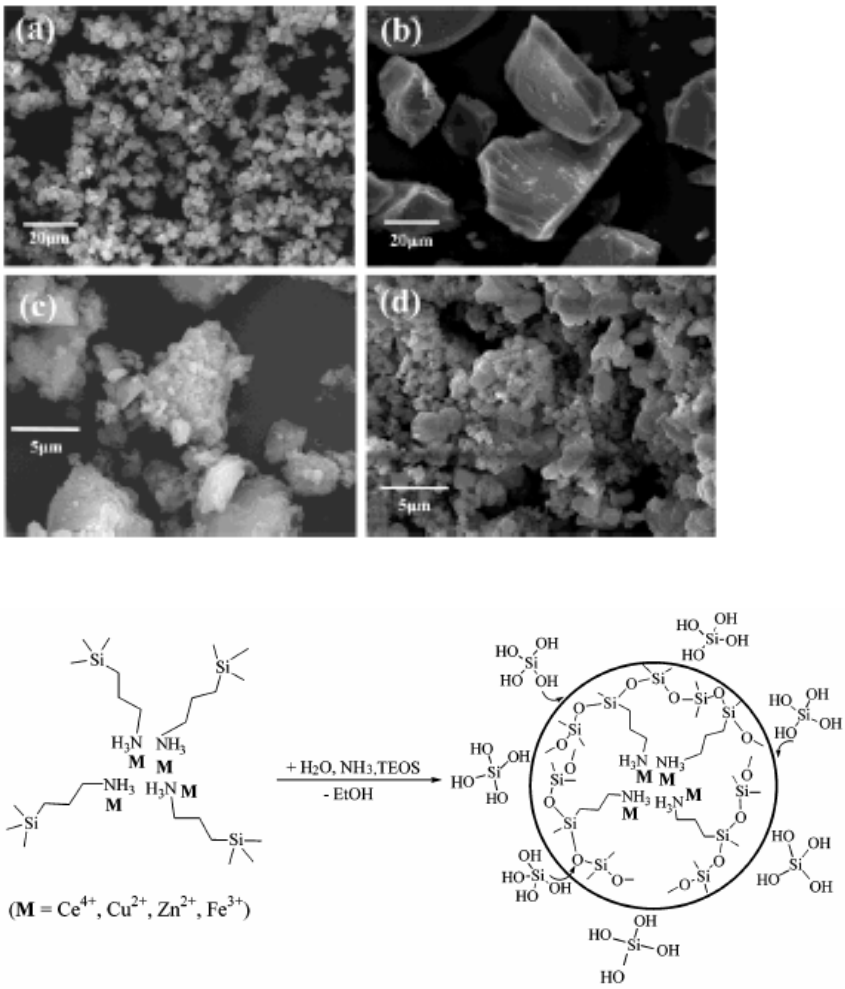

Fig.22. SEM images of (a) zinc-, (b) iron-, (c) copper-, (d) cerium-modified xerogels and schematic reaction pathway for preparation metal-silicate sol-gel [95].

1.5. Thin silicate film modified electrodes – properties and applications

Chemically modified electrodes have been known since 1973 when chemisorption of functionalised olefin on a platinum electrode was electrochemically observed [96]. Electrode surface modification provides a huge concentration of redox active species and attached molecules can act as a fast and selective electron transfer mediator in electrocatalysis [97]. They can be coupled to the electrode surface by covalent immobilisation [97], chemisorption [96] or redox polymer deposition by dip [98], spin coating [99], organosilane bonding [100], electrochemical precipitation and polymerisation [101], adsorption from solution [102] and plasma discharge polymerisation [103]. Recently thin, rigid silicate films were recognised as attractive for electrode surface modification. The first silicate modified electrode was probably obtained by the Murray group in the late 1970's [97,104]. Although the formation of silicate matrix was not mentioned by the authors it is quite probable that it was obtained

during the immobilisation procedure. The first direct report about silicate modified electrode with ferrocene groups appeared in the literature in 1991 [105]. The open framework of silicates gives the opportunity for chemical compound immobilisation and fast electron transfer. The good adhesion to some electrode substrates, favourable abrasion resistance, and the versatility in tailoring the films make sol-gel modified electrodes useful electrochemical tools [15,25,106,107,108]. Some examples of silicate film modified electrodes will be presented below.

1.5.1. Unmodified films

Silicate film provide physical barrier for redox probe transport towards electrode surface [109]. However, the sol-gel film obtained from unmodified precursor - TMOS exhibits selectivity towards positively charged probes accumulating $Ru(NH_3)_6^{3+}$ cations. Negatively charged $Fe(CN)_6^{3-}$ cannot easily diffuse through the matrix because of the repulsion of free electron pairs of oxygen atoms [68].

For example, an interdigitated microsensor electrode modified with a TMOS based film was employed as an amperometric carbon oxide or gaseous hydrogen peroxide sensor employing their partitioning in the porous film [110,111]. Compared to Nafion or membrane type sensors, the results were humidity-independent indicating a stable concentration of water in the sol-gel processed film.

1.5.2. Films with encapsulated electroactive species

Different electroactive redox probes of different charges and sizes were encapsulated within TMOS based silicate matrix [112]. Only a small fraction of them are mobile and able to freely exchange electrons with the electrode. This fact indicates dense and collapsed structure of the TMOS based film. On the other hand, the encapsulation of the species significantly slows down their leaching to the surrounding solution which is clearly visible in Fig.23.

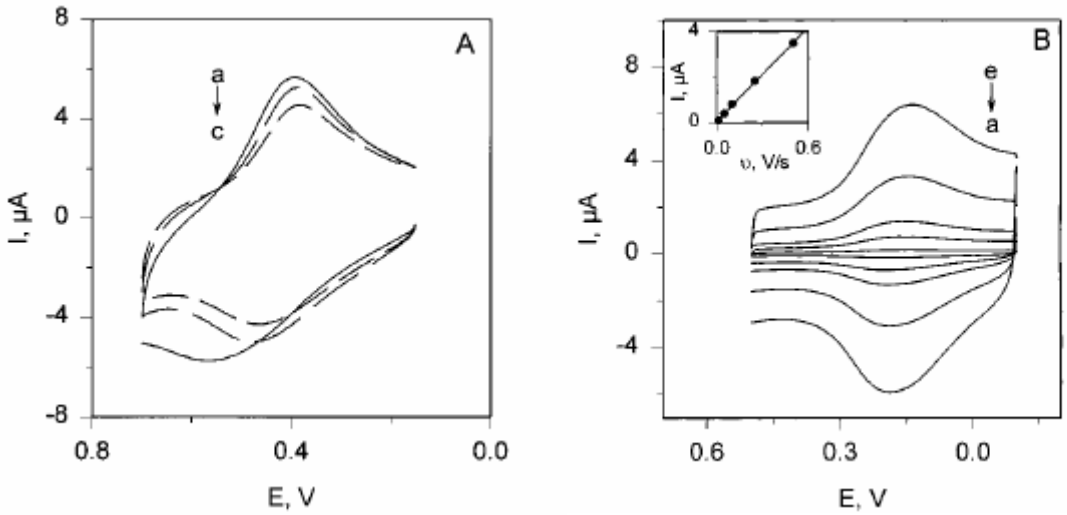

Fig.23. (A) Cyclic voltammograms of gel-encapsulated $Fc(CH_2OH)_2$ acquired a) immediately and b) 1.5 and c) 3 h after placing the film in a 0.1 mol dm^{-3} KNO_3. Scan rate: 100 mV s^{-1}. (B) Cyclic voltammograms of gel-encapsulated $Fe(CN)_6^{3-}$ in 0.1 mol dm^{-3} KNO_3 after placing the film for 30 min at a) 500, b) 250, c)100, c) 50 and e) 10 mV s^{-1}. Insert; plot of the cathodic peak current vs. potential scan rate [112].

The encapsulation of redox probes within silicate films can be useful for potentiometric and amperometric sensor preparation. Organically modified silicate film with entrapped pH indicators providing stable and fast response to solution with wide pH range [113] and exhibiting no significant leaching is one of the examples.

Toluidine blue encapsulated within the three dimensional network of a silicate self-assembled monolayer on the electrode surface and covered by a second layer to protect against leaching was used for electrocatalytic oxidation of NADH [114]. Similarly a platinum electrode modified with a silicate film with entrapped large 12-molybdophosphoric acid molecules was applied for electrocatalytic electroreduction of bromate, chlorate and hydrogen peroxide [115]. These two examples indicate permeation of neutral and ionic species across the deposited silicate film.

1.5.3. Organically-modified films with ligand properties

The incorporation of organic groups into the silicate matrix film changes its properties like hydrobobicity – hydrophilicity, its affinity for the support and for some electroactive species or metal ions. An electrode modified with a bis[(3-triethoxysilyl)-propyl]tetrasulfide (SIS) based film can be used for mercury detection employing the interaction between metal and sulphur presented in sulphide group [116] (Fig.24, 25).

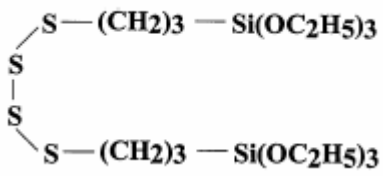

Fig. 24. The structure of bis[(3-triethoxysilyl)-propyl]tetrasulfide [116].

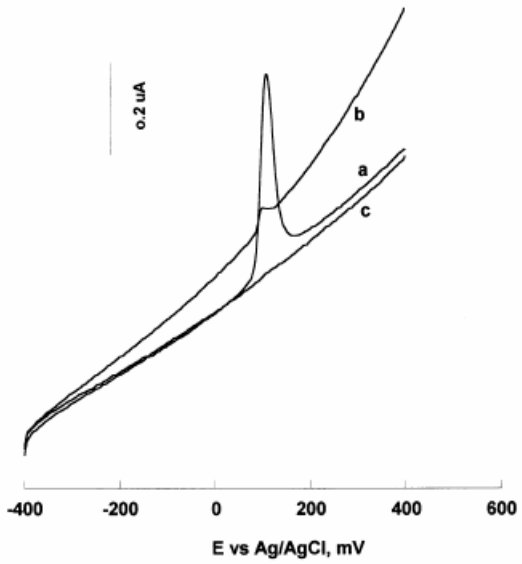

Fig.25. The linear sweep stripping voltammetry of glassy carbon electrode modified with SIS (a) after accumulation in an acetate buffer containing 5 10^{-6} mol dm^{-3} Hg^{2+} in aqueous solution for 10 min., and after the electrode was cleaned (b) electrochemiacly and (c) chemically. Scan rate: 400 mV s^{-1}. Reduction time 15 min [116].

Similarly copper (II) ions can be detected by the electrode modified with a 3-aminopropyltriethoxysilane (APTEOS) based film [117].

1.5.4. Organically-modified films with covalently attached electroactive groups

To prevent leaching of the electroactive species from the silicate matrix they were covalently bonded inside a silica network [38]. Ferrocene based functional groups were most often immobilised in the silicate films. For example ferrocene monocarboxylic acid was linked with the sol-gel film based 3-glycidoxypropyltrimethoxysilane and trimethoxysilane [118]. Unfortunately, the matrix encapsulated redox probe exhibits much better defined voltammetric behaviour with well-shaped peaks in comparison with the redox probe linked matrix. This suggests a lack of translational degree of freedom in the case of covalently bonded ferrocene. Nevertheless due to its stability the

latter system was used as an inter layer between a metal surface and ion selective membrane [118].

Trimethoxysilylferrocene and 1,1'-bis(trimethoxysilyl)ferrocene were used for film preparation on the electrode surface. The electrode modified with the latter compound exhibits a linear dependence of the concentration of electroactive species to the square root of the specific surface area of the gel [38].

Further studies proved that ferrocene can be permanently attached to different silicate precursors. It has been shown that redox active and ion exchange (see below) functions can be combined [119]. For this system the amount of electroactive groups in the film and the structure of the precursor influences the shape of cyclic voltammograms [119] (Figs.26, 27).

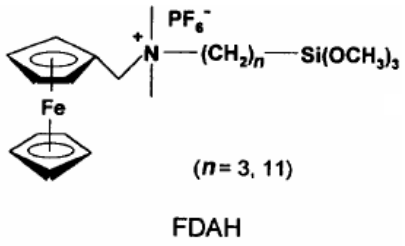

Fig.26. The (ferrocenylmethyl)dimethyl(w-trimethoxysilyl) alkylammonium hexafluorophosphate (FDAH) structure [119].

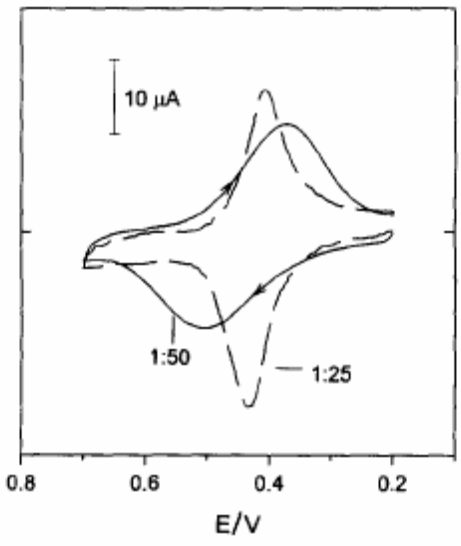

Fig.27. Cyclic voltammograms of FDAH:TMOS hybrid films (1:50; 1:25) in 0.1 mol dm^{-3} aqueous $KClO_4$ with scan rate 50 mV s^{-1} [119].

These hybrid materials are electrochemically stable and able to catalyse the electrooxidation of catechol and can be used as the active element of an amperometric sensor.

1.5.5. Ion-exchange films

One of the advantages of inorganic – organic hybrid materials obtained in mild conditions is the ease of incorporation of specific ion-exchange sites, like NH_3^+, COO^- [1]. They can be used to prevent unwanted substances from reaching the surface or to preconcentrate an ionic analyte. These matrices exhibit permselectivity and are able to exchange ions. The ion-exchange properties of films fabricated from silane-NH_2 or silane-$(COOH)_3$ can be attributed to the strong electrostatic interaction between the acidic/basic functional group in the film and the charged analyte [120] (Fig.28).

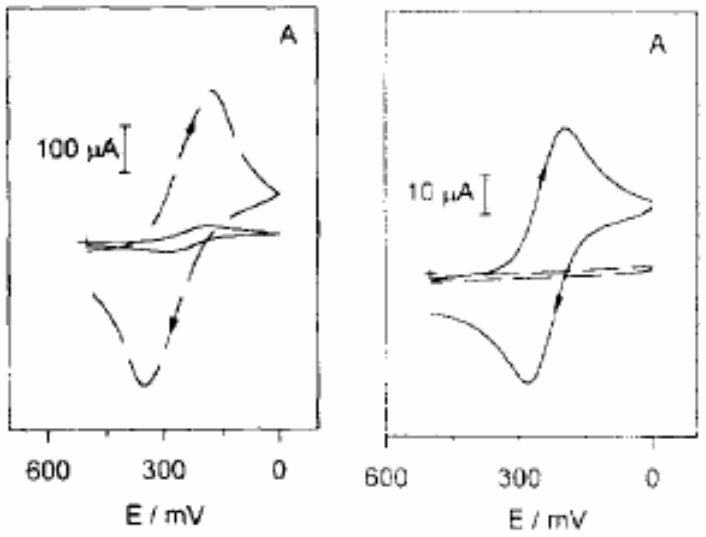

Fig.28. Cyclic voltammograms of (A) sol-gel –NH_2 and (B) sol-gel-$(COOH)_3$ modified glassy carbon electrode in 0.001 mol dm^{-3} $Fe(CN)_6^{3-}$ in 0.1 mol dm^{-3} pH 7.4 phosphate buffer solution respectively at bare (solid line) and modified electrode (dashed line). Scan rate 100 mV s^{-1} [120].

The film containing protonated amine groups exhibits ion-exchange properties and permselectivity [121]. Compared to the nonfunctionalised material the one prepared from APTEOS exhibits a 10-fold faster ion-exchange of the ferricyanide anion (Fig.29).

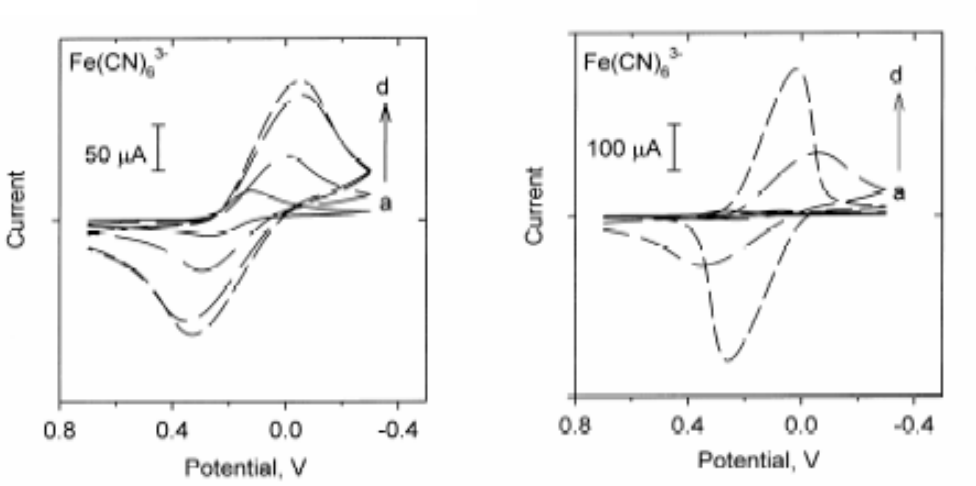

Fig.29. Cyclic voltammograms of 0.001 mol dm^{-3} Fe(CN)$_6^{3-}$ in 0.005 mol dm^{-3}, pH 4.0 KHP buffer at a) 1:1 TMOS:APTEOS and b) 1:1 MTMOS:APTEOS modified electrodes. CVs were acquired (a) ca. 0 min, (b) 10 min, (c) 60 min, (d) 180 min after the electrodes were placed in solution with scan rate 100 mV s^{-1} [121].

Further research into ion-functionalised precursors embedded in organically modified silicates matrices allows obtaining materials with different quantities of ion-exchange sites, different hydrophobicity and porosity [121]. Higher permeability were shown by films prepared from precursors containing larger organic substituents. These materials consist of a more open silicate framework because of spherical hindrance.

The silicates with covalently bounded quaternary ammonium groups are another important group of compounds for ion exchange films. These films are permeable and selective for anions [122,123].

It has to be added that the organic cation-exchange polymers, like Nafion [124] or poly(vinylsulfonic acid, sodium salt) (PVSA) [125] embedded in a non-functionalised silicate matrix or a positively-charged sol-gel silicate [126] also provide silicate based permselective films.

1.5.6. Films with encapsulated enzymes

The ability of silicate matrices to stabilise enzyme immobilisation represents one of the most important properties of these materials. This is because the mild conditions of the sol-gel process are not harsh enough to denature most of the encapsulated biomolecules [127]. Therefore silicate matrices are useful in enzyme modified electrodes preparation [25,128]. For example, the successful immobilisation of urease [129] or laccase [130] within sol-gel films deposited on the electrode surface without

loosing their properties are representative examples. Urease is an enzyme which catalyses urea hydrolysis to ammonia and carbon dioxide. Encapsulated in a sol-gel silica film deposited on the electrode surface it can be used as an urea potentiometric sensor and exhibited a Nernstian slope in a solution with pH lower than 8 [129]. Moreover, it was found that encapsulated urease is more thermally stable than the free one. Laccase in the presence of an appropriate mediator that acts as an electron relay between the enzyme and the electrode is able to catalyse oxygen reduction. The comparison of the activity of laccase immobilised in a silicate film present at the electrode surface and the native enzyme indicates that matrix does not affect its biological and physicochemical properties [130,131,132].

Summarising, in this paragraph the examples of silicate modified electrodes were presented. It is possible to use silicates as a framework for particles immobilisation, species encapsulation or by functional groups covalent bound redox active probe. These features make them attractive composite materials for electrode modification. These inorganic-organic hybrids allow to controlling the architecture of the electrode material and designing integrated electrochemical systems for fast charge and mass transfer processes.

2. Redox liquid modified electrodes

A redox liquid is an organic compound containing redox active groups being liquid at room temperature or a redox probe solution in a hydrophobic solvent. These two classes are called undiluted [133] and diluted redox liquids [134,135] respectively. The electrode surface modification with undiluted redox liquids provides a huge concentration of redox active species limited only by specific volume of the substance. This system is different from other modified electrodes like for example polymer modified electrodes [136], because of the presence of a well defined liquid-liquid interface. To provide electrode stability in aqueous solution the organic phase should be water insoluble.

The geometry of efficient redox liquid based systems depends on whether the organic phase is non-conductive (unsupported system) or ionically conductive (supported system) – namely with dissolved countersions. In general the electrode surface can be modified by a thin organic liquid film [137], a single droplet [137,138,139,140] or a droplet array [137,138].

As was said above the immersion of the redox liquid modified electrode into the aqueous solution creates a well defined liquid|liquid interface. Here during the electrochemical process the ion transfer may take place to maintain the phases neutrality. Therefore the mechanism of electrode reaction depends on liquid deposit geometry and whether it is supported or not. For electrodes not completely covered by an unsupported redox liquid the electrochemical process starts at the three phase junction as it is shown in Fig.30. Obviously, in the case of an electrode completely covered by this phase the electrochemical process does not occur [139].

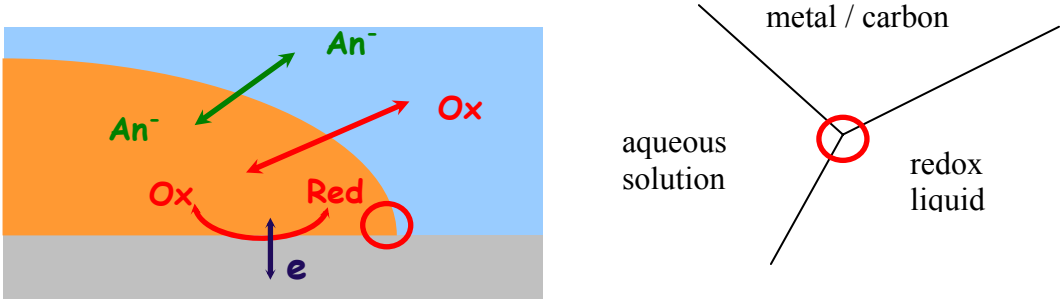

Fig.30. Schematic diagram of the three phase junction and mechanism of the electrode process.

The understanding of the mechanisms of the electrode reactions in these systems is important both from a fundamental and a practical point of view.

The Fig.31 shows the potentials mechanisms of electrode reactions at the redox liquid droplet modified electrode for supported and unsupported systems. The electrogenerated cation is formed during the oxidation process. When the droplet is supported by an electrolyte to maintain the oil phase neutrality the expulsion of non-electroactive cation occurs (Fig.31a). For an unsupported droplet the anion insertion from the aqueous solution (Fig.31b) or the electrogenerated cation ejection (Fig.31c) dominates.

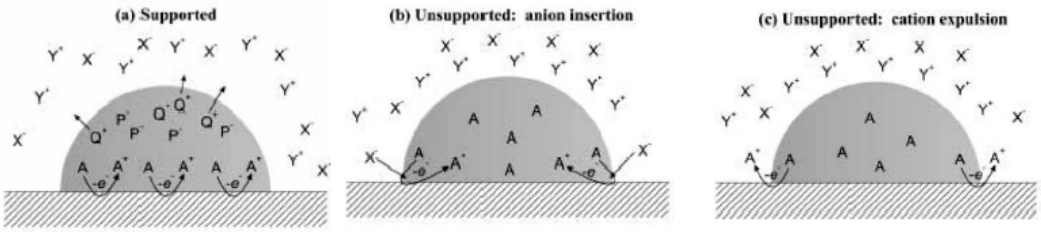

Fig.31. Schematic diagram of the three electrochemical liquid|liquid mechanisms a) supported system after electrooxidation with non-electroactive cation expulsion, b) unsupported system after electrooxidation with counterion insertion and c) unsupported system after electrooxidation with electrogenerated cation expulsion [141].

The electrode surface modification with randomly distributed unsupported microdroplets of undiluted redox liquid was proposed in 1997 [133]. For this purpose water insoluble *N,N,N',N'*-tetrahexylphenylene diamine (THPD) was used. The droplets were deposited on a basal plane pyrolytic graphite (bppg) electrode by evaporation of THPD solution in a volatile solvent and studied in aqueous solution (Fig.32). In the limited range of potentials one reversible one-electron oxidation process described by the following reaction occurs:

$$THPD_{(org)} \leftrightarrow THPD_{(org)}^{+} + e \qquad (3)$$

To maintain the organic phase neutrality an anion transfer from the aqueous solution into the droplet is the next step of the electrode process:

$$THPD_{(org)}^{+} + ClO_{4(aq)}^{-} \leftrightarrow THPD_{(org)}^{+}\ldots ClO_{4(org)}^{-} \qquad (4)$$

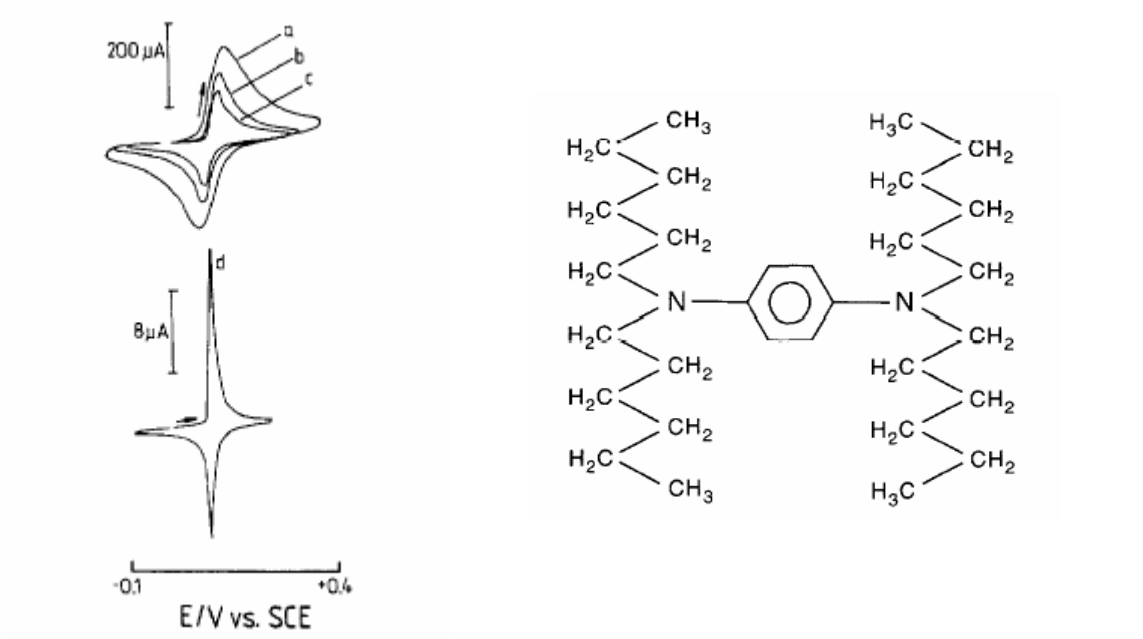

Fig.32. (A) Cyclic voltammograms for the oxidation of THPD deposited on bppg electrode and immersed in aqueous 1 mol dm^{-3} NaClO4 at a scan rate of (a) 500, (b) 200, (c) 100, (d) 2 mV s^{-1}. (B) Molecular structure of N,N,N',N'-tetrahexylphenylene diamine (THPD) [133].

The substituted phenylene diamine with long alkyl chains were later widely used for bppg electrode surface microdroplets modification. For example it was elucidated that oxidation of microdroplets based N^1-[4-(dihexylamino)phenyl]-N^1,N^4,N^4-trihexyl-1,4-

phenylene-diamine (DPTPD) is associated with two consecutive reversible one electron processes accompanied by perchlorate anion transfer into the organic phase [142]. These electrochemical processes can be written as:

$$DPTPD_{(org)} + ClO_{4(aq)}^{-} \leftrightarrow DPTPD_{(org)}^{+}\ldots ClO_{4(org)}^{-} + e \quad (5)$$

$$DPTPD_{(org)}^{+}\ldots ClO_{4(org)}^{-} + ClO_{4(aq)}^{-} \leftrightarrow DPTPD_{(org)}^{2+}\ldots (ClO_{4(org)}^{-})_2 + e \quad (6)$$

Further experiments with other 1,4-phenylenediamine derivatives substituted with alkyl chains of different length showed that electron transfer is followed by a counterion transfer into or/and electrogenerated cation expulsion from the organic phase [143]. The cation expulsion dominates for derivatives with shorter alkyl chains because of some water solubility of the electrogenerated cation.

Also the experiments with *n*-butylferrocene (*n*BuFc) deposit resulted in the expulsion of partially soluble in water *n*-butylferricinium cations formed during the oxidation reaction into the aqueous solution [144]. The dissolution process of *n*BuFc is accompanied by the ion pair formation in the aqueous solution, which is given by the following equation:

$$n\text{BuFc}_{(org)} + X_{(aq)}^{-} \leftrightarrow n\text{BuFc}_{(aq)}^{+}\ldots X_{(aq)}^{-} + e \quad (7)$$

Liquid acid-base complex is another example of a diluted redox system in hydrophobic solvent. The voltammetry of liquid *N,N,*-didodecyl-*N',N'*-diethylphenylenediamine (DDPD) dissolved in bis(2-ethylhexyl) phosphate (HDOP) deposited on the electrode surface resulted in one-electron oxidation of the DDPD-HODP accompanied by proton expulsion in a wide pH range [135]. This process can be described by the following equation:

$$HDOP\text{-}DDPD_{(org)} \leftrightarrow DPO\text{-}DDPD^{+}_{(org)} + H^{+} + e \quad (8)$$

Recently, the electrochemistry of liquid vitamins have attracted a lot of interest. The vitamins E and K_1 are naturally occurring, viscous liquids with electroactive groups. The α-tocopherol named vitamin E is an important antioxidant. The electrochemical oxidation of its droplets involves proton expulsion from the organic phase [145]. The

phylloquinone named vitamin K_1 is a secondary electron acceptor within a photosystem. Its microdroplets are reduced to form hydroquinone [146].

Systems based on a single immobilised droplet of a diluted redox liquid were also widely studied [138,140]. A single droplet of a nitrobenzene (NB) solution of redox probes immobilised at the electrode surface was employed by the Scholz group for electrochemical determination of the Gibbs energy of ion transfer between the aqueous and the organic phase [138,140,147,148]. Highly water insoluble redox active compounds like decamethyferrocene (DmFc) was used for anion transfer studies [147]. The redox potentials were found to depend on the type of anions present in the aqueous solution (Fig.33). This process can be described by the following equation:

$$DmFc_{(NB)} + X^-_{(aq)} \leftrightarrow DmFc^+_{(NB)} + X^-_{(NB)} + e \qquad (9)$$

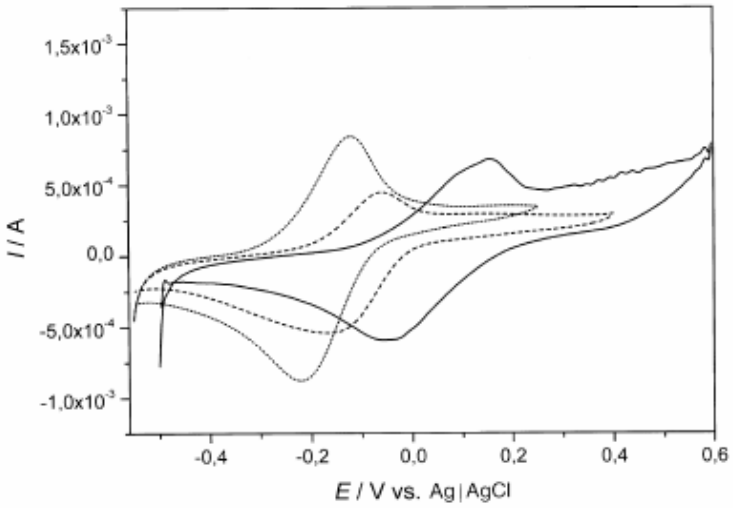

Fig.33. Cyclic voltammetry of 0.1 M DmFc in NB solution deposited on a graphite electrode and immersed in different 1 mol dm^{-3} aqueous electrolyte solutions: (dotted line) NaClO4, (dashed line) KSCN, (full line) KCl; scan rate 100 mV s^{-1} [147].

A linear dependence of the redox potential and the standard potentials of the anions transfer across the liquid-liquid interface was found (Fig.34) with a slope close to unity. This proves the correctness of equation (9) and allows the determination of the Gibbs energy of NO_3^- anion transfer.

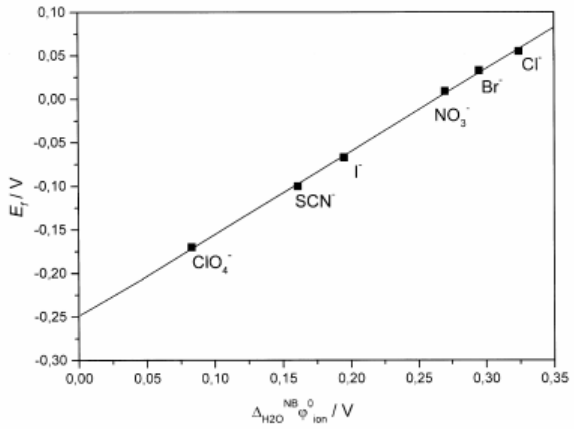

Fig.34. Plot of the peak potentials of DmFc vs. the standard transfer potential of anions from aqueous solution to NB [147].

Next, similar experiments were done with iron(III) tetraphenyl porphyrine chloride (Fe(III)-TPP-Cl) [140,148] for a cation transfer studies. Also in this case the redox potentials were found to depend on the cations present the aqueous solution. This process can be written as follows:

$$Fe(III)\text{-}TPP\text{-}Cl_{(NB)} + Cat^{+}_{(aq)} + e \leftrightarrow Fe(II)\text{-}TPP\text{-}Cl_{(NB)}^{-} + Cat^{+}_{(NB)} \qquad (10)$$

Further, this concept was applied to determine the unknown standard Gibbs energies ($\Delta_{Aq}^{NB}\varphi_{X^-}^{0}$) of the transfer of peptide anions from the aqueous solution to the nitrobenzene phase [149]. This research has particular importance in pharmacy. This liquid|liquid interface imitates parts of biological systems and are helpful in studying the transport and distribution processes of drugs.

To prove that the voltammetric process of a single microdroplet and microdroplets array occurs at three phase junction various experiments were performed. As first the microscopic images of THPD deposited on a siliconised ITO electrode immersed in 0.1 mol dm^{-3} $NaClO_4$ aqueous solution were taken after the electrochemical experiment [133]. The colour changed from yellow to blue on the circumference of the droplets indicating the place where the electrogenerated cations are formed.

Metallic silver microrings were observed during electrochemical $THPD^{+}$-ClO_4^{-} complex formation after the reaction with silver perchlorate [150]. This process can be described by the following reaction:

$$THPD_{(org)} + Ag_{(aq)}^{+} + ClO_{4(aq)}^{-} \leftrightarrow THPD_{(org)}^{+}\ldots ClO_{4(org)}^{-} + Ag_{(s)} \qquad (11)$$

The experiment with a single droplet of ferrocene solution in NB having different sizes also confirms the importance of the three phase boundary [139]. A linear dependence between the voltammetric peak current and the droplet radius was found. The increase of droplet radius results in bigger peak current.

The monitoring of the electrogenerated cation release from a droplet of DmFc solution in NB during the electrooxidation process by ultramicroelectrode also proved that the reaction starts at the three phase boundary [151]. The largest concentration of $DmFc^+$ cations was detected close to the circumference of drop.

It was also found by Marken and co-workers [152] that the voltammetric peak current depends on the number of microdroplets deposited at the electrode surface. Together with an increasing number of droplets at the electrode surface the peak current increases. When the droplets merge to form a thin layer a decrease of the peak current was observed, due to of shorter length of the three phase junction [152].

An experiment with cylindrical microelectrodes immersed into the two immiscible liquids shows that the reaction starts at the three phase boundary [153]. The magnitude of the peak current depends on the platinum wire diameter. With increasing wire diameter I_p is grows larger, which indicates that the three phase junction is getting longer (Fig.35a). Therefore this is clear evidence that the length of the latter affects the efficiency of the electrode process in such a system. Polymer ring formation during the electropolymerisation at the liquid|liquid interface also indicates that the three phase junction is needed for reaction to take place [154]. The polymer was formed on the interface monomer solution in NB|aqueous electrolyte|platinum wire (Fig.35b).

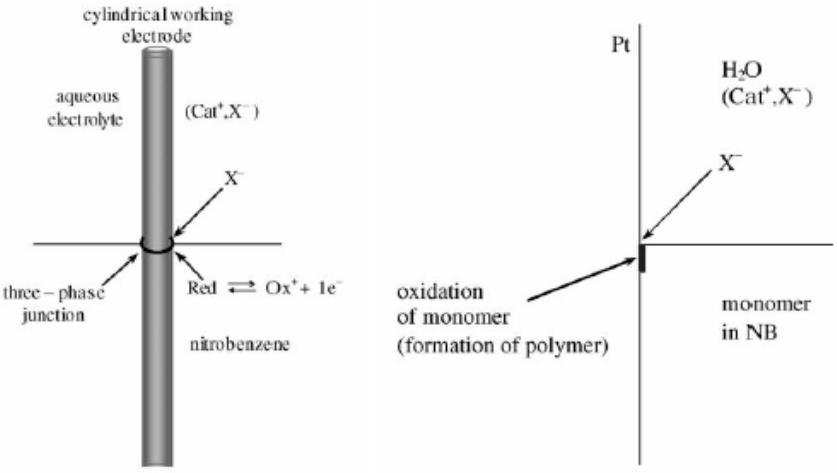

Fig.35. (a) Graphical representation of the formation of the three-phase boundary [153]. (b) A detailed view of polymer deposition mechanism [154].

Scanning confocal microscope images and profiles (Fig.36) of water droplets containing copper [141] taken after electrolytic copper deposition are also clear evidence that in the case of unsupported systems the reaction occurs at the three phase junction.

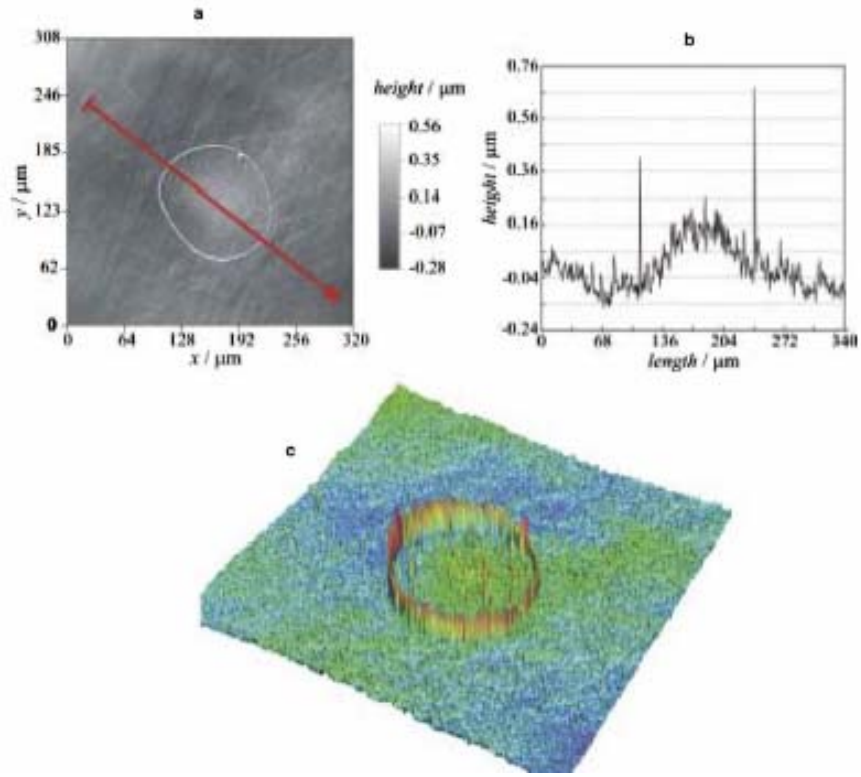

Fig.36. The profiles of the scanning confocal microscopy of edge plane pyrolytic graphite modified by the deposition of cooper from a water droplet containing 0.05 mol dm^{-3} CuSO4 immersed in 0.1 M TBAP/DCE parts (a) and (b) along with the corresponding 3-dimentional image (c) [141].

Not only droplets but also thin film modified electrodes were studied. The pioneering experiment of a thin ionically conducting organic film deposited at the electrode surface and immersed into an aqueous solution was done by the Anson group. The NB based film was deposited on a pyrolytic graphite electrode [155]. The organic layer with dissolved water insoluble electroactive species, like DmFc [156] or porphyrin-type molecules [157], completely covered the electrode surface. For this reason the film was supported with an electrolyte e.g. quaternary ammonium salt to provide ionic conductivity. During the electrochemical process of the electroactive compound electrogenerated ions are formed. Similarly, in the case of unsupported system, to maintain neutrality of the organic phase the ion transfer occurs across the liquid|liquid interface. The direction of the ion transfer is driven by the hydrophobic/hydrophilic properties of the electrogenerated species and counterions.

Again two processes can occur: the expulsion of the electrogenerated ions from the organic phase into the aqueous solution or the transfer of counterions into the organic phase. In the majority of cases, the movement of supporting ions from the organic phase into the aqueous solution was detected [157]. Surprisingly, even the water insoluble decamethylferrocinium cation was detected in aqueous solution [158]. This setup was also used to study the electron transfer kinetics across the liquid|liquid interface [159,160]. Interestingly, nitrobenzene or benzonitrile thin film modified electrodes with cobalt porphyrins exhibited a higher catalytic effect of oxygen reduction to water in comparison to the electrode with adsorbed catalyst [161,162]. In further experiments nitrobenzene was replaced by a room temperature ionic liquid that was used as a supported organic phase [163] (Chapter.3).

Untill now the organic droplets were immobilised onto the electrode surface and immersed into the aqueous solution. Recently, the inverse electrode was proposed. The water droplets containing $Fe(CN)_6^{4-}$ are now immobilised onto the electrode surface and immersed into 1,2-dichloroethane (DCE) supported by tetrabutylammonium perchlorate (TBAP) [141]. In this case to maintain the neutrality of the aqueous phase the expulsion of K^+ into DCE solution occurs. This process is given by the following equation:

$$Fe(CN)_6^{4-}{}_{(aq)} + K^+_{(aq)} \leftrightarrow Fe(CN)_6^{3-}{}_{(aq)} + K^+_{(DCE)} + e \qquad (12)$$

To summarise, the systems based on redox liquid deposits exhibits specific and sometimes complicated electrochemical behaviour. However, the mechanism of the electrode reactions is already quite well elucidated and numerous applications can be envisaged. It is already clear that the length of the three phase junctions affects the efficiency of these electrochemical systems. It is clear that the preparation of electrode support extending this parameter is a challenge.

3. Room temperature ionic liquids as electrochemical solvents

The room temperature ionic liquids (RTILs) represent a quite novel class of electrochemical solvents. Since this topic is relatively new and part of this thesis is devoted to RTIL modified electrodes they will be discussed separately.

RTILs are defined as “compounds composed of ions that exist in its liquid state at a temperature around 298 K and below” [164]. Most of them consist of 1-alkyl-3-

methylimidazolium, *N*-methyl-*N*-alkylpyrrolidinium and tetraalkylammonium cations together with tetrafluoroborate, hexafluorophosphate and bis(trifluoromethyl-sulfonyl)imide anions. Their crystallisation is not permitted because of the large constituent anions size and the asymmetry of organic cations.

The RTILs are characterised by unusual properties [164,165,166] like significantly larger ionic conductivity over common organic solvents. They exhibit high polarity [167], high viscosity [168], enhanced by strong hydrogen bond interactions causing slow diffusion of electroactive species within and negligible vapour pressure [168]. Moreover, they are distinguished by high thermal, chemical and electrochemical stability. RTILs have an unique ability to dissolve numerous organic and inorganic compounds. One of their most important features is a wide electrochemical window up to about 5.0 V [169]. This is because both constituent cations/ anions are reduced/oxidised at sufficient low/high potentials. The potential window is narrowed in the presence of impurities [164]. Although the view about RTILs low toxicity was undermined recently [170] and truly depends on their exact composition, most scientists name them as “green solvents” [164].

Among numerous applications the electrochemical investigation of gases like oxygen, carbon dioxide, ammonia and sulfur dioxide in RTILs is recently widely studied [171,172,173]. This is because their detection is important in medicine as well as in industries including in exhaust gases. The one-electron reduction of oxygen to superoxide in RTIL is reversible [172].

$$O_2 + e \leftrightarrow O_2^{-\bullet} \qquad (13)$$

The electrogenerated superoxide in RTILs readily react with carbon dioxide and form peroxydicarbonate ion [164] what is given by the following equation:

$$O_2^{-\bullet} + CO_2 \leftrightarrow CO_4^{-\bullet} \qquad (14)$$

Therefore this reaction can be utilised to prepare RTIL based sensors for carbon dioxide in the presence of other gases. Similarly, the electrode reaction of ammonia in RTIL can be applied for sensing in the gaseous phase [173]. These applications are quite promising because of the negligible vapour pressure of RTIL’s.

Recently, RTILs were employed for electrodeposition of various metal like silver [174], copper [175], and germanium nanoclusters on gold [176] or titanium nanowires on highly oriented pyrolytic graphite [177]. Moreover the RTILs are popular as solvents for a number of synthetic reactions, like the Diels-Alder reaction, catalytic reactions of organometallic compounds or electrocatalytic dimerisation and polymerisation [164]. Furthermore RTILs are employed as electrolytes for batteries [178], in traditional fuel cells [179] and for ion-selective membrane preparation [180,181].

Very recently, the RTILs were also applied in biphasic electrochemical studies [182,183,184]. Their ability to extract ions or neutral molecules from aqueous solution into the organic phase were elucidated. Therefore physicochemical studies on the RTIL-aqueous solution interface are of great interest [182,185]. The electrochemical properties of a self-assembled 2-aminoethanethiol monolayer modified gold electrode covered by a DmFc solution in RTILs are presented in [184]. The one-electron electroxidation of DmFc is coupled to the dissolution of RTIL cations to the aqueous solution. To maintain the neutrality during the $DmFc^+$ cation electroreduction the transfer of RTIL anions from the organic phase to the aqueous solution was observed. During preparation of this thesis biphasic system based RTIL modified carbon-silicate materials [186] or RTIL based carbon paste [187] were also developed in our group.

4. Goal

This thesis focuses on the electrode surface modification with the thin silicate films and the redox liquid immobilisation. The project consists of film preparation, its characterisation and studies of the electrochemical behaviour of the modified electrodes with various types of the hydrophobic redox liquids. Therefore also the hydrophobic silicates were chosen for their stable immobilisation. The development of the electrode surface was the other challenge. This was achieved by the embedding of conducting nanoobjects within the open framework of silicates for efficient electrode process of the redox liquid.

5. Experimental part

To characterise the obtained silicate films spectroscopy and microscopy methods were employed. Infrared transmittance (FTIR) and reflectance (FTIRRAS) spectroscopy provided information about network formation. AFM allowed to get the knowledge about surface topography. The film structure details were also given by field emission gun scanning electron microscopy (FEGSEM). The scanning electron microscopy with roentgenographic microanalysis helped determine surface composition. To study the electrochemical properties of the film deposited onto electrode support before and after its modification with redox liquid the electrochemical techniques like cyclic voltammetry (CV), chronoamperometry (CA) and differential pulse voltammetry (DPV) were applied. The basics of these methods are briefly presented below.

5.1. Infrared spectroscopy

Infrared spectroscopy provides information about chemical compounds structure. This is due to the interaction between the infrared (IR) radiation with matter. The photon energy in this range is not enough to excite electrons but induces vibrational excitation of covalently bounded atoms and groups. The atoms in a molecule are constantly oscillating around average positions changing the bonds length (stretching vibrations) and angles (bending vibrations) between them. Atoms in a given molecule absorb a unique set of IR radiation frequencies matching the frequencies of the molecular oscillations and the spectrum with bands corresponding to functional groups can be recorded [188]. In principle the absorption of IR radiation is possible, if the vibrations cause a change in the dipole moment of the molecule.

In the experiments in this thesis the transmittance spectra of silicate precursors were recorded. The FTIR spectra were measured by detection of attenuated light after its passage through the sample. To acquire detailed information about species adsorbed on metal support the reflectance technique was used [189]. This non-destructive method allows studying very thin films and to determine the orientation of molecules. The IR radiation is directed onto the surface of the sample at an angle of incidence (I) which is equal to the angle of the reflection (R) (Fig.37). The choice of the angle of incidence depends on the adsorbed film thickness and for very thin coatings it equals about 80°.

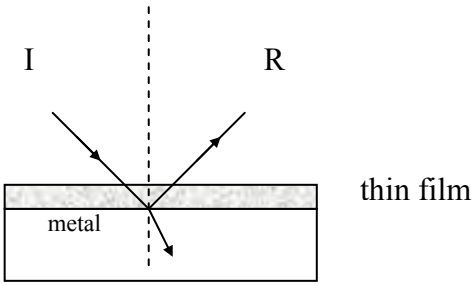

Fig.37. The scheme of incidence of IR radiation.

The angle of the reflected light from the metal support depends, besides on the incidence angle, also on its polarisation (Fig.38). For the vertical polarisation, the vectors of the incident and reflected light are opposite to each other and cancel on the surface. As result, no stationary waves appear and no interaction with the adsorbate is observed. The situation changes significantly for parallel polarisation. The vectors of polarised light crosses at a point and generate stationary waves, which interact and the spectrum can be recorded.

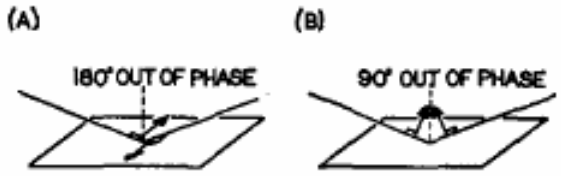

Fig.38. Relative phase of the electric vector for (a) perpendicular and (b) parallel polarisation before and after reflection from a metal surface [189].

5.2. Atomic force microscopy

The AFM technique was chosen instead of scanning tunnelling microscopy to provide information about surface topography for the reason that silicate sol-gel processing films are not conductive [190]. An atomically sharp tip attached to a cantilever (spring constant 0.01-100 N m $^{-1}$) moves over the surface [191,192]. The deflection force is measured in x, y position during the tip's movement over the sample. The deflection is caused by interaction force between the tip and sample atoms. The potential between tip and sample is described by the Lennard-Jones model. Herein two distinguished regions with minimal potential are pointed out. This corresponds to contact and non-contact mode, where the repulsive (near) and the attractive (far)

interaction occurs, respectively. In the experiments presented in this thesis the contact mode was employed. The deflection of repulsive force in direct contact was determined by the reflection of a laser beam from top of cantilever on photodiode (Fig.39). Next, under the influence of the beam a feedback regulator activates a piezoelectric control. The moving of the latter one allows to keep the deflection force constant with sensitivity about 0.01 nm in the force range 10^{-13}-10^{-8} N.

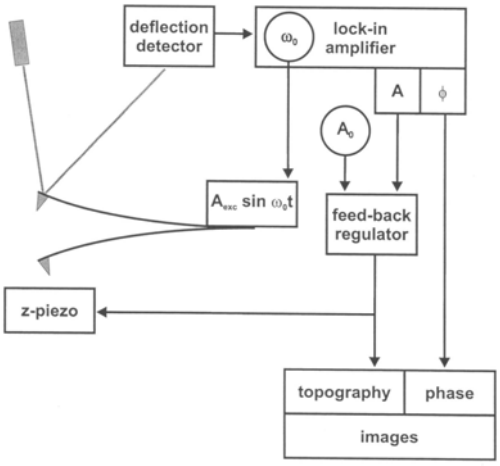

Fig.39. Scheme of AFM contact mode [193].

5.3. Scanning electron microscopy

The SEM uses an electron beam to acquire knowledge about the sample morphology. This method requires a conductive sample. In the case of non-conductive materials an ultra-thin layer of e.g. gold, platinum is deposited on top of the sample. The primary electron beam is produced at a cathode, placed at the top of column, named gun. There are two main types of electron guns, a hot filament gun, where electrons are extracted from a heated tungsten wire through thermionic emission, or the field emission gun (FEG) where the electrons are extracted from a needle shape cathode by the application of a strong electric field. The extracted electrons are accelerated from a few hundred to tens of thousands of electron volts. The primary electron beam is focused by a magnetic lens and apertures onto the sample surface. To limit electron scattering in the column a high vacuum is needed. This also prevents sample oxidation. Next, a set of scan coils deflect the beam in a scanning pattern over the sample surface. When the examined material is struck by the electron beam several types of signals are formed. Secondary electrons are produced by the interactions between the primary

electrons and the weakly bonded conduction-band electrons in metals or the valence electrons of insulators and semiconductors. They have low energy, and thus come from a very shallow region at the sample surface. On this basis information about sample topography can be elucidated. Backscattered electrons are created by electron beam interaction with the positive charged nucleus *via* elastic collisions. They have high energy. This allows getting knowledge about morphology and average surface composition [194].

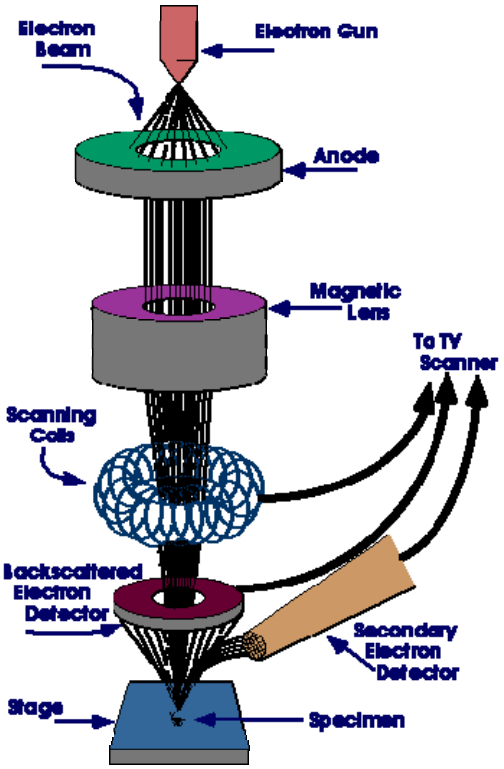

Fig.40. Scheme of FEGSEM setup [195]

The elemental microanalysis can be done by the collecting the characteristic X-ray radiation that is produced when an inner shell electron is struck and an outer shell electron fills the vacancy and releases energy as an X-ray photon. The plot of the number of counts versus energy provides information about the elements and their concentration in the studied materials.

5.4. Cyclic voltammetry

Cyclic voltammetry provides considerable information on the thermodynamics of redox processes, for example redox potential, and the kinetics of heterogeneous electron-transfer reactions and coupled chemical reactions or adsorption processes. For that reason the technique was chosen in this work to obtain qualitative information about electrochemical reactions. In this method the potential is swept between two values E_i and E_e at a fixed rate in forward scan and is then reversed and in backward scan swept back to E_i, forming a triangular potential waveform (Fig.41a).

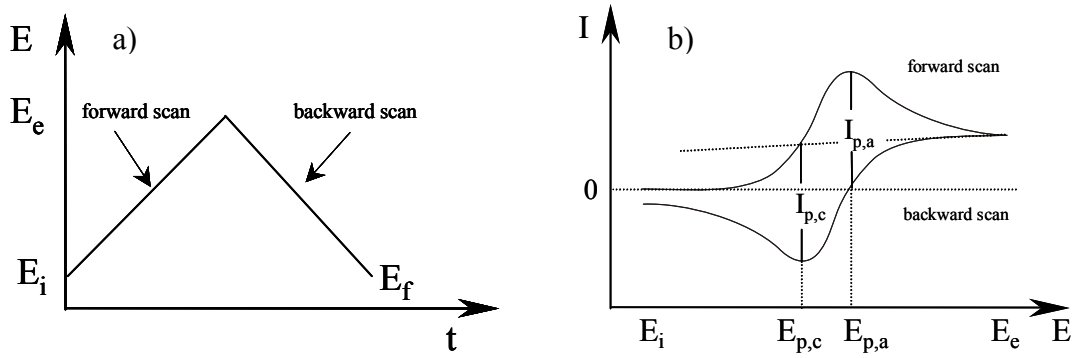

Fig.41. a) Cyclic potential sweep, b) resulting cyclic voltammogram [196].

During the potential sweep the potentiostat measures the current resulting from the applied potential. The current vs. potential plot is used for the analysis (Fig.41b). When the bulk solution initially contains only a reduced form (Red) of the redox couple at the initial potential (lower than the redox potential) no conversion of Red to Ox occurs. As the applied potential approaches the redox potential, the anodic current increases until a peak is reached $I_{p,a}$ (forward scan). At this point the potential is sufficiently positive that any Red reaching electrode surface is converted to Ox:

$$\text{Red} \rightarrow \text{Ox} + \text{e} \qquad (15)$$

The characteristic peak is formed because of the initial increase of Red concentration gradient and further depletion of Red form. At this point the current depends upon the rate of mass transfer to the electrode surface. During the reverse scan (backward scan), the previously generated Ox form accumulated near the electrode surface is reduced to

Red form. This reaction results in increasing of the cathodic current which in reversible process produces a peak shape response:

$$Ox + e \rightarrow Red \qquad (16)$$

When the reversible redox system remains in equilibrium throughout the potential scan the peak current for the Red-Ox couple at 25°C can be described by the Randles-Sevcik equation [196,197]:

$$i_p = \left(2.69 \cdot 10^5\right) \cdot n^{2/3} \cdot A \cdot C \cdot D^{1/2} \cdot \upsilon^{1/2} \qquad (17)$$

where: n – number of the electrons transferred

A – electrode area (cm^2)

D – diffusion coefficient ($cm^2\ s^{-1}$)

C – redox probe concentration ($mol\ cm^{-3}$)

υ - the scan rate ($V\ s^{-1}$)

Moreover, the equilibrium requires the surface concentration to be maintained according to Nernst equation. Under these conditions the cyclic voltammogram is characterised by the following properties:

- the formal potential is centred between $E_{p,a}$ and $E_{p,c}$; $E^0 = \left(E_{p,a} + E_{p,c}\right)/2$
- the separation between the peak potentials is equal 59/n mV at 25°C for all scan rates, where n is the number of the transferred electrons; $E_p = \left(E_{p,a} - E_{p,c}\right)$
- the peak width is equal to 28.5/n mV at 25°C for all scan rates; $E_{p/2} = E_{1/2}$
- the peak current ratio ($i_{p,a}/i_{p,c}$) is equal to unity for all scan rates
- the peak current is linearly dependent on the concentration of the redox probe
- the peak current increases linearly with the square root of the scan rate

For the irreversible and quasi-reversible systems, when the chemical reaction is coupled to the redox process or adsorption of either reactants or products occurs the individual peaks are reduced and widely separated. The peak current at 25°C in such a system is described by the following equation [196]:

$$i_p = \left(2.99 \cdot 10^5\right) \cdot n \cdot \alpha^{1/2} \cdot A \cdot C \cdot D^{1/2} \cdot \nu^{1/2} \qquad (18)$$

where: α - transfer coefficient

During the electrochemical reaction both the Red and Ox form can be involved in an adsorption-desorption process. When both forms adsorb on the electrode surface this interfacial behaviour satisfy the Nernstian equation and exhibits symmetrical cyclic voltammetric peaks ($\Delta E_p = 0$) and a peak half width of 90.6/n mV at 25°C. The peak current is linearly dependent on the surface coverage (Γ) and the potential scan rate [196]:

$$i_p = \frac{n^2 \cdot F^2 \cdot \Gamma \cdot A \cdot \nu}{4 \cdot R \cdot T} \qquad (19)$$

where: F – Faraday constant (C mol^{-1})

Γ - surface coverage (mol m^{-2})

R – gas constant (J mol^{-1} K^{-1})

T – temperature (K)

The surface coverage can be determined by the quantity of charge consumed by the surface process:

$$Q = n \cdot F \cdot A \cdot \Gamma \qquad (20)$$

The prepeak or postpeak is observed on the voltammogram when either the Ox or the Red form is observed at a potential more positive or negative than the diffusion-controlled peak, respectively [196].

5.5. Chronoamperometry

Chronoamperometry is another method to study the mechanisms of electrode processes. It involves potential step changes at the working electrode. In the first step

the potential (E_1), at which no electrochemical reaction of redox active species take place, is applied. Next, the potential is changed abruptly to that (E_2) when the faradaic current connected to the electrochemical reaction occurs. For simple a redox reaction (eq.15) it results in a current decrease as a function of time (Fig.42b).

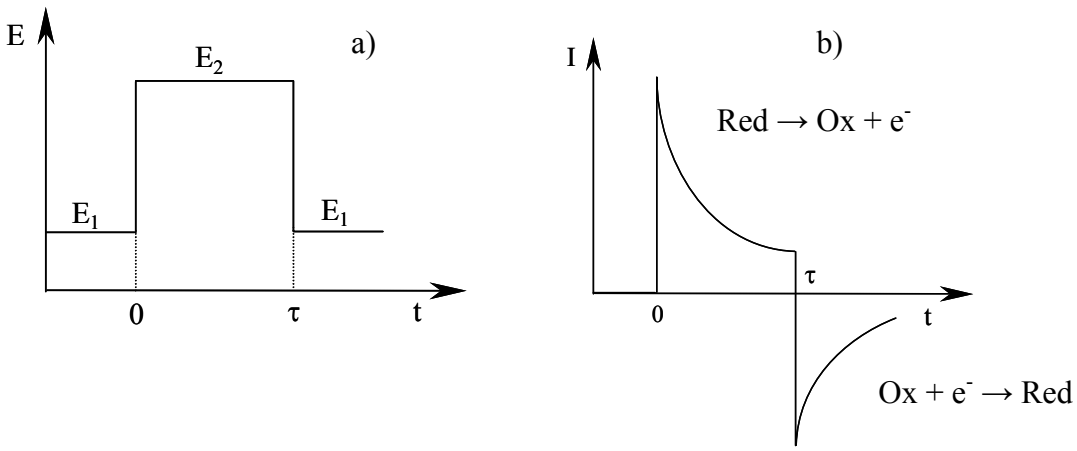

Fig.42. Double potential step chronoamperometry a) typical waveform, b) current response [196].

Under these conditions the mass transfer is controlled by diffusion. Over time the concentration of substrate close to the electrode surface is diminished and a diffusion layer is formed. The current-time curve is described by the Cottrell equation [196,197,198]:

$$i(t) = \frac{n \cdot F \cdot A \cdot C \cdot D^{1/2}}{\pi^{1/2} \cdot t^{1/2}} \quad (21)$$

where: t – time

Therefore the linearity of i_p vs. $t^{-1/2}$ relationship is regarded as confirmation of simple mechanism of the electrode reaction.

5.6. Differential pulse voltammetry

Differential pulse voltammetry (DPV) is usually used for trace level determination and when the background current should be eliminated. Because of the latter reason it can be used for relatively precise determination of the redox potential and therefore this method was used in this work. The potential waveform in DPV consists of small pulses

with constant amplitude superimposed upon a staircase waveform. The current is sampled twice (Fig.43a) in each pulse period at first before the pulse and at the end of the pulse. This allows eliminate the capacitive current. For simple a electrochemical a redox reaction the resulting differential pulse voltammogram consists of current peaks (Fig.43b). The peak current is directly proportional to the concentration of the redox probe in the bulk solution and is given by the following equation [196,197]:

$$\Delta i_p = \frac{n \cdot F \cdot A \cdot D_{Ox}^{1/2} \cdot C_{Ox}^{*}}{\pi^{1/2} \cdot t_p^{1/2}} \cdot \left(\frac{1-\sigma}{1+\sigma} \right) \tag{22}$$

where: $\sigma = \exp\left(nF\Delta E_p / 2RT\right)$

The peak potential is given by the following equation:

$$E_p = E_{1/2} - \Delta E / 2 \tag{23}$$

where: ΔE - the pulse amplitude

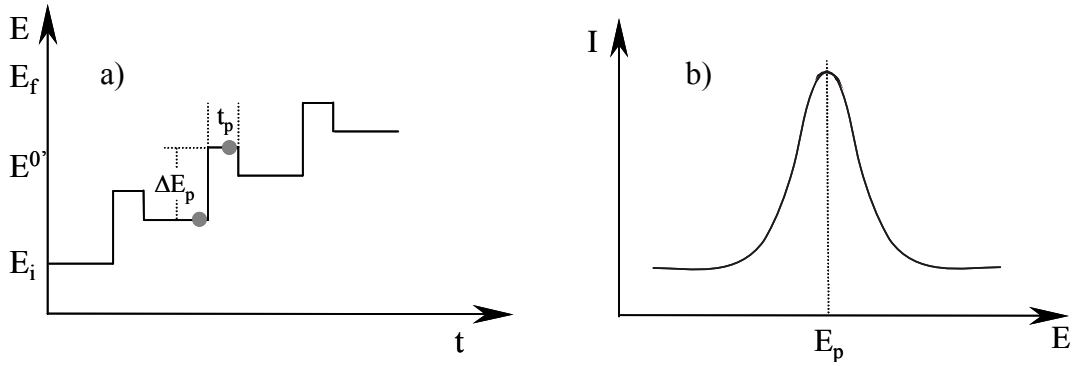

Fig.43. a) Potential program for differential pulse voltammetry, b) resulting differential pulse voltammogram [196].

5.7. Experimental conditions and procedures

5.7.1. Chemical reagents and materials

Methyltrimethoxysilane (99%) – **MTMOS,** Aldrich

3-mercaptopropyltrimethoxysilane (99%) – **MPS**, Aldrich

t-butylferrocene (99%) – **tBuFc**, Strem

N,*N*-didodecyl-*N'*,*N'*-diethylphenylene diamine – **DDPD**, was obtained from Dr F. Marken, Bath University (UK)

di-(2-ethyl-hexyl)phosphate acid (97%) – **HDOP**, Aldrich

Ferrocenedimethanol (99%) – **$Fc(CH_2OH)_2$**, Aldrich

1-decyl-3-methylimidazolium bis(trifluoromethylsulfonyl)imide – **$C_{10}mimN(Tf)_2$**

1-butyl-3-methylimidazolium bis(trifluoromethylsulfonyl)imide – **$C_4mimN(Tf)_2$**

1-butyl-3-methylimidazolium hexafluorophosphate – **C_4mimPF_6**

$C_{10}mimN(Tf)_2$, $C_4mimN(Tf)_2$, C_4mimPF_6 were synthesised by Dr J. Sirieix-Plenet CNRS (France)

Tetrabutylammonium perchlorate – **TBAP,** prepared by metathesis of $(C_4H_9)_4NBr$ with $HClO_4$, Fluka, and recrystallised twice from water and dried under reduced pressure at 100°C for 24 h

Tetrahexylammonium perchlorate – **THxAP**, Fluka

Tetraoctylammonium perchlorate – **TOAP**, Fluka

2-nitrophenyloctylether – **NPOE**, Fluka

KNO_3, KCl, KOH, KBr, NaF, $K_4Fe(CN)_6$, POCh

KPF_6, $NaFB_4$, Merck

$NaClO_4$, NaSCN, Aldrich

methanol, ethanol, hexane, 2-propanol, POCh

hydrochloric acid, *orto*-phosphoric acid, perchlorate acid, POCh

All chemicals were used as received. Water was purified by an ELIX system (Millipore).

Carbon hydrophobic nanofibres – **CNFs** (150-200 nm), synthesised by M.A. Murphy from Loughborough University (UK)

Silicon dioxide hydrophobic nanoparticles Aerosil R812 – **SiO_2** (d = 7 nm), ETC Group

tin-doped indium oxide nanoparticles as water suspension – **ITO_{part}** (d = 21 nm), NanoTek

The gold plates (Au vacuum deposited on glass slides) for IR experiments were purchased from Arrandee.

Reference electrodes: tungsten oxidised wire – W (d = 0.5 mm) or saturated calomel electrode – SCE, REF401, Radiometer, Ag|AgCl|$KCl_{sat.}$ n-Lab.
Counter electrode: platinum wire (d = 0.5 mm)
Working electrodes: gold disc (d = 1.6 mm) in Kel-F, n-Lab; **ITO** coated glass (d = 5.0 mm, resistivity 30 Ohm per square), Image Optics Ltd.

5.7.2. Procedures

Sol preparation

The MTMOS stock sol was prepared by the method similar to the one described in ref. [199]. The hydrolysed sol was prepared by mixing 1.0 ml of MTMOS with 1.5 ml of methanol. After the addition of 50 μl of concentrated HCl it was sonicated for 2 min. The resulting mixture was diluted with methanol in 1:100, 1:1000 and 1:10000 volume ratios and sonicated for another 2 min.

Self- ssembly of theMPS layer was conducted by immersion of electrode for 21 h into 0.3 mol·dm^{-3} the solution of MPS in ethanol [83]. The degree of gold surface coverage was controlled by cyclic voltammetry (Chapter.6.1).

The MPS sol was prepared by the method described in ref. [83]. To a 0.3 mol dm^{-3} solution of MPS in ethanol 50 μl of concentrated HCl was added and sonicated for 2 min.

The stock MTMOS sol solution was diluted 1:10 with methanol and sonicated for 2 further minutes. Then 10 mg of hydrophobic SiO_2 and 40 mg of CNFs were added and the mixture was further sonicated for 2 minutes.

The ITO nanoparticle dispersion in water was dried and re-dispersed in methanol to obtain a 3 wt.% suspension.

Electrode preparation

Prior to each use the Au disc was polished with a 1 μm alumina dispersion in deionised water, sonicated for 10 min in deionised water and finally washed with hot redistilled water. Au covered glass plates were treated by concentrated HNO_3 for 20 min, washed with water and extensively washed with hot water. Finally they were immersed into methanol and dried.

The ITO and glass supports were cleaned by rinsing the electrodes in ethanol and water, then furnace treated at 500 °C in air for 60 minutes. The ITO and glass electrode area was defined by masking off an area with scotch tape.

Table.1 contains a brief description of the electrode preparation steps. More details will be given in Chapter6.1.

Tabele.1. Electrode preparation

Electrode	**Method**	**Procedure**
Au|$MTMOS_{gel}$	sol-drop deposition	5 μl of MTMOS sol 1:1000
Au|MPS|$MTMOS_{gel}$	sol-drop deposition	21 h in MPS solution and 5 μl of MTMOS sol 1:1000
Au|MPS_{gel}	sol-drop deposition	5 μl of MPS sol 1:1000
ITO|$MTMOS_{gel}$	dip-coating	immersed to and pulled out from the MTMOS stock sol solution with speed 85 mm min^{-1}
glass|$MTMOS_{gel}$|Au_{ev}	dip-coating	immersed to and pulled out from the MTMOS stock sol solution with speed 85 mm min^{-}; gold evaporation
ITO|CNF,SiO_2,$MTMOS_{gel}$	sol-drop deposition	4 μl of mixture with CNFs
ITO|ITO_{part}|$MTMOS_{gel}$	dip-coating	layer by layer deposition from ITO nanoparticles 3 wt.% suspension in methanol solution with speed 85 mm min^{-1}; immersed to and pulled out from the MTMOS sol 1:100 with speed 85 mm min^{-1}

The modified electrode was left for drying at least 24 h at room temperature.

The solvent evaporation method was used for modification of the electrode surface with *t*BuFc or DDPD solution in hexane.

Drop deposition was used for modification of the electrode surface with RTILs or *t*BuFc in NPOE solutions

The gold plates used as support for SEM, AFM and FTIRRAS experiments were modified in the same way as the gold disc electrode. To obtain the film a proportionally larger amount of MTMOS or MPS sol 1:1000 was cast on the Au coated glass plate. The modified surfaces were left for drying at least 24 h at room temperature for film formation.

5.7.3. Instrumentation

FTIR and **FTIRRAS** spectra were measured by an FTIR 8400 Shimadzu spectrometer. FTIR spectra of the liquid gel precursors: MTMOS and MPS spectra were recorded as thin liquid films between KRS-5 plates. The spectra of bulk MPS were obtained in KBr pellets. The reflectance spectra of silicate films were obtained using the variable angle reflectance accessory model 500 from SpectraTech Inc. The incidence angles was varied from 25 to 80 degrees with respect to the surface normal.

AFM experiments were done by means of the commercial instrument TMX 2000 'Discoverer' (Topometrix, CA) in constant (repulsive) and constant force modes. Standard silicon nitride tips and 25 μm scanner were applied. All scans were performed under ambient conditions. Samples were placed underneath the AFM system directly after the preparation procedures. For each sample several images at various positions were collected to gain more information about local structure.

SEM images were done on a Hitachi S3500N whereas roentgenographic microanalysis was performed on energodispersive Roentgen spectrometer (VANTAGE THERMO NORMAN) with a sensitivity of 0.3 at. %; system at Warsaw University of Technology, Faculty of Materials Science and Engineering, Poland.

FEGSEM images were obtained at a Leo 1530 system at Loughborough University, Institute of Polymer Technology and Materials Engineering, UK.

DIP-COATING for nanoparticulate layers and film deposition a KSV dip-coating unit (KSVInstruments Ltd.) was employed.

CV, CA and **DPV** experiments were done with an Autolab (Eco Chemie) electrochemical system in a conventional three-electrode cell with dedicated software.

Furnace for ITO electrode cleaning Elite tube furnace, model TSH 12/65/550

6. Results and discussion

As was mentioned above the electrode surface modification with redox liquid droplets have been known since 1997 [133]. The electrochemical process of such unsupported deposits takes place predominantly at the three phase junction, electrode | redox liquid | aqueous solution. Therefore the extension of this boundary is highly desirable to maximise the current response. Such a system gives a stable voltammetric response only when the neutral droplets are deposited on the electrode, and the charged species forming after the electron exchange reaction are insoluble in aqueous solutions. Otherwise an unstable voltammetric behaviour is observed [137,144].

The stability of the voltammetric response and the enhancement of the electrode reaction efficiency (defined as the ratio of the Faradaic charge to the electric charge corresponding to complete electrochemical conversion of the deposited redox liquid) and can be realised by the development of a suitable electrode support (Fig.44, 45). It was our idea that a thin hydrophobic silicate film can improve the first factor. The strong affinity of the redox liquid to the methyl functionalised silicate matrix has been already proven for redox liquid modified hydrophobic carbon ceramic electrodes (CCE) [200]. The experiments with this system also showed that the organically modified silicate matrix acts as a liquid reservoir [200,201]. Therefore in our experiments the MTMOS based matrix was deposited on gold, ITO or glass supports. The main advantage of the film obtained from MTMOS precursor is its hydrophobic porous structure, which can act as a container for a hydrophobic redox liquid. Additionally, the silicate matrix is rich in free pairs of electrons present on oxygen atoms, which can stabilise the cationic form of the redox probe within the organic phase. Poor adhesion of MTMOS to hydrophilic gold may result in an unstable electrode performance because of peeling of the matrix from the electrode. However, one may take advantage of -SH groups adsorbing spontaneously on a gold support [202]. That is why in some experiments 3-mercaptopropyltrimethoxysilane (MPS) was anchored to the gold surface before the silicate film deposition. MPS layer rich in Si-OH groups is allowed to react with the MTMOS precursor and finally forms a matrix stronger bonded to the electrode support.

The low efficiency of the redox liquid electrode process on these electrodes represents another problem. This can be connected with partial blocking of the electrode surface and relatively short length of the three phase junction. This problem was solved

here by development of an extended conductive surface done in two ways. First by immobilisation of conductive nanoobjects, like carbon nanofibers (CNF) or ITO nanoparticles into the hydrophobic silicate film on the electrode support. In these experiments ITO electrode was used, because of good silicate and ITO particle adhesion to this surface. Deposition of an imperfect conductive gold layer onto the hydrophobic silicate film placed on nonconductive glass support represents a second approach.

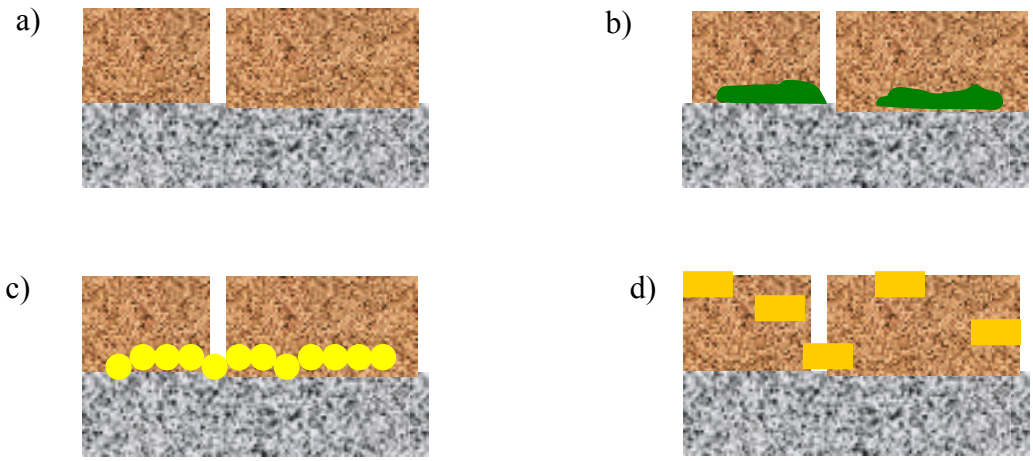

Fig.44. Scheme of cross sections of proposed electrode configurations a) silicate film, b) silicate film on the top of precursor layer c) silicate film with embedded nanoobjects and d) silicate film with imperfect gold layer on top.

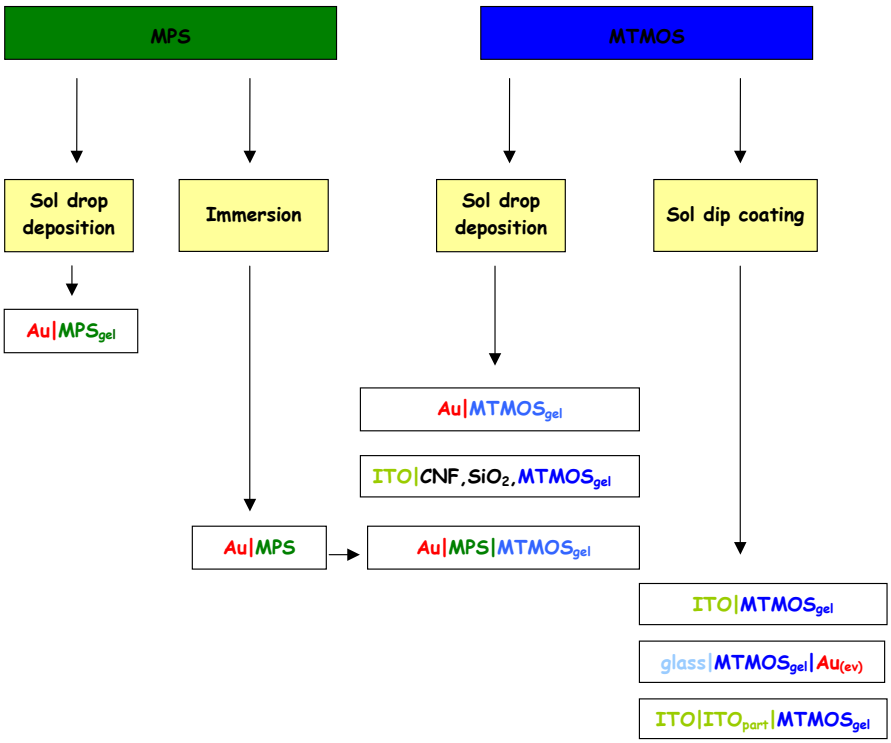

Fig.45. The overview of the prepared and studied electrodes.

6.1. Surface modification and optimisation

The surface of the electrodes was modified by a one or two step method.

The one step method involves the sol drop deposition or sol dip coating process. The sol was prepared by a method similar to that described in ref. [199]. Typically the hydrolysed stock (I) sol was prepared by mixing 1.0 ml of MTMOS with 1.5 ml of methanol. After addition of 2 μl of concentrated HCl as catalyst it was sonicated for 2 minutes. The stock (II) sol solution was prepared by mixing 57 μl of MPS with 1.0 ml of ethanol and 2 μl of concentrated HCl and finally sonicated for 2 minutes [83].

The stock (I) and (II) sols were diluted with methanol in 1:100, 1:1000 and 1:10000 volume ratios and sonicated for 2 minutes. 5 μl of this solution was deposited onto gold discs to prepare **Au|MTMOS$_{gel}$** or **Au|MPS$_{gel}$** electrodes.

In preliminary experiments the effect of sol dilution on the magnitude of the voltammetric response of the redox liquid deposit was studied. **Au|MTMOS$_{gel}$** electrodes were modified with 1.9 nmol of *N*,*N*-didodecyl-*N'*,*N'*-diethylphenylenediamine (DDPD) and immersed into 0.1 M $KClO_4$ solution. DDPD was chosen for the reason that its electrogenerated cation is water insoluble [135]. Sharp and well defined voltammetric peaks are found for the films obtained from 1:1000 and 1:10000 diluted sols (Fig.46). After tenth scan the most stable voltammograms are obtained for the first electrode. A substantially smaller peak current is recorded for the electrode modified with 1:100 sol. It seems that a more compact film is obtained at this electrode. One can conclude, that in the first two cases, the electrode surface is only partially blocked and more three phase junctions are formed. Therefore for further experiments a 1:1000 diluted sol was used for electrode modification.

The dip coating method was also used for film deposition on the ITO electrode. The electrode was immersed and pulled out from the stock sol solution with the speed 85 mm min^{-1} and the **ITO|MTMOS$_{gel}$** electrode was prepared. The same procedure was used to obtain MTMOS thin film on glass support. To provide electric contact a thin layer of porous gold with a thickness about 20 nm was evaporated on the top and the **glass|MTMOS$_{gel}$|Au$_{ev}$** was prepared.

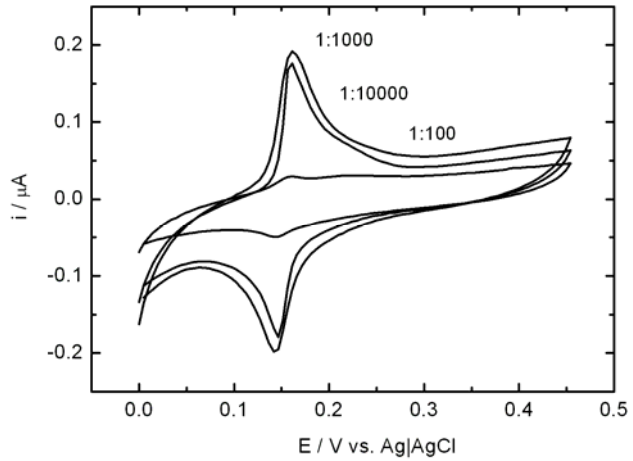

Fig.46. Cyclic voltammograms obtained with Au|MTMOS$_{gel}$ electrodes (surface area 0.02 cm^2) obtained from sol diluted with methanol in 1:100, 1:1000 and 1:10000 ratio, modified with 1.9 nmole of DDPPD and immersed in aqueous 0.1 mol dm^{-3} KClO$_4$ aqueous solution. Scan rate 10 mV s^{-1}.

The sol drop deposition was also employed for preparation of the silicate film with embedded interwoven carbon nanofibres. Unfortunately, as was judged by naked eye, significant CNFs aggregation occurs. In order to avoid this phenomenon 7 nm diameter SiO_2 nanoparticles were added to the sol. This improved the CNFs solubility and prevented their re-aggregation during the sol-gel process. In typical procedure the stock sol solution was diluted with methanol in 1:10 ratio and sonicated for 1 minute. After than 10 mg of hydrophobic silica particles and 40 mg of CNFs was added and sonicated for another 2 minutes. For film preparation 4 μl of mixture was deposited onto the ITO surface and **ITO|CNF,SiO$_2$,MTMOS$_{gel}$** electrode was produced.

In the two step method the deposition of a hydrophobic matrix was preceded by the MPS self assembly on the gold electrode or by layer-by-layer deposition of ITO nanoparticles on ITO support. In the first case bare gold disc electrodes were premodified by immersion into a 0.3 mol dm^{-3} MPS in ethanol solution. In this case the chemisorption of SH groups at the Au electrode is expected to occur [83] and the **Au|MPS** electrode is formed. The degree of thiol adsorption was controlled by CV in aqueous 0.001 mol dm^{-3} $Fc(CH_2OH)_2$ solution. Decrease of the peak current (I_p) and increase in the anodic peak (E_a) to cathodic (E_c) peak separation (ΔE_p) indicates that the electrode surface was partially blocked [83]. On this basis a procedure involving 21 hours of electrode immersion in MPS solution when a 20% decrease of I_p was observed was chosen arbitrarily (Fig.47). It should be emphasised that part of the electrode

surface remains electrochemically active, presumably not blocked. After rinsing and overnight drying the **Au|MPS** was modified by deposition of 5 μl of diluted MTMOS sol 1:1000 in methanol (one step method described above).

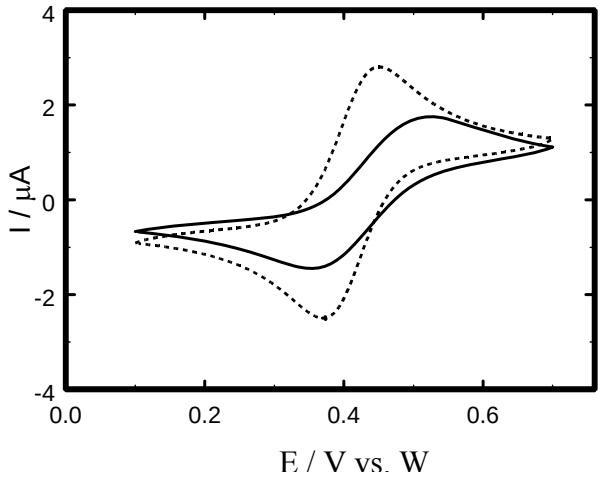

Fig.47. Cyclic voltammograms obtained with bare Au (dashed) and Au|MPS (solid) electrodes immersed in 0.001 mol dm^{-3} $FcCH_2OH$ and 0.1 mol dm^{-3} KNO_3 aqueous solution. Scan rate 50 mV s^{-1}; surface area 0.02 cm^2.

The layer by layer deposition of ITO nanoparticles was realised by ITO electrode immersion in and withdrawal from a suspension containing 3% wt. ITO nanoparticles in methanol solution. Both processes were performed with a speed 85 mm min^{-1} of withdraw. This step was repeated from 1 to 12 times. Each one was followed by drying and dipping in methanol. After that the electrode was immersed into MTMOS sol solution diluted in 1:100 ratio with methanol and **ITO|ITO$_{part}$|MTMOS$_{gel}$.** electrode was prepared.

Finally after preparation procedure all electrodes were left for at least 24 hours for drying and film formation.

6.2. Infrared spectroscopic characterisation of silicate film

FTIR and FTIRRAS spectroscopy were employed to verify the polymer network formation. This is possible through comparison of the transmittance and the reflectance spectra and assigned the signals to formed functional groups and bonds. Also the latter method allows to get some information about the defects in silicates matrixes. For this purpose transmittance spectra between KRS-5 plates of MTMOS and MPS precursors were done. The reflectance spectra of the MTMOS$_{gel}$, MPS$_{gel}$ and MPS|MTMOS$_{gel}$

films on glass slides covered by gold layer of were obtained at variable angles from 25° to 80° with respect to the normal surface. It was expected that the change of support or nanoobjects embedding in silicate matrix does not affect Si-O-Si bonds formation. For this reason only three above mentioned films were examined by IR spectroscopy.

6.2.1. Au|MTMOS$_{gel}$

Fig.48 compares FTIR spectra of the sol-gel processed MTMOS based film on the gold surface and its precursor. The detailed band assignment [203,204] is given in Table.2. The bands originating from Si-O-CH_3 groups of MTMOS precursor are replaced by Si-O-Si modes in the film spectrum indicating silicate network formation. Relatively intense band at 900 cm^{-1} indicates that significant amount of unreacted Si-OH groups are left. The broad bands at 1625 and 3320 cm^{-1} originate probably from mixed contributions of Si-OH and water trapped during the gelation process.

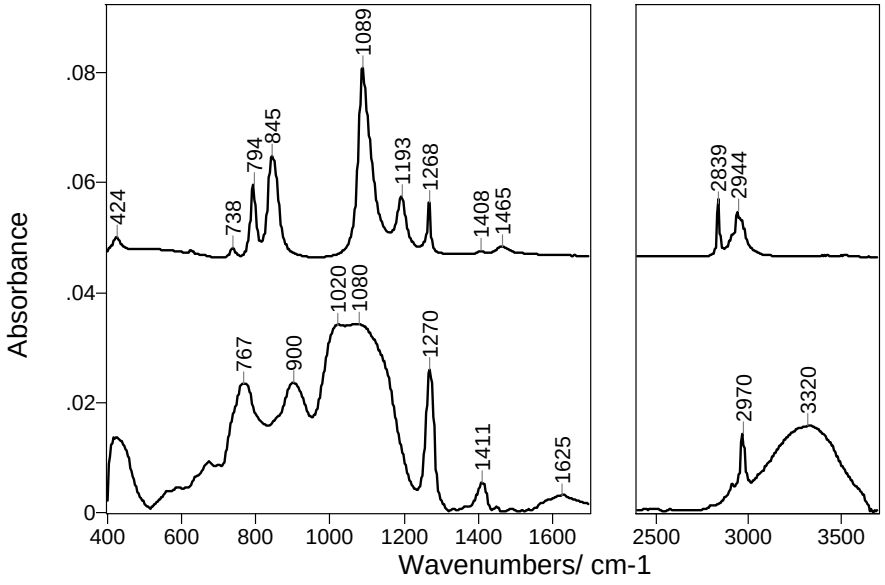

Fig.48. FTIR spectra of MTMOS precursor (a) and Au|MTMOS$_{gel}$ sample recorded in the reflectance mode under 25° incidence angle(b).

Table.2. IR band positions (cm^{-1}) and assignments.

MTMOS	MTMOS gel	MPS	MPS gel	Assignments [a]
424	424	463	463	δ_{oSiOC}, δ_{oSiOSi}
			690	δ_{rCH2}
738		756	756	ν_{Si-C}
	767		802	$\nu_{sSi-O-Si}$
794		812		$\nu_{sSi-O-C}$
845				δ_{rCH3} Si-CH_3
	900		884	ν_{Si-O} Si-OH
	1020/1190		1025/1186	$\nu_{asSi-O-Si}$
1089		1089		$\nu_{asSi-O-C}$
1193		1193		δ_{sCH3} OCH_3
1268/1408	1270/1411			δ_s/δ_{as} Si-CH_3
		1240/1260 1307,1340 1410/1456	1240/1260 1307,1340 1410/1456	δ_{CH2} Si-C_2H_4SH
1465		1456		δ_{asCH3} OCH_3
	1625		1625	δ_{bOH} Si-OH and H_2O tr.
		2550	2555	ν_{SH}
2839		2839		ν_{CH} OCH_3
			2852/2926	ν_{CH} CH_2
2944	2970	2944		ν_{CH} Si-CH_3
	3320		3350	ν_{OH} Si-OH and H_2O tr.

[a] δ_o, δ_r, ν, δ and δ_b denote out-of-plane deformation, rocking, stretching and bending modes respectively; as and s denote asymmetric and symmetric modes.

The Si-O-Si asymmetric stretching band ($\nu_{asSi-O-Si}$) consists of multiple components. This effect was extensively studied for SiO_2 glasses [112,205,206,207], sol-gel derived silica [68,79,121] and plasma-deposited siloxane films [204]. The band splitting originates from the mechanical coupling between adjacent Si-O-Si groups and long-range Coulombic interactions [205]. The mechanical coupling divides the $\nu_{asSi-O-Si}$ mode

into the in-phase (AS1) and out-of-phase (AS2) components. The Coulombic interactions originate from dipole charge motions within the Si-O bond network. The vibrations parallel to the propagation of the network oscillating movement give rise to longitudinal-optic (LO) components of IR bands, whereas the perpendicular motions generate transverse optic (TO) components. The frequency shift between these two components provides a qualitative information on the sample density, porosity and the number of defects of silicate network [204,205]. The bigger incidence angle the higher intensity of LO modes [207]. Therefore to identify TO and LO modes for MTMOS gel, the infrared reflectance spectra were measured at various incidence angles (Fig.49). The intensity of 1151 and 1190 cm^{-1} components of the $\nu_{asSi\text{-}O\text{-}Si}$ band increase noticeable upon increase of the incidence angle and they were assigned to AS1-LO and AS2-LO modes respectively. The 1020 and 1080 cm^{-1} bands correspond to AS1-TO and AS2-TO modes correspondingly.

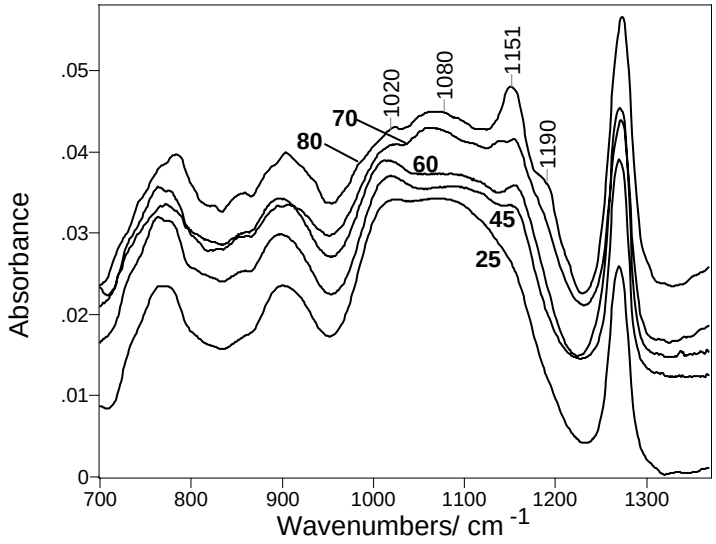

Fig.49. FTIR reflectance spectra of Au|MTMOS$_{gel}$ sample obtained at various angles of incidence. The incidence angles: 25, 45, 60, 70 and 80° are indicated on the figure.

6.2.2. Au|MPS$_{gel}$

Fig.50 compares FTIR spectra of the MPS based thick film sol-gel processed on glass used as reference for bulk MPS based gel and analogous thin film sol-gel processed on the gold surface and its precursor. Similarly, like for Au|MTMOSgel system the Si-OCH_3 modes are replaced by bands characteristic for Si-O-Si and Si-OH

components. The presence of SH group in the MPS gel is verified by the presence of 2555 cm^{-1} band [208,209]. This indicates that only fraction of these groups reacts with Au and film is composed of Si-O-Si network with OH and C_3H_6SH functional groups. The differences between Au|MPSgel and Au|MTMOSgel spectra comprise a number of CH_2 deformation bands at: 690, 1240/1260 (doublet), 1307, 1340, 1410 and 1456 cm^{-1}. The CH_2 groups give also strong high frequency bands at 2852 and 2926 cm^{-1} due to symmetric and antisymmetric stretching modes respectively. The LO and TO components of the $\nu_{asSi\text{-}O\text{-}Si}$ band have been identified by recording the reflectance spectra at various incidence angles, similarly as for MTMOS gel. The distance between the AS1-TO and AS1-LO component is by 9 cm^{-1} smaller comparing to MTMOS gel film indicating larger number defects in the MPS gel film structure.

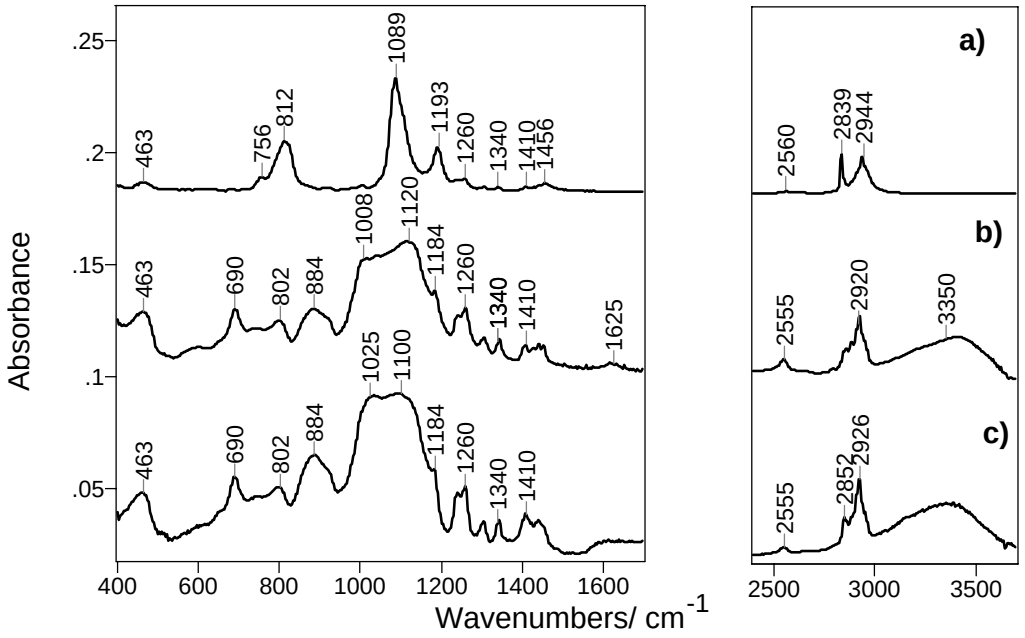

Fig.50. FTIR spectra of MPS precursor (a) MPS_{gel} cast onto a glass plate (b) and $Au|MPS_{gel}$ sample recorded in the reflectance mode under 25° incidence angle (c).

6.2.3. Au|MPS|$MTMOS_{gel}$

The spectrum of the MTMOS sol-gel processed film deposited on gold premodified with MPS closely resembles that obtained on unmodified gold (Fig.51). The only noticeable difference are CH_2 stretching bands at 2850 and 2920 cm^{-1}. From spectra obtained at various incidence angle the AS1-TO to AS1-LO band frequency difference

was estimated equal 150 cm^{-1}, being thus 20 cm^{-1} smaller than for MTMOS gel film. This indicates that premodification of Au substrate by MPS increases number of defects in MTMOS gel film.

To estimate the number of C_3H_6SH groups as a function of the distance from the gold surface namely to verify sample chemical homogeneity was made. This was done by comparison of the spectra recorded at large angle (70-80°) and near normal incidence of the beam, carrying information about the surface and bulk sample respectively. However, the only visible difference is the change of shape of the $\nu_{asSi\text{-}O\text{-}Si}$ band due to variable LO modes contribution. The lack of dependence of the intensity of CH_2 bands of MPS (normalised to intensity of CH_3 band) on the incidence angle may indicate that the amount of MPS is nearly constant from the top of the layer to the gold surface. This surprising result may be explained by the film surface roughness [210]. The infrared beam is diffused and even for high incidence angles the large part of the beam passes through the sample. Therefore, the spectra recorded at high incidence angle contain large contribution from bulk of the sample.

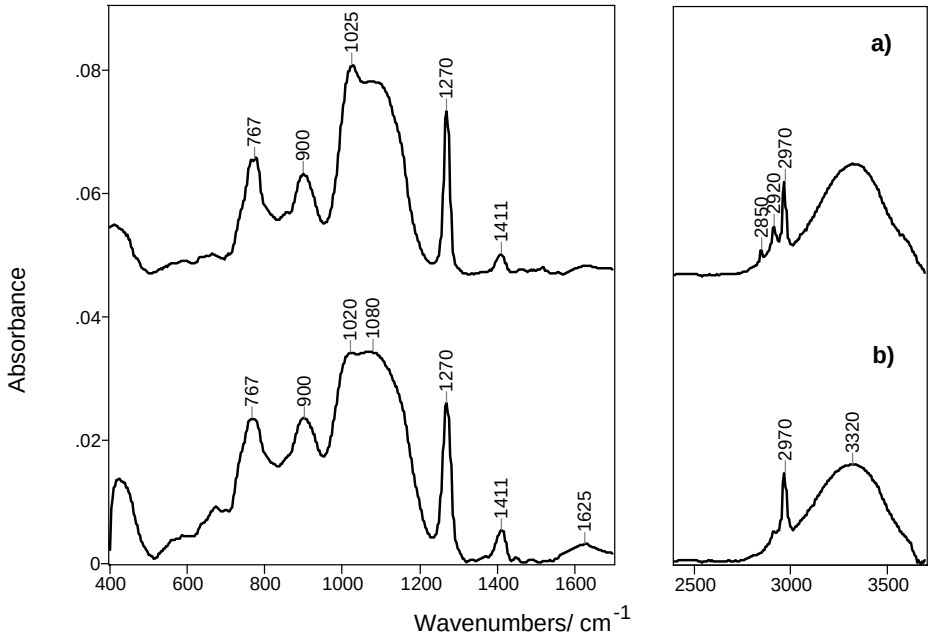

Fig.51. FTIR reflectance spectra (incidence angle 25°) of Au|MPS|MTMOS$_{gel}$ (a) and Au|MTMOS$_{gel}$ samples (b).

Summary the existence of Si-O-Si bounds were proven during silicate formation obtained by sol-gel process. The changes in LO to TO distance confirm the differences in the film structure and show that Au|MPS|MTMOS$_{gel}$ sample is the most defected.

6.3. AFM and SEM Characterisation of Silicate films

In order learn about surface structure of silicate based films the AFM and SEM were employed. As it was said in Chapter 1.4.1 these methods were often used to characterise silicate films. Here the topography of Au|$MTMOS_{gel}$, Au|MPS_{gel}, Au|MPS|$MTMOS_{gel}$ and ITO|$MTMOS_{gel}$, glass|$MTMOS_{gel}$|Au_{ev} electrodes as well as nanoobject embedded in matrixes like ITO|CNF,SiO_2,$MTMOS_{gel}$ and ITO|ITO_{part},$MTMOS_{gel}$ electrodes were studied by these methods.

6.3.1. Au|$MTMOS_{gel}$

AFM image of Au|$MTMOS_{gel}$ show significant differences in film topography comparing to bare gold (Fig.52). In the case of the latter the surface scratches are only visible (Fig.52a). The image of Au|$MTMOS_{gel}$ sample (Fig.52b) reveals relatively flat surface with randomly distributed holes of diameter 200-600 nm. The thickness of the hydrophobic silicate film was estimated from the height of naturally formed film|substrate step boundary and it is equal ca 250 nm (Fig.53).

Similarly, the FEGSEM image of Au|$MTMOS_{gel}$ demonstrates the number of defects in silicate films (Fig.54a).

6.3.2. Au|MPS_{gel}

The topography of the films prepared from MPS precursor is quite different. Although as judged from AFM image single holes can be observed on the image of this sample (Fig.52c) it is mainly dominated by species sticking out of the surface.

Also SEM image shows that topography depends on the film composition (Fig.55a). The sticking out objects can be also found. Identification of the elements by SEM (Fig.55a) and surface roentgenographic analysis (Fig.55b) show that these protrusions are rich of sulphur, whereas between these features this element was not identified. It may indicates that presence of MPS promotes their growth.

6.3.3. Au|MPS|$MTMOS_{gel}$

The randomly distributed protrusions are better developed on Au|MPS|MTMOSgel sample (Fig.52d). Their dimensions are 200-600 nm in width and 50-200 in height with larger dimensions for Au|MPS|MTMOSgel sample. It has to be emphasized that their

width may be well overestimated due to broadening out by the shape of the tip. The isolated holes are also visible on the image of this sample.

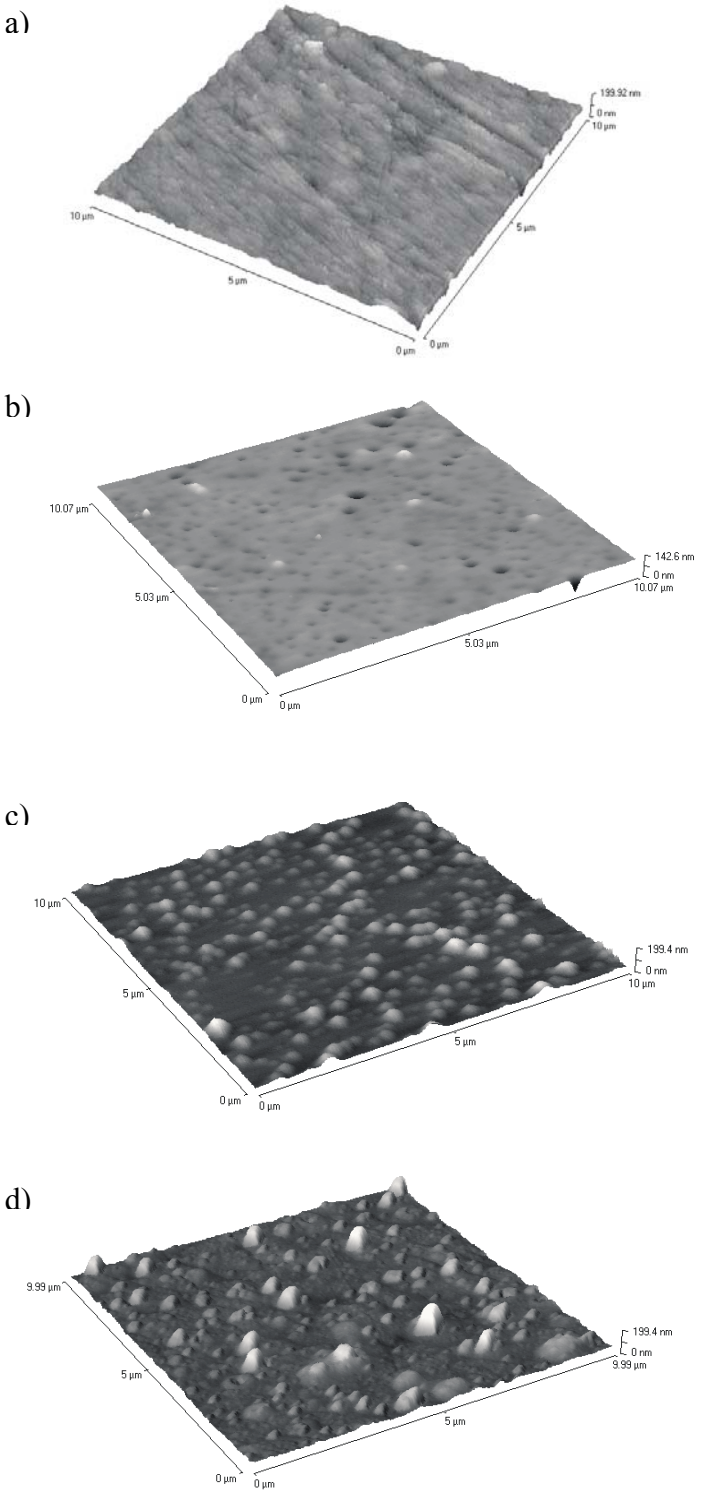

Fig.52. Comparison of AFM images (3D view) obtained for (a) Au, (b) Au|MTMOS$_{gel}$, (c) Au|MPS$_{gel}$ and (d) Au|MPS|MTMOS$_{gel}$ samples. Scanning area 10 × 10 µm .

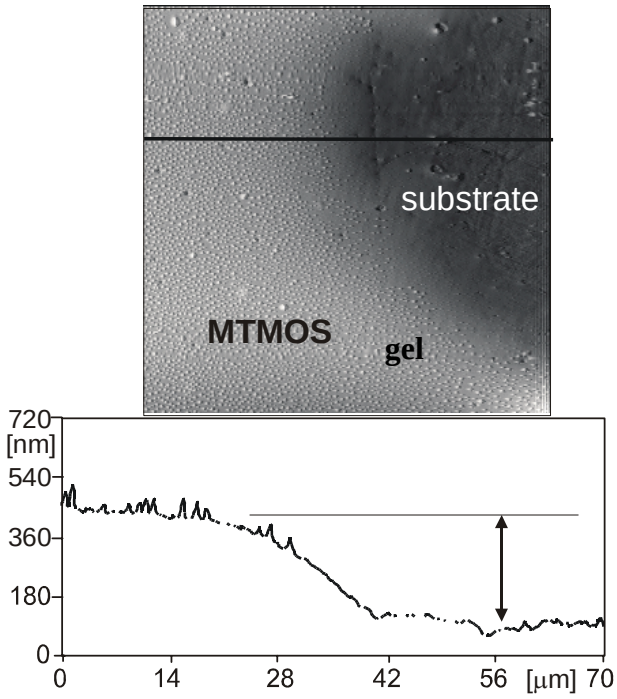

Fig.53. Linear profile used for estimation of Au|MTMOS$_{gel}$ film thickness together with 2D image of this part of the surface. Solid line shows track of profile.

It is clear that relatively uniform film is obtained on Au surface from MTMOS. On the other hand sol-gel process of MPS results in non-uniform growth of the film rich of protrusions. Interestingly premodification of Au with MPS results in even more developed three dimensional geometry of MTMOS film. This happens despite the absence of catalyst in premodifying MPS solution being necessary condition for silicate film formation. Probably defective layer of MPS serves as support for MTMOS based silicate formation started by cocondensation of MTMOS molecules on MPS based silicate surface. Finally, one can summarise that the structure of the film depends on precursor and the number of defects increases according to Au|MTMOS$_{gel}$, Au|MPS$_{gel}$ and Au|MPS|MTMOS$_{gel}$ order. The difference in structure observed in AFM experiments is in qualitative agreement with results obtained from FTIRRAS experiments (Chapter 6.2).

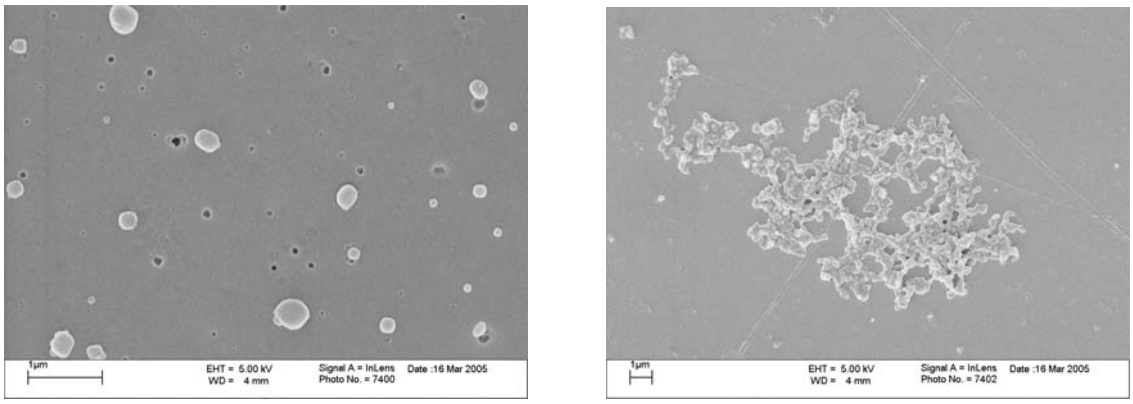

Fig.54. FEGSEM images of a) Au|MTMOS$_{gel}$ and b) Au|MPS|MTMOS$_{gel}$ films.

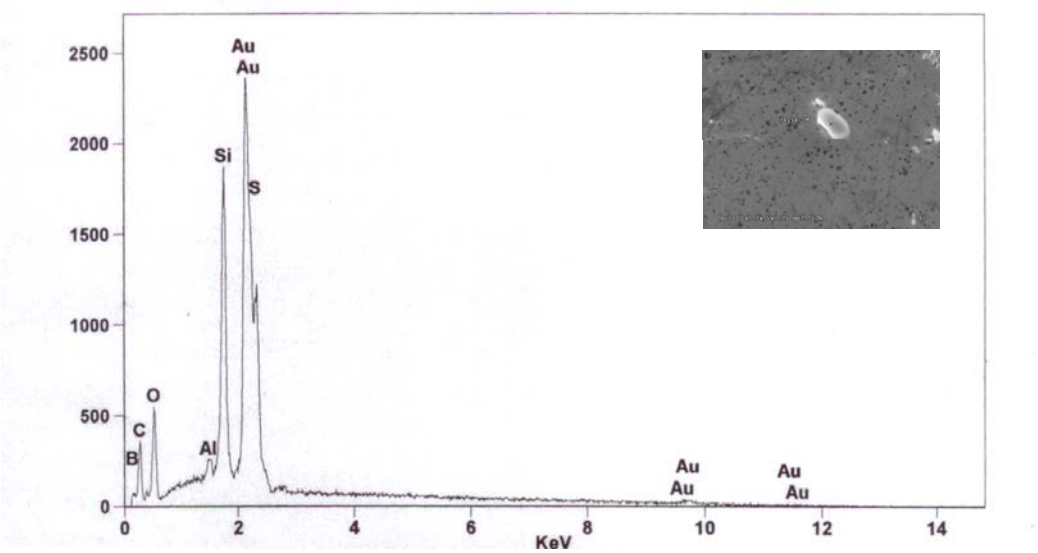

Fig.55. a) SEM image of Au|MPS$_{gel}$ film, b) roentgenographic analysis of the elements present on protrusion surface.

6.3.4. ITO|MTMOS$_{gel}$

The FEGSEM images of MTMOS based gel deposited on ITO electrode via dip coating revealed film formation. The surface is smooth and film thickness is equal approximately 200 nm (Fig.56). However, one has to take into account that micropores are too small to be seen directly by this technique.

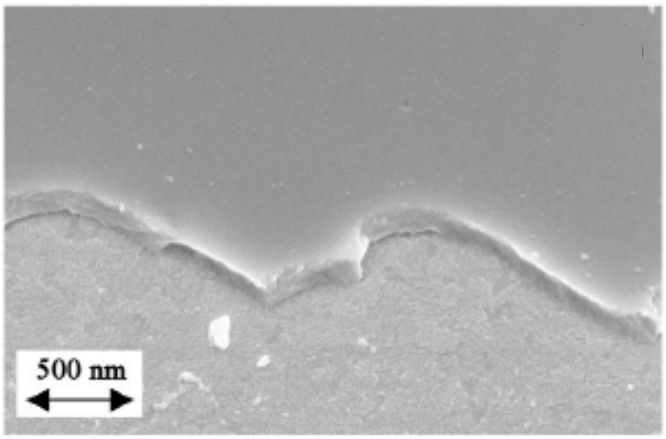

Fig.56. FEGSEM image of ITO|MTMOS$_{gel}$ film.

6.3.5. glass|MTMOS$_{gel}$|Au$_{ev}$

Similarly as on ITO electrode the MTMOS based film was coated also onto glass support. This film was later covered by evaporated gold. MTMOS$_{gel}$ and Au layers approximately 200 and 20 nm thick are visible on FEGSEM image of glass|MTMOS$_{gel}$|Au$_{ev}$ (Fig.57). On the top of the film some protrusions and holes are visible.

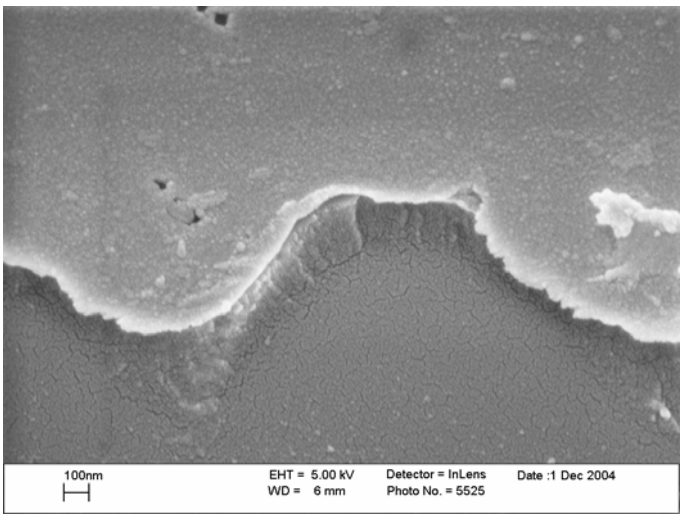

Fig.57. FEGSEM image of glass|MTMOS$_{gel}$|Au$_{ev}$ film.

6.3.6. ITO|CNF,SiO_2,$MTMOS_{gel}$

FEGSEM images of ITO|CNF,$MTMOS_{gel}$ electrode are shown in Fig.58. At low magnification globular deposits up to 100 μm diameter can be seen (Fig.58A). Closer inspection (Fig.58B) reveals the presence of densely packed carbon nanofibres and silica nanoparticles. Both particles and fibres are clearly visible in Fig.58C and the structure can be seen to be essentially mesoporous.

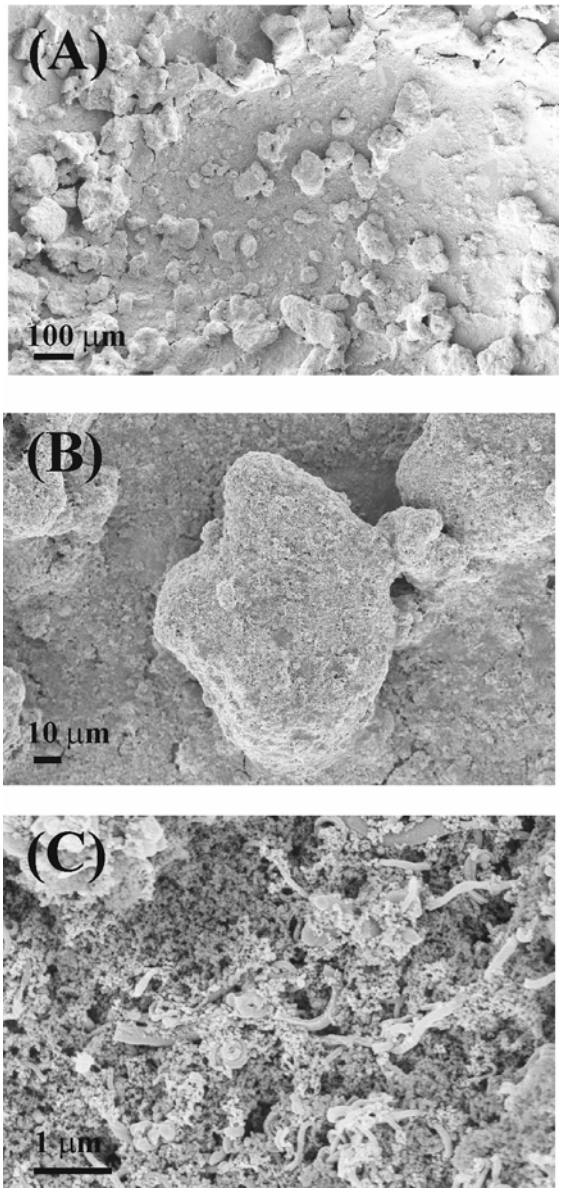

Fig.58. FEGSEM images of the surface of ITO|CNF,$MTMOS_{gel}$ at (A) low, (B) intermediate, and (C) high magnification.

6.3.7. ITO|ITO$_{part}$

For ITO particles modified electrode AFM and FEGSEM images were taken before silicate film deposition. They show well developed surface of ITO nanoparticles film (Fig.59, 60). Together with increasing number of ITO nanoparticles layers, the size of aggregates became bigger. The thickness of coating was estimated as about 40 and 120 nm for one and three layers, respectively by the AFM. This indicates that applied preparation procedure allows to prepare layer on layer film with single layer thickness equal about 40 nm. This is about twice of the diameter of nanoparticles. Interestingly this film was deposited without organic binder employed earlier for TiO_2 nanoparticles modified electrodes [211,212]. However, contrary to the latter film ITO nanoparticles films are not homogeneous.

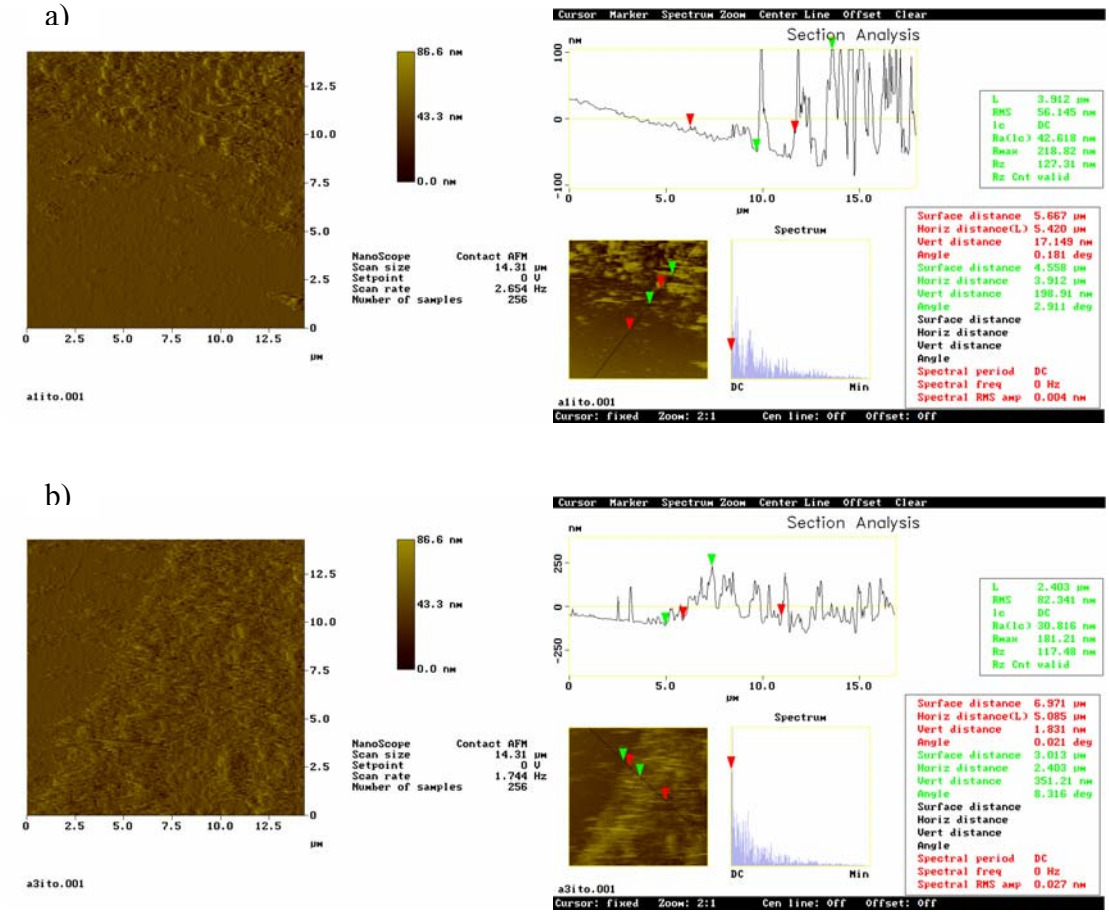

Fig.59. AFM images of the surface of ITO|ITO$_{part}$ a) one layer of ITO particles b) three layers of ITO particles.

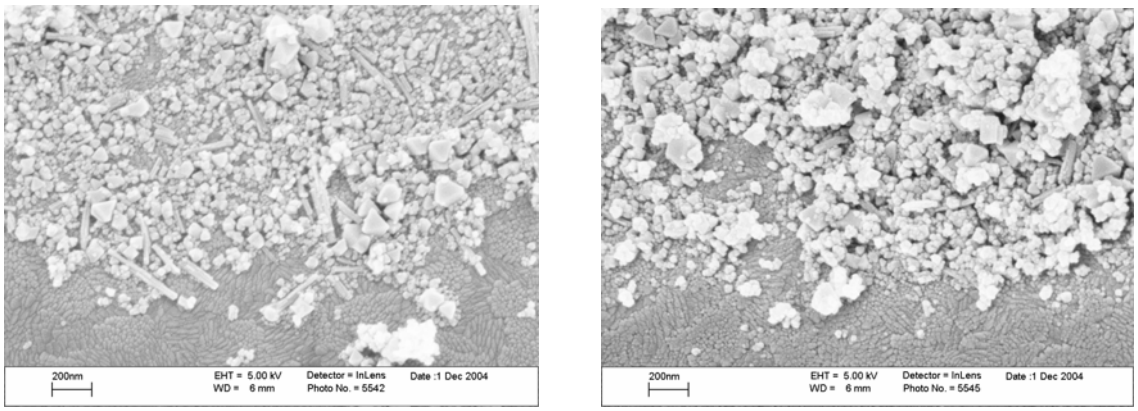

Fig.60. FEGSEM images of the surface of ITO|ITO_{partl} a) one layer of ITO particles b) three layers of ITO particles.

Summarising, in this paragraph the procedures of thin silicate film preparation on the electrode surface were presented. The FTIRRAS method spectra proved the existence of silicate network and film heterogeneity. From the AFM and SEM images the topography of the surface was assessed. The film structure depends on precursors used and type of embedded particles. The structure of the most of the prepared films is clearly heterogenous. This heterogeneity is promoted by the use of MPS precursor. Obviously embedding of nanoobjects in silicate matrix considerably develops the surface. In this case hydrophobic silicate functions as a binder for nanoobjects and changes hydrophobic/hydrophilic properties of the electrode surface. The well-known aggregation of nanoparticles is limited by applying SiO_2 nanoparticles as "nanosurfactants". The rough and hydrophobic surface can be useful for hydrophobic redox liquid immobilisation.

6.4. Permeation through the film from aqueous solution

Before modification of the studied electrodes with the redox liquid the permeation of the deposited layer by species dissolved in solution was examined by CV. This method was already used extensively to characterise sol-gel processed films [79,83,208]. For simple electrode reactions involving transport process and heterogeneous electron transfer the change of voltammograms provides information about film penetration by ions and molecules, thereby giving information about film quality. For completely blocked surface with thickness larger than few nanometers one expect suppression of voltammetric peaks [83]. This is because electron transfer is severely inhibited due to extensively long tunnelling distance. Not complete coverage of the metal surface results only in some decrease of the current and the change of the shape of voltammogram (Fig.47). For porous nonelectroactive film CV response may turn from peak-shaped to the sigmoidal signal together with the current decrease. This indicates the transistion form linear to hemispherical diffusion [79]. This is because only small sized parts of the electrode surface with small area are accessible by the redox probe.

The permeation of silicate films deposited on electrode surface was checked by CV experiments with two redox probe with different charge and size. In typical experiment, the neutral, $Fc(CH_2OH)_2$ or an anionic $Fe(CN)_6^{4-}$ probe was present in 1 mol dm^{-3} aqueous solutions. Both of them undergoes reversible and relatively fast one electron exchange reaction [68]. Their electrooxidation can be described by eq.24 and eq.25. Already Collinson results indicate [68], that $Fc(CH_2OH)_2$ directly crosses tetramethoxysilicate based hydrophilic film, but negatively charged $Fe(CN)_6^{3-}$ cannot easily diffuse through the matrix, thus little Faradaic current can be observed for this redox probe. It was expected, that for hydrophobic films $Fc(CH_2OH)_2$ will not interact with silicate film and can access the electrode surface, while the polar $Fe(CN)_6^{4-}$ will be repelled from the matrix.

$$Fc(CH_2OH)_2 \leftrightarrow Fc(CH_2OH)_2^{+} + e \qquad (24)$$

$$Fe(CN)_6^{4-} \leftrightarrow Fe(CN)_6^{3-} \qquad (25)$$

In the case of Au|MTMOS$_{gel}$, Au|MPS$_{gel}$ and Au|MPS|MTMOS$_{gel}$ electrodes for both redox probes the peak currents are suppressed in comparision to bare Au (Fig.61) with more pronounced effect for anionic redox probe [68,121]. This may be explained by weaker penetration of the film by anionic substrate, because of repulsive interactions between polar solute and hydrophobic silicate matrix (see above). The effect of gel composition is similar for both redox probes. The peak currents decrease in the order Au > Au|MTMOS$_{gel}$ > Au|MPS$_{gel}$ > Au|MPS|MTMOS$_{gel}$ for Fc(CH$_2$OH)$_2$) and Au > Au|MTMOS$_{gel}$ > Au|MPS|MTMOS$_{gel}$ > Au|MPS$_{gel}$ for $Fe(CN)_6^{4-}$. The change of the shape of voltammogram from peak shaped (Au|MTMOS$_{gel}$) to sigmoidal (Au|MPS$_{gel}$ and Au|MPS|MTMOS$_{gel}$) together with the current decrease indicates not only decrease of the Au surface accessible for Fc(CH$_2$OH)$_2$, but also smaller size (≈ 20 μm) of defects in silicate matrix. The increase of voltammetric response was not observed for Au|MPS$_{gel}$ electrode in the presence of an anionic redox probe as it was described in [80]. The $Fe(CN)_6^{4-}$ redox probe is repulsed from this matrix. This also indicates that thiol groups repel anionic redox probe.

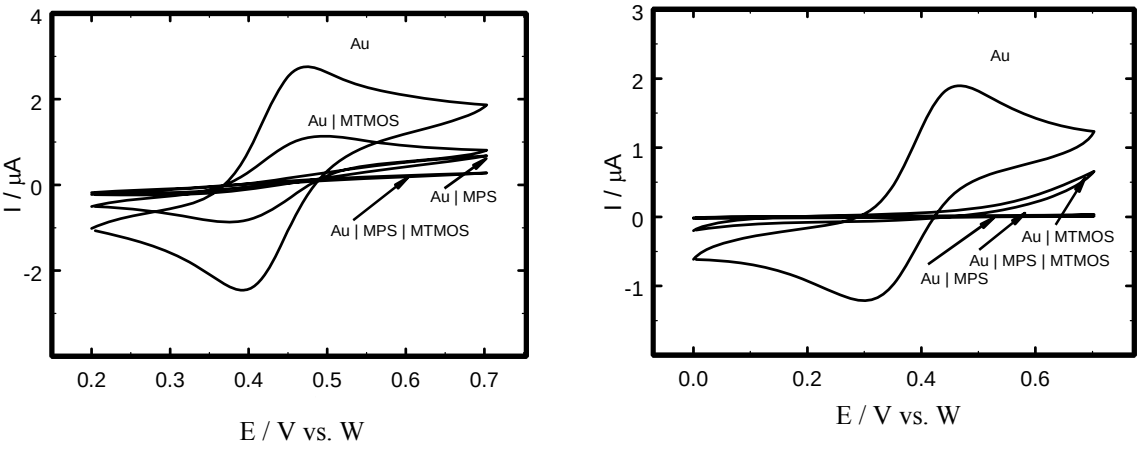

Fig.61. Cyclic voltammograms obtained with Au, Au|MTMOS$_{gel}$, Au|MPS$_{gel}$ and Au|MPS|MTMOS$_{gel}$ electrodes immersed in (a) 0.001 mol dm^{-3} Fc(CH$_2$OH)$_2$ and (b) 0.001 mol dm^{-3} $Fe(CN)_6^{4-}$, solution in 0.1 mol·dm^{-3} KNO$_3$ aq. (scan rate 50 mV s^{-1}; surface area 0.02 cm^2.

The permeation ability of redox probe through the ITO|MTMOS$_{gel}$ electrode similarly to gold modified electrodes was verified in the Fc(CH$_2$OH)$_2$ aqueous solution (Fig.62).

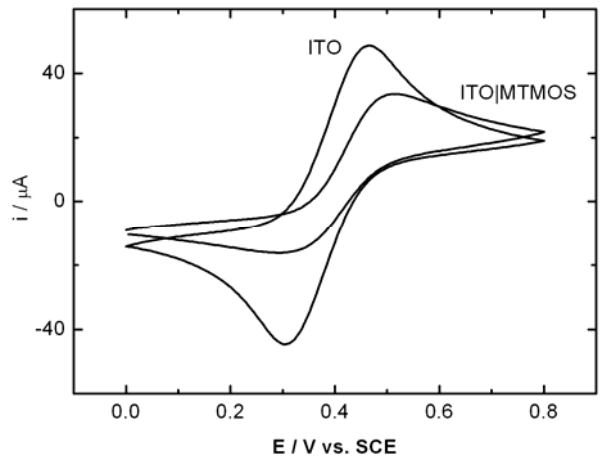

Fig.62. Cyclic voltammograms obtained with ITO and ITO|MTMOS$_{gel}$ electrodes immersed in 0.001 mol dm^{-3} Fc(CH$_2$OH)$_2$ aqueous solution in 0.1 mol dm^{-3} KNO$_3$. (scan rate 50 mV s^{-1}; surface area 0.36 cm^2).

For bare ITO electrode a reversible voltammetric response is observed with peak-to peak separation about 150 mV what can be in part attributed to ohmic resistance of ITO layer. The voltammogram of ITO|MTMOS$_{gel}$ electrode obtained in the same condition shows reduced current response. This is evidence that some part of the electrode surface is blocked by silicate film.

The above results show that apparently homogeneous MTMOS based film, as can be judged from AFM and FTIRRAS experiments, remains to some extent transparent for species dissolved in solution. This is clearly visible for the neutral redox probe with hydrophobic head and hydrophilic tails. Introduction of species having thiol groups much more block redox probe access to predominant part of the electrode surface. This effect occurs even if only its small part is intentionally blocked by chemisorbed MPS (Fig.47).

CV experiments with Fc(CH$_2$OH)$_2$ solution were also used to show surface development by Au deposition on silicate film surface. For this reason the voltammograms of the glass|MTMOS$_{gel}$|Au$_{ev}$ electrode with relatively high scan rate were done (Fig.63). The I$_p$ versus square root of scan rate were plotted (Fig.64) and compared with the glass|Au$_{ev}$ electrode and calculated values based Randles-Sevcik equation (eq.17). Deviation from the theoretical dependence can be easily seen for both electrodes. In the case of the glass|Au$_{ev}$ electrode slightly smaller current than calculated for geometric area is observed. It seems to that only part of the surface was coated by gold. Quite opposite effect is observed for glass|MTMOS$_{gel}$|Au$_{ev}$ electrode. The higher

value of peak current than theoretical, indicates more developed surface by the presence of $MTMOS_{gel.}$.

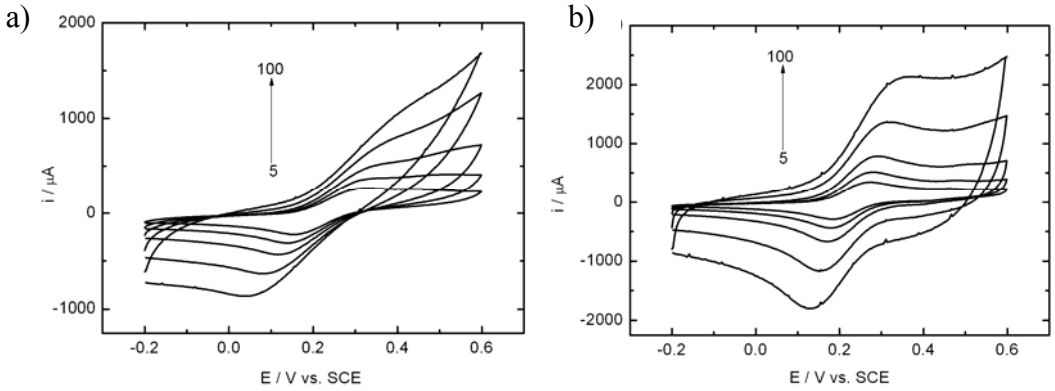

Fig.63. Cyclic voltammograms obtained with a) glass|Au_{ev} and b) glass|$MTMOS_{gel}$|Au_{ev} electrodes immersed in 0.001 mol dm^{-3} $Fc(CH_2OH)_2$ aqueous solution in 0.1 mol dm^{-3} KNO_3. (scan rate 5, 10, 20, 50 and 100 V s^{-1}; surface area 0.2 cm^2).

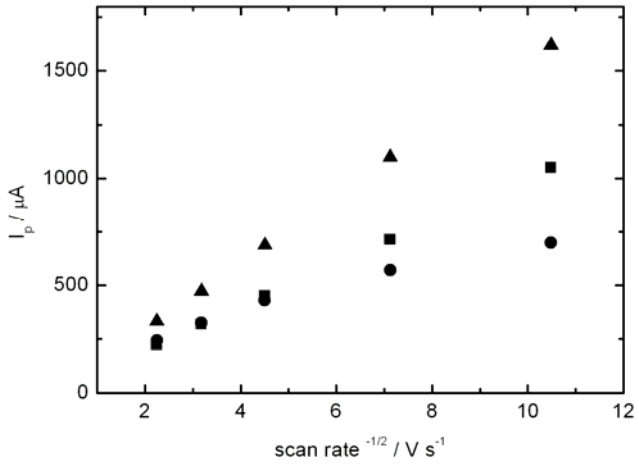

Fig.64. The dependences of cathodic peak current (I_p) versus square root of scan rate for calculated value (■), glass|Au(●) and glass|$MTMOS_{gel}$|Au_{ev} (▲) immersed in 0.001 mol dm^{-3} $Fc(CH_2OH)_2$ aqueous solution in 0.1 mol dm^{-3} KNO_3. (surface area 0.2 cm^2).

The water soluble derivative of ferrocene was also used to study the electrical and electrochemical properties of film containing CNFs. The ITO|CNF,SiO_2,$MTMOS_{gel}$ electrode voltammograms obtained during continuous scanning in the presence of $Fc(CH_2OH)_2$ in aqueous solution indicates the characteristics of a partially blocked electrode (Fig.65). At slower scan rate (1 mV s^{-1}) the sigmoidal shape of voltammograms is clearly seen (Fig.65) indicating ultramicroelectrode ensemble like behaviour [213]. This observation can be explained by assuming that the globular

structures visible in Fig.58A are effectively and partially insulating the electrode surface. They are highly hydrophobic and likely not wetted by the aqueous solution. The remaining electrode area probably acts as assembly of ultramicroelectrodes with mixed planar and spherical diffusion. The decrease of the current in comparison to unmodified ITO electrode (Fig.65) is also the evidence of substantial blocking the active ITO surface by the hydrophobic CNF-silica matrix. The existence of unwetted domains in electrode material was confirmed by 4 times increase of the voltammetric current with electrodes washed with 2-propanol before immersion into aqueous solution (Fig.66). This treatment might allows to remove gas bubbles from the hydrophobic mesoporous structure and enhanced access of the redox probe to the electroactive electrode surface.

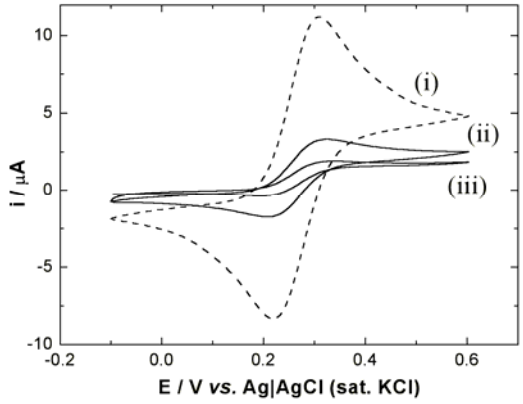

Fig.65. Cyclic voltammograms for the oxidation of 0.001 mol dm^{-3} $Fc(CH_2OH)_2$ in 0.1 mol dm^{-3} aqueous $NaClO_4$ (i) obtained at a bare ITO electrode at scan rate 10 mV s^{-1} (dashed curve) and (ii, iii) ITO|CNF,SiO_2,$MTMOS_{gel}$ electrodes at scan rate of (ii) 10 and (iii) 1 mV s^{-1} (solid lines); (surface area 0.2 cm^2).

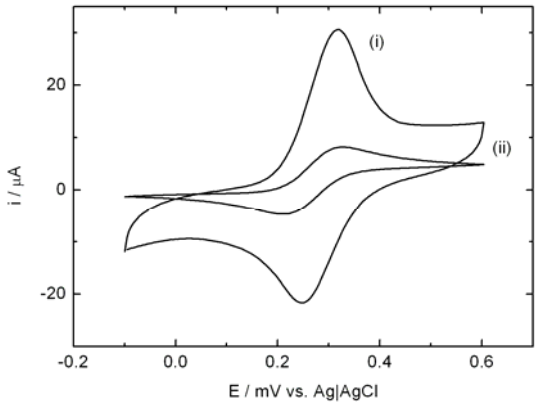

Fig.66. Cyclic voltammograms for the oxidation of 0.001 mol dm^{-3} $Fc(CH_2OH)_2$ in 0.1 mol dm^{-3} aqueous $NaClO_4$ obtained at ITO|CNF,SiO_2,$MTMOS_{gel}$ electrode (ii) dried and (i) washed with 2-propanol (surface area 0.02 cm^2; scan rate 10 mV s^{-1}.

The experiments with $Fc(CH_2OH)_2$ was also done for the electrode with ITO nanoparticles embedded in MTMOS gel. It indicates that presence of these nanoparticles slightly develope surface (Fig.67). Contrary to CNF's ITO nanopartciles do not exhibit ultramicroelectrde behaviour at slower scan rate. This reveals the expected increase in the capacitive back ground current as well as only a minor influence of the presence of ITO nanoparticles on the voltammetric peak current. This observation is consistent with an unblocked and highly reactive surface, good conductivity between particles and electron transfer occurring even at the outermost layers [214].

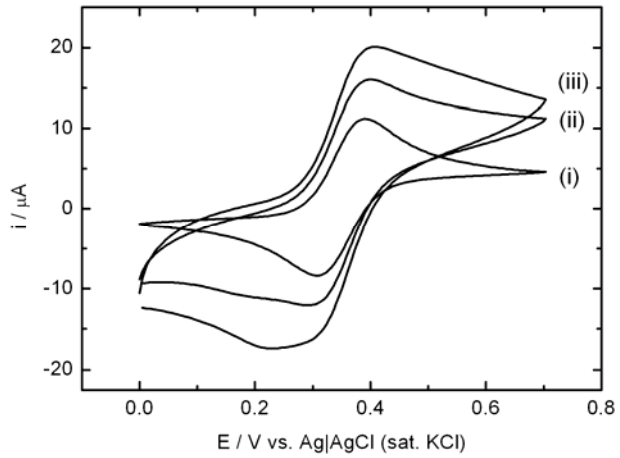

Fig.67. Cyclic voltammograms for the oxidation of 0.001 mol dm^{-3} $Fc(CH_2OH)_2$ in 0.1 mol dm^{-3} aqueous $NaClO_4$ obtained at ITO electrode (i), ITO\|ITO_{part},$MTMOS_{gel}$ electrode 6 layers (ii) and 12 layers (iii) (surface area 0.02 cm^2; scan rate 10 mV s^{-1}).

Summarising, the hydrophobic films obtained by sol-gel process are to some extent permeable for redox probe dissolved in aqueous electrolyte. This indicates that silicate films have developed structure and are rich of defects. The degree of the latter one strongly depends on the used precursors. Even though those merits, its presence partially blocks the electrode surface. Embedding of CNFs or ITO nanoparticles within the silicate matrix does not or only little improve the access of the redox probe to the electrically conductive substrate.

6.5. Electrochemical behaviour of redox liquids deposited on silicate films

As it was stated before (Chapter.2) in order to obtain good quality redox liquid modified electrode characterised by stable voltammetric response and high efficiency of the electrode process, the development of new electrode material is still required. Therefore the electrodes presented in previous chapter were modified with different types of redox liquids and their electrochemical properties were studied. For modification pure redox liquids *t*-butylferrocene [144] and *N,N*-didodecyl-*N',N'*-diethylphenylenediamine [134] were selected, because of the significant difference in their electrochemical behaviour due their different hydrophobicity. The latter compound was also diluted with organic acid in order to observe proton transfer across liquid-liquid interface [134]. Also supported diluted redox liquids: redox probe solution in room temperature ionic liquid or supported organic solvent were used. For comparison these deposits were also studied on unmodified electrode because of such system were not reported in literature.

6.5.1. tert-Butylferrocene

For most of the experiments *t*BuFc (Fig.68) was chosen for the reason that neutral molecule is practically insoluble in water, but its electrogenerated cation is partially soluble in aqueous media (10^{-3} – 10^{-4} mol dm^{-3}) [215,216]. These properties allow to monitor the transfer of the electrogenerated species to and from the aqueous solution and the matrix effect. In all cases *t*BuFc was deposited by its hexane solution and volatile solvent evaporation.

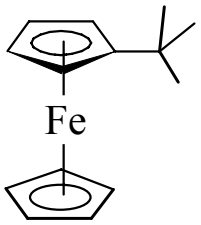

Fig.68. Molecular structure of tBuFc.

6.5.1.1. Au

It is already known that the electrochemical process of the pure redox liquid starts at three phase junction [133] (Chapter.2). To find the optimal length of the three phase junction the Au electrode with different amount of *t*BuFc deposit was studied by cyclic voltammetry in (Fig.69). The modified Au electrode was immersed into 0.1 mol dm^{-3} KNO_3 aqueous solution and the voltammograms were recorded. The fifth scan was arbitrary selected for analysis. Probably, during the first scan the reorganisation of the organic phase at the electrode surface may happen [133]. The microphases change the size after oxidation/reduction process and initially counterion insertion.

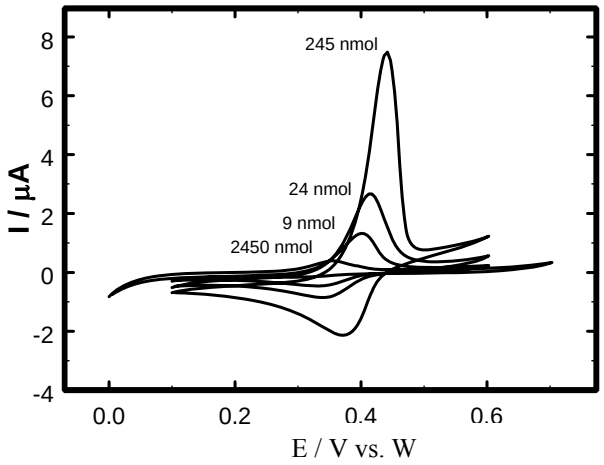

Fig.69. 5th scan cyclic voltammograms obtained with Au electrode modified with 9, 24, 245 and 2450 nmole of tBuFc immersed in 0.1 mole·dm^{-3} KNO_3 aqueous solution. (scan rate 50 mV s^{-1}; surface area 0.02 cm^2).

The electrooxidation/reduction process occurring at this electrode can be described as follows [217]:

$$tBuFc_{(org)} - \bar{e} \leftrightarrow tBuFc^{+}_{(org)} \qquad (26)$$

One can observe that there is no simple correlation between peak current and amount of *t*BuFc deposit. The larger amount of the redox liquid deposit results in I_p increase exept the largest one where the distinct drop of peak current is visible. This is probably because the electrode is overflooded by large amount of *t*BuFc. The efficiency of the electrode process is very small and equal 0.001%, 0.07%, 0.42%

and 0.53% for 2450 nmole, 245 nmole, 24 nmole and 9 nmole, respectively. These differences are connected with the length of the three phase junction, which probably depends on the dispersion of the redox liquid droplets on the electrode surface. Taking into account the value of I_p the 24 nmole deposit was chosen for further experiments.

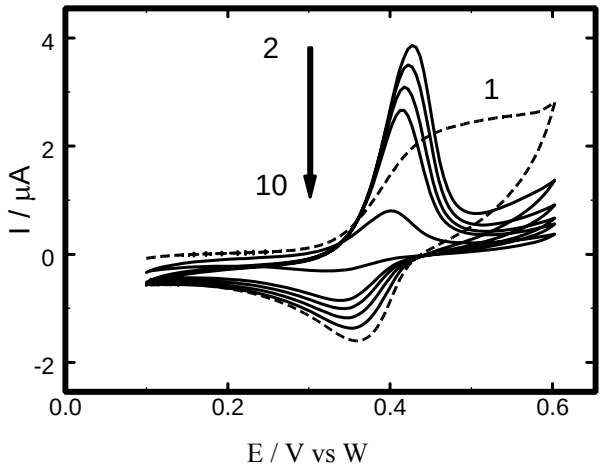

Fig.70. Cyclic voltammograms (1st, 2nd,3rd, 4th, 5th and 10th scan) obtained with Au electrode modified with 24 nmole of tBuFc immersed in 0.1 mol·dm^{-3} KNO_3 aqueous solution. Arrow marks the decrease of the current during subsequent scans. (scan rate 50 mV s^{-1}; surface area 0.02 cm^2).

During the subsequent scans (Fig.70) the decrease of the both peak currents is observed for this deposit. This is probably, because some of *t*BuFc$^+$ cations formed during electrode oxidation process, are ejected into the aqueous solution [144]:

$$t\text{BuFc}^+_{(org)} \rightarrow t\text{BuFc}^+_{(aq)} \qquad (27)$$

The value of the ratio of the anodic charge (Q_a) to cathodic charge (Q_c) (Q_a/Q_c) confirms the expulsion of the electrogenerated *t*BuFc$^+$ cations into the aqueous solution. It is larger than unity and it decreases from 1.5 (2nd scan) to the value 1.2 at the 10th scan. This indicates that the number of *t*BuFc$^+$ cations leaving the organic phase decreases during subsequent scans and it may be caused by change in the organic droplets composition due to some anion insertion (see below). One has to remember that Q_c contains also the contribution from re-deposition of the *t*BuFc due to electroreduction of the *t*BuFc$^+$ cations existing in the aqueous solution by the electrode surface:

$$t\text{BuFc}^{+}_{(aq)} + \bar{e} \rightarrow t\text{BuFc}_{(org)} \quad (28)$$

The Q_a/Q_c ratio is expected to be independent of the amount of the liquid phase, therefore its can be used as a measure of the competition between cation expulsion and any process resulting in tBuFc$^+$ confined to the electrode, like anion insertion or ion pair adsorption [144].

The shape of the first scan differs strongly from the second and further ones. CV curve is probably distorted by large ohmic drop caused by the very low concentration ions in the liquid deposit before experiment starts. The concentration of the ions within redox liquid may increase after first scan, because of some contribution of anion insertion in overall electrode process:

$$t\text{BuFc}^{+}_{(org)} + NO_3^-{}_{(aq)} \rightarrow t\text{BuFc}^{+}...NO_3^-{}_{(org)} \quad (29)$$

Alternatively, this behaviour can be accounted for rearrangement of deposit to the number of smaller redox liquid droplets during the first scan.

6.5.1.2. Au|MTMOS$_{gel}$

The shape of cyclic voltammograms obtained with Au|MTMOS$_{gel}$ electrode modified with tBuFc (Fig.71) is somewhat different than that of bare Au modified with droplets of this compound (Fig.70). The peaks current are not so well developed and less sharp as in the case of unmodified gold electrode. Moreover, the distance between anodic and cathodic peak becomes bigger by about 20 mV when MTMOS film is present at the electrode surface.

Also the smaller I_p and the negative shift of E_a by 20-40 mV represent another difference. It seems that the presence of the MTMOS thin film moderately facilitate the oxidation of the tBuFc molecules. The decrease of the peak current may indicate, that diffusion of the reaction substrate through pores is substantially slower than in solution and/or the surface of the modified electrode is partially blocked by sparingly porous parts of silicate matrix. This decreases access of redox liquid to the gold surface and reduces formation of Au|tBuFc|aqueous solution three phase junction. It can be considered as the drawback of this type of modification. It results in about ten

times decrease of efficiency of the electrode process equal about 0.03% for the 2nd scan.

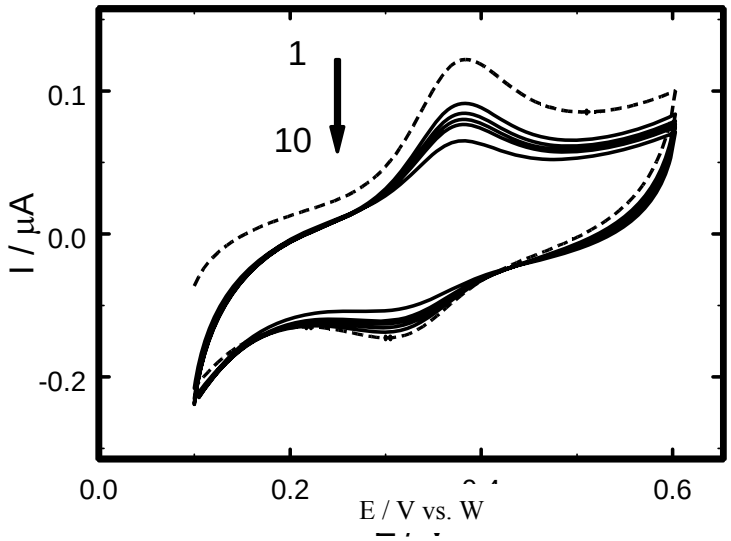

Fig.71. Cyclic voltammograms (1st, 2nd,3rd, 4th, 5th and 10th scan) obtained with Au|MTMOS electrode modified with 24 nmole of tBuFc immersed in 0.1 mol·dm^{-3} KNO_3 aqueous solution. Arrow marks the decrease of the current during subsequent scans. (scan rate 50 mV s^{-1}; surface area 0.02 cm^2).

Still the current decrease during subsequent scans is observed (Fig.71). However, the magnitude of this effect is smaller than for bare Au electrode. The magnitude of the anodic peak current (I_a) obtained in 10th scan at $TMOS_{gel}$ modified electrode is roughly one third of that obtained during first scan (Fig.71). This indicates larger contribution of eq.28, thus smaller expulsion of electrogenerated cations (eq.27) and therefore better stability of the electrode|redox liquid|aqueous solution system. This is also confirmed by smaller value of Q_a/Q_c ratio in comparison to Au|*t*BuFc electrode. It changes from 1.4 to 1.15 from 1st to 10th scan (Fig.72). Obviously, the presence of the silicate film slows down expulsion from and stabilises *t*BuFc$^+$ cation within the hydrophobic matrix. This can be explained by the attractive interactions between free electron pair of oxygen atoms connecting silicone atoms of silicate network and electrogenerated cation.

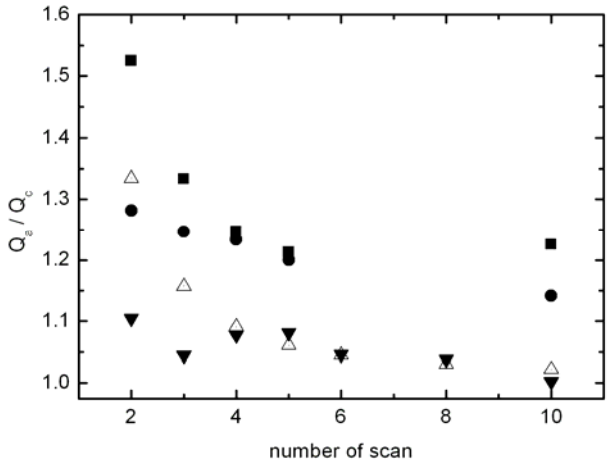

Fig.72. The dependence of Q_a/Q_c ratio versus number of scans for Au (■), Au|MTMOS$_{gel}$ (●), Au|MPS$_{gel}$ (▼) and Au|MPS|MTMOS$_{gel}$ (Δ) electrodes modified with 24 nmole of tBuFc and immersed in 0.1 mol dm $^{-3}$ KNO_3 aqueous solution (scan rate 50 mV s^{-1}; surface area 0.02 cm^2).

6.5.1.3. Au|MPS|MTMOS$_{gel}$

The premodification of hydrophobic silicate modified Au electrode with MPS layer more significantly changes its electrochemical behaviour after deposition of *t*BuFc. The decrease of the current magnitude by half is observed only during the first five scans. This effect is smaller than for Au or Au|MTMOS$_{gel}$ electrodes (Fig.73). Further scanning does not affect the shape of voltammogram. Contrary to the Au and Au|MTMOS$_{gel}$ electrodes Q_a/Q_c is close to unity after small decrease from less than 1.15 during the 1st scan (Fig.72). One may conclude that hydrophobic methyl as well as some not chemisorbed electrodonating mercapto groups stabilise the electrogenerated *t*BuFc$^+$ cations within the matrix preventing its expulsion to aqueous phase. Better anchoring of hydrophobic silicate matrix than in the case of Au|MTMOS$_{gel}$ electrode may also contribute to better immobilisation of electrogenerated ions (eq.29). Contrary to the Au and Au|MTMOS$_{gel}$ electrodes the largest decrease of the anodic peak current, roughly about 80% of the effect is observed for 2nd scan. This may be connected with partial expulsion of *t*BuFc$^+$ cations from *t*BuFc droplets not fixed within silicate film being in direct contact with Au support.

Similarly to Au|MTMOS$_{gel}$ electrode smaller currents in comparison to bare Au and the same level of the efficiency (0.03%) are obtained. This indicates that the surface is partially blocked. Interestingly, no specific difference between shape of the

voltammogram obtained during 1st and further scans is observed for both types of silicate modified electrodes. This may indicate that no important change in distribution of microdroplets within silicate film occurs after first portion of counterions enters organic phase.

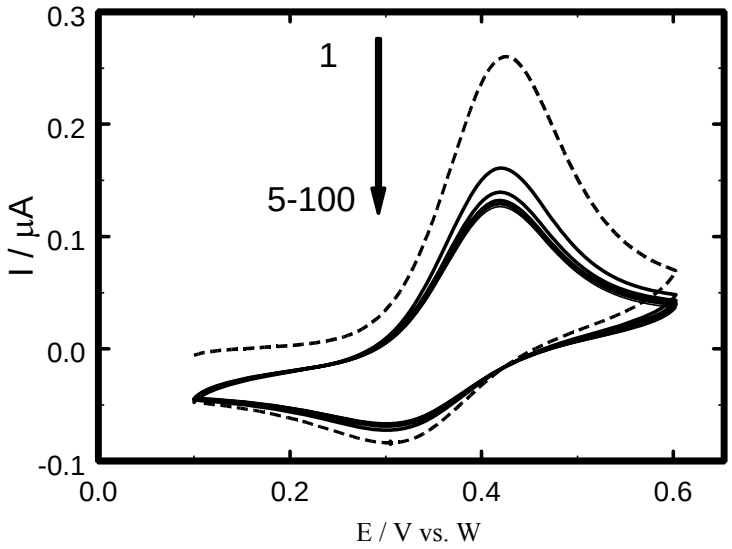

Fig.73. Cyclic voltammograms (1st, 2nd,3rd, 4th, 5th and 100th scan) obtained with Au|MPS|MTMOS$_{gel}$ electrode modified with 24 nmole tBuFc immersed in 0.1 mol·dm^{-3} KNO_3 aqueous solution. Arrow marks the decrease of the current during subsequent scans. (scan rate 50 mV s^{-1}; surface area 0.02cm^2).

For this electrode due to the stability of the voltametric response the effect of scan rate was studied. Approximately linear dependence between peak current and square root of scan rate is observed. This is clear evidence that diffusion of the redox probe is important part of the electrochemical process.

Next, CA measurements of stable electrode Au|MPS|MTMOS$_{gel}$ were done to get more information about the mode of the redox active molecule to the electrode surface. These experiments (Fig.74a,b) were done for fresh and cycled samples. In the latter case potential step experiments were applied after stable voltammogram was obtained. More information was obtained from the so called Cottrell plot: current vs. square root of time (Fig.74c,d). The positive intercept on anodic part of the plot obtained from the data acquired at longer times (Fig.74c) is a feature of ultramicroelectrode [218] or ultramicroelectrode assembly like behaviour [219,220] indicating that the electrode reaction site is restricted to close neighbourhood of the three phase junction Au|redox liquid|aqueous electrolyte. The deviation from this

dependence at shorter times of electrolysis, more pronounced for non cycled sample, may result from electrodissolution of smaller droplets of redox liquid. For electroreduction the picture is more complicated. For fresh sample the linear Cottrell plot with zero intercept, typical for nonspherical diffusion [79] indicates that larger part of the electrode surface is involved possibly larger contribution of re-deposition of *t*BuFc due to electroreduction of $t\text{BuFc}^{+}_{(aq)}$ species (eq.28).

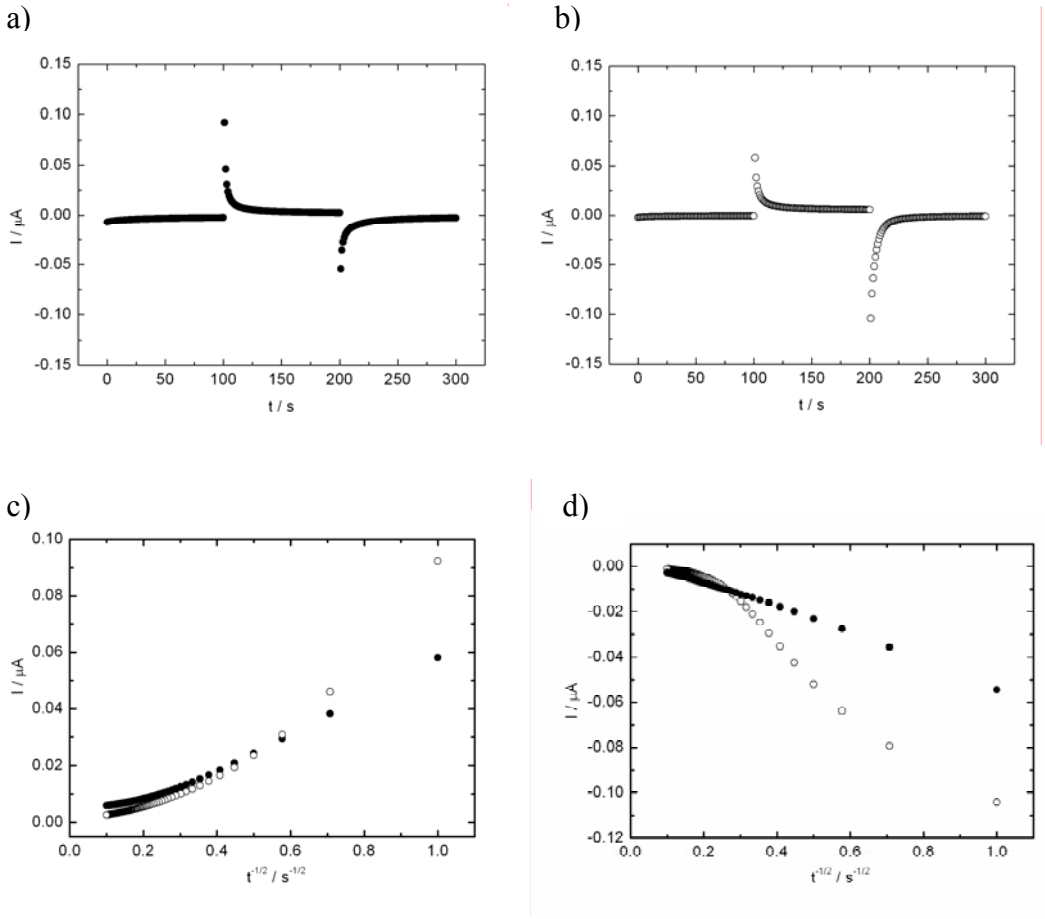

Fig.74. The current (I) vs. time (t) dependence (a fresh, b after five CV cycles) obtained from potential step experiments obtained with Au|MTMOS|MPS$_{gel}$ electrode (surface area 0.02 cm^2) modified with 24 nmole tBuFc immersed in 0.1 mol·dm^{-3} KNO_3 aqueous solution. The Cottrell plots obtained from anodic (b) and cathodic (c) step of the experiment described above for fresh (●) and after five CV cycles (○) electrode.

6.5.1.4. Au|MPS$_{gel}$

The electrochemical behaviour of Au|MPS$_{gel}$ electrode modified with *t*BuFc (Fig.75) is different than that of Au and Au|MTMOS$_{gel}$ but similar to Au|MPS|MTMOS$_{gel}$. After first five scans the stable voltammetric response is

observed. During the next subsequent scans the shape of the voltammograms is not much affected by the time of experiment. One can easily judge, that using MPS for thin film preparation or to anchor $MTMOS_{gel}$ prevents the redox probe expulsion into the aqueous solution. It is probably because of enrichment of thin film surface in numerous protrusions and possible coordination of electrogenerated tBuFc$^+$ to thiol groups. Similarly to Au|MPS|$MTMOS_{gel}$ electrode Q_a/Q_c is stable and close to unity. The efficiency of electrode process for Au|MPS_{gel} electrode is much higher than for Au, Au|$MTMOS_{gel}$ or Au|MPS|$MTMOS_{gel}$ and its value is close to 1%.

Contrary to Au|MPS|$MTMOS_{gel}$ electrode, the linear dependence between peak current and scan rate, was found from the voltammograms obtained for Au|MPS_{gel} electrode. This is typical for adsorptive or restricted diffusion process. The different electrochemical behaviour of Au|MPS_{gel} and Au|MPS|$MTMOS_{gel}$ electrode modified with the redox liquid probably results from different surface topography. Probably the redox liquid is more dispersed and the length of three phase junction is significantly increased.

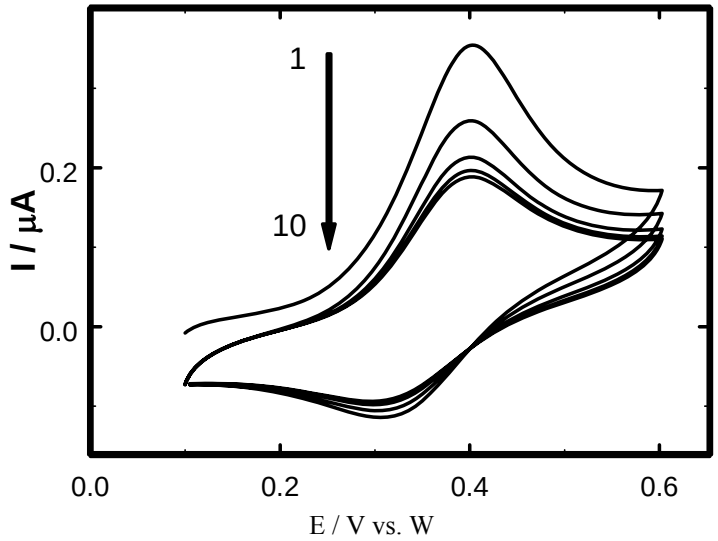

Fig.75. Cyclic voltammograms (1st, 2nd,3rd, 4th, 5th and 10th scan) obtained with Au|MPS_{gel} electrode (surface area 0.02 cm^2) modified with 24 nmole of tBuFc immersed in 0.1 mol·dm^{-3} KNO_3 aqueous solution. Arrow marks the decrease of the current during subsequent scans. Scan rate 50 mV s^{-1}

6.5.1.5. glass|Au_{ev}

The voltammetric response of glass|Au_{ev} modified with tBuFc is presented in Fig.76. The first scan differs from next as observed for bare gold electrode and

described in chapter 6.5.1.1. During the subsequent scans the shape of the voltammograms is not much affected by the time of experiment what distinguish this type of electrode from gold disc one. The observed stabilisation of voltammetric response can be caused by the porous structure of gold layer and roughness of glass support. Also the efficiency of this electrode process (2%) is almost one order of magnitude higher compare to the gold disc one and may also result from the more heterogeneous electrode surface.

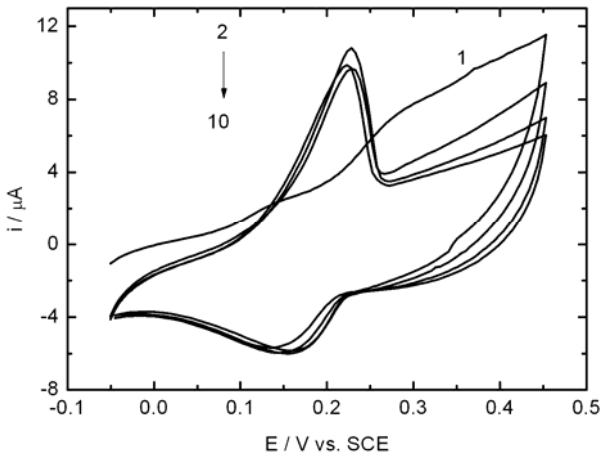

Fig.76. Cyclic voltammograms for the oxidation of 24 nmole immobilised tBuFc on glass|Au_{ev} electrode immersed into aqueous solution of 0.1 mol·dm^{-3} KNO_3. Scan rate 50 mV s^{-1}; surface area 1 cm^2.

6.5.1.6. glass|$MTMOS_{gel}$|Au_{ev}

Similarly to Au|$MTMOS_{gel}$ the glass|$MTMOS_{gel}$|Au_{ev} electrode modified with *t*BuFc exhibits decrease of I_p during the subsequence scans. One can easily judge, that expulsion of the *t*BuFc cation into aqueous solution is dominating process at this electrode and can be described by the eq.27. Additionally two effects are observed on the Fig.77. First, the significantly different shape of the first scan. As it was mentioned in Chapter.6.5.1.1., this effect can be caused by the droplets rearrangement. Next, the significant shift of the E_a is observed. This can result also from droplets reorganisation and new microphases formation.

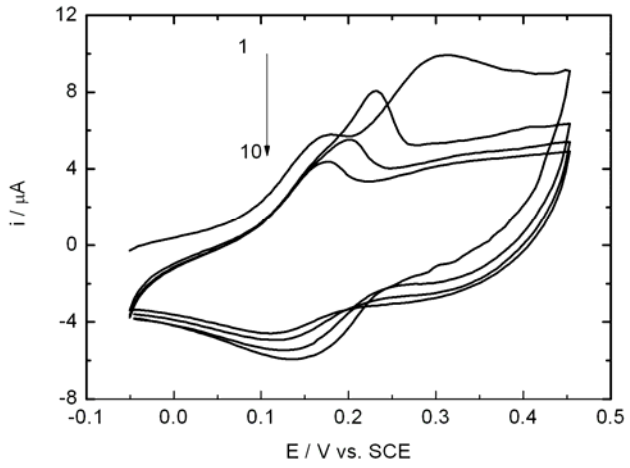

Fig.77. Cyclic voltammograms for the oxidation of 24 nmole immobilised tBuFc on glass|$MTMOS_{gel}$|Au_{ev} electrode immersed into aqueous solution of 0.1 mol·dm^{-3} KNO_3. Scan rate 50 mV s^{-1}; surface area 1 cm^2.

The efficiency of glass|$MTMOS_{gel}$|Au_{ev} electrode process is similar to glass|Au_{ev} one and is equal 2%. Surprisingly no stabilisation of voltammetric response was observed for this electrode. This effect differs glass|$MTMOS_{gel}$|Au_{ev} electrode from glass|Au_{ev} as well as Au|$MTMOS_{gel}$ one.

6.5.1.7. ITO electrode

Similarly as it was done for Au electrode, bare ITO one was modified with *t*BuFc. The voltammetric response is presented in Fig.78. The efficiency of the oxidation process (eq.26) is equal 0.2% - similar to Au|tBuFc electrode. This indicates that most of the redox liquid remains unreacted because of short length of three phase junction at the electrode surface. The decrease of the current magnitude is observed. However the stabilisation of the electrochemical response occurs after 10th scan. This is in contrast to unstable electrochemical behaviour on bare Au modified with *t*BuFc where no stabilisation in time was observed. This effect may occur for the reason of roughness and oxide nature of ITO support.

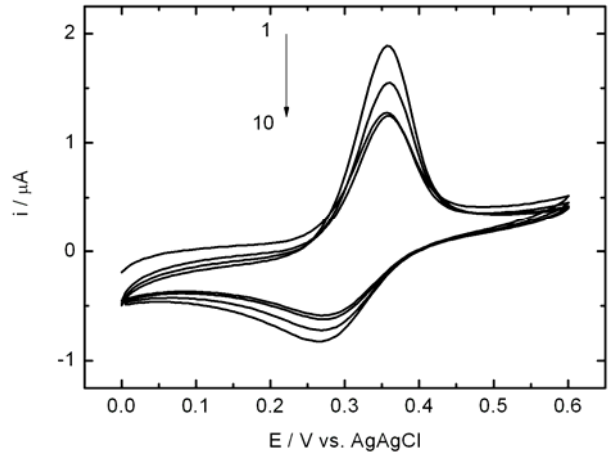

Fig.78. Cyclic voltammograms for the oxidation of 20 nmole immobilised tBuFc immersed into aqueous solution of 0.1 mol·dm^{-3} KNO_3 on a bare ITO electrode. Scan rate 50 mV s^{-1}; surface area 0.36 cm^2.

6.5.1.8 . ITO|MTMOS$_{gel}$

Next, ITO|MTMOS$_{gel}$ electrode modified with *t*BuFc was investigated. Its electrochemical behaviour is similar to that of redox liquid modified ITO electrode namely stabilising effect of voltammetric response is observed (Fig.79). But in the latter case the presence of thin hydrophobic silicate film enhances this behaviour. The efficiency of the electrode process remain on the same level and results about 0.1% and is one order of magnitude larger than for Au|MTMOS$_{gel}$ electrode indicating different structure of the deposit.

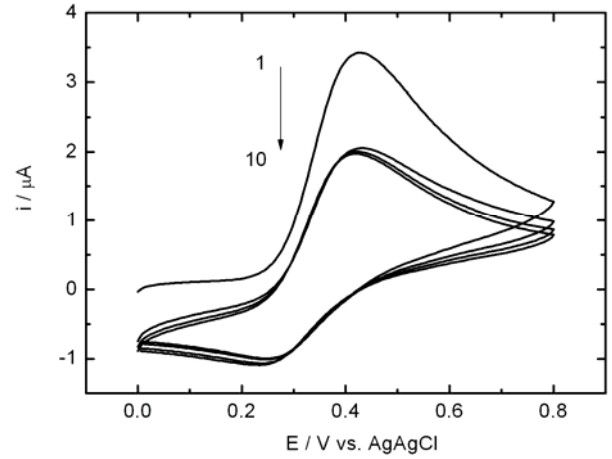

Fig.79. Cyclic voltammograms for the oxidation of 20 nmole immobilised tBuFc immersed into aqueous solution of 0.1 mol·dm^{-3} KNO_3 on an ITO|MTMOS$_{gel}$. Scan rate 50 mV s^{-1}; surface area 0.36 cm^2.

6.5.1.9. ITO|ITO$_{part}$|MTMOS$_{gel}$

The voltammetric response of ITO electrode with layer-by-layer deposited ITO nanoparticles embedded in MTMOS$_{gel}$ thin film, further modified with *t*BuFc deposit and immersed into aqueous solution are presented in Fig.80. One can conclude that together with increasing number of ITO nanoparticle layers the peak current connected with redox liquid electrochemical process also increases. Comparing to the ITO|MTMOS$_{gel}$ electrode the I_p is 15, 40, 90, 460 times bigger and the efficiency of the electrode reaction increases from 0.9, 2.2, 3.7 to 30.0%, for the electrodes with 3, 6, 9, 12 ITO nanoparticles layers respectively. This clearly indicates that introduction of the nanopartcles considerably enhances the efficiency of the electrode process. Therefore the electrode modified with 12 layers of nanoparticles was chosen for the experiments with different amounts of redox liquid (Fig.81).

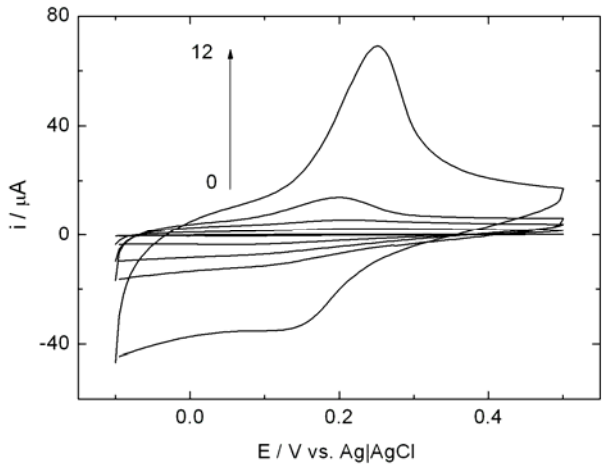

Fig.80. Cyclic voltammograms obtained with bare ITO and modified with ITO|ITO$_{part}$|MTMOS$_{gel}$ (0, 3, 6, 9, 12 nanoparticles layers) electrodes with deposited 24 nmole of tBuFc 0.1 mol·dm^{-3} NaClO$_4$ aqueous solution. Scan rate 50 mV s^{-1}; surface area ca. 1 cm^2.

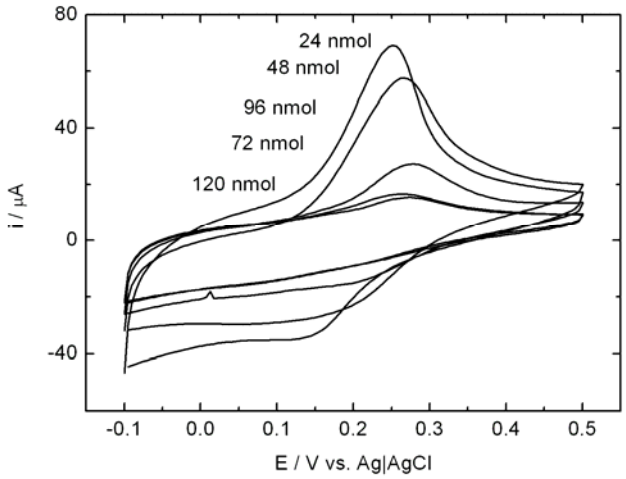

Fig.81. 2nd scan cyclic voltammograms obtained with ITO|ITO_{part}|$MTMOS_{gel}$ (12 nanoparticles layers) electrode modified with 24, 48, 72, 96 and 120 nmole of tBuFc immersed in 0.1 mol·dm^{-3} $NaClO_4$ aqueous solution. (scan rate 50 mV s^{-1};surface area ca. 1 cm^2).

The largest peak current magnitude was obtained for the electrode modified with 24 nmole of *t*BuFc. This data indicate that at this electrode the longest three phase junction is formed. The next experiment with this amount of *t*BuFc exhibits the change of voltammetric response of the redox liquid deposited on ITO|ITO_{part}|$MTMOS_{gel}$ (Fig.82) during subsequent scanning. Clearly the decrease of I_p is observed. Also the ratio of Q_a/Q_c charge decreases from 1.2 for the 2nd to nearly 1.0 for 10th scan. The peak current decrease because instead of the counter ions insertion same expulsion of *t*BuFc occurs. This electrode is not stable. On the other hand the efficiency of the electrode process is equal 30% for the 2nd scan and two order of magnitude bigger than for clean ITO or ITO|$MTMOS_{gel}$ electrodes.

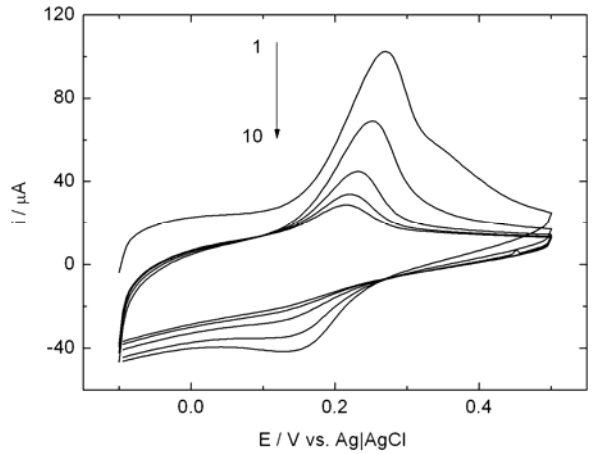

Fig.82. Cyclic voltammograms obtained with ITO modified with ITO 12 layers of ITO nanoparticles electrode with deposited 24 nmol of tBuFc 0.1 mol·dm^{-3} $NaClO_4$ aqueous solution. Scan rate 50 mV s^{-1}; surface area ca. 1 cm^2.

Summarising, the deposition of ITO nanoparticles embedded in hydrophobic matrix allows for large extension of the length of three phase junction.

6.5.1.10. ITO|CNF,SiO_2,$MTMOS_{gel}$

Next, the hydrophobic ITO|CNF,SiO_2,$MTMOS_{gel}$ electrodes were modified with 1960, 196, 19.6 and 7.2 nmole of *t*BuFc (Fig.83). After immersion into the aqueous solution the electrooxidation of the redox probe occurs at the resulting electrodes during voltammetric experiment.

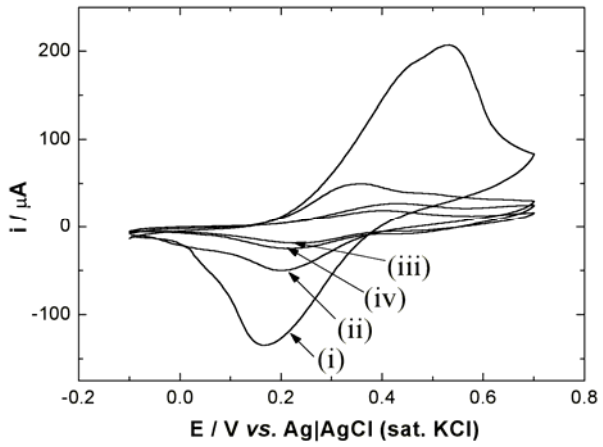

Fig.83. Cyclic voltammograms (3rd scan, scan rate 10 mV s^{-1}) obtained for the oxidation of tBuFc immobilised in a hydrophobic CNF – silica film modified ITO electrode (surface area 0.2 cm^2) immersed in aqueous 0.1 mol dm^{-3} $NaClO_4$ with (i) 1960, (ii) 196, (iii) 19.6, and (iv) 7.2 nmole of tBuFc.

Two important effects can be seen from these voltammograms. First, the hydrophobic CNFs embedded in silica thin film are electrochemically active and electrically connected to the ITO substrate. Second, for a larger amount of the redox liquid deposit a larger electric charge passes during a single scan. However, this dependence is not linear and higher efficiency of the electrode process is observed at lower amount of tBuFc deposit. Probably, in the presence of larger deposit the electrode is overflooded by the large amount of redox liquid. This behaviour is probably connected with the increase of length of three phase junctions at carbon nanofibrer | *t*BuFc | aqueous electrolyte interface which is expected to be more extended for a smaller amount of deposit. The efficiency of electrode process (calculated for 3rd scan) increases going from the larger to the smaller amount of deposit being equal 2, 5, 12, and 32% for 1960, 196, 19.6, and 7.2 nmole *t*BuFc deposit, respectively. However, the ratio Q_a/Q_c decreases from larger to smaller deposit being equal 2.4, 1.4, 1.3, and 1.5. It looks like in the case of smaller deposit an anion transfer process is much more favourable than *t*BuFc$^+$ expulsion into the aqueous phase. This conclusion is supported by observation that for the two largest deposits the voltammograms are unstable during subsequent potential cycles and a peak current decrease is observed. Therefore for next experiments with this electrode 19.6 nmole was selected.

The stable cyclic voltammograms for the oxidation of 19.6 nmole tBuFc immobilised on ITO|CNF,SiO_2,$MTMOS_{gel}$ obtained at various scan rates are presented in Fig.84. At slower scan rates a well-defined peak shaped response with only slightly increased peak-to-peak separation is observed. Both anodic and cathodic peak becomes spread at faster scan rates. This shape of voltammetric curves probably results from substantial surface area of the carbon nanofibres and resistance in the electrical contact between CNFs and ITO substrate.

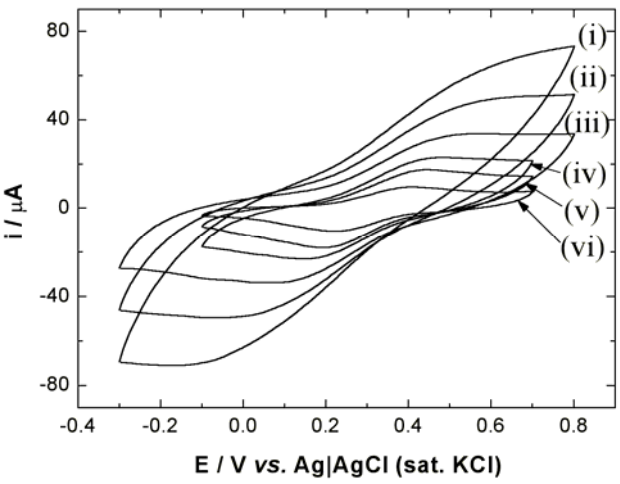

Fig.84. Cyclic voltammograms (scan rate (i) 160, (ii) 80, (iii) 40, (iv) 20, (v) 10, and (vi) 5 mV s^{-1}) obtained for the oxidation of 19.6 nmole tBuFc immobilised on ITO|CNF,SiO_2,$MTMOS_{gel}$ (surface area 0.2 cm^2) immersed in aqueous 0.1 mol dm^{-3} $NaClO_4$.

The comparison of voltammograms obtained for the oxidation of the same amount of *t*BuFc immobilised on the electrode with CNFs present and absent in the silicate matrix is shown in Fig.85.

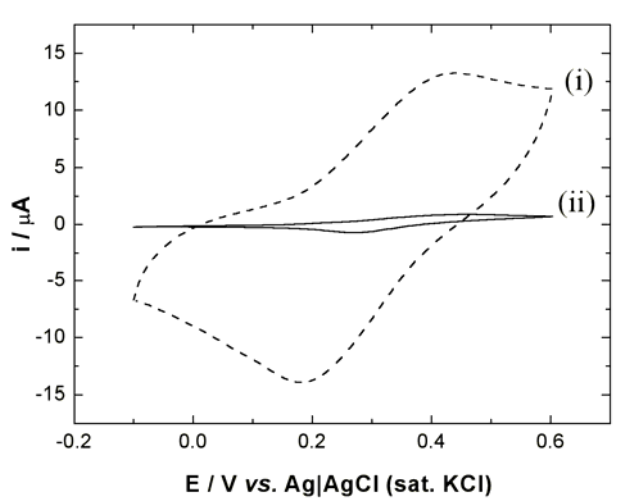

Fig.85. Cyclic voltammograms (scan rate 10 mV s^{-1}) obtained for the oxidation of 19.6 nmole tBuFc immobilised (i) on ITO|CNF,SiO_2,$MTMOS_{gel}$ and (ii) ITO|SiO_2,$MTMOS_{gel}$ (surface area 0.2 cm^2) and immersed in aqueous 0.1 mol dm^{-3} $NaClO_4$.

In the presence of CNFs the voltammetric signal is very stable in subsequent scans. On the other hand considerable decrease of both peak currents is observed on

voltammetric signal for ITO|SiO_2,$MTMOS_{gel}$ electrode (Fig.86). It obviously reveal stabilising properties of CNFs. Probably, such a film creates a more extended hydrophobic interface with sufficient electrical conductivity to enhances stable voltammetric responses. This is confirmed by the fact that I_p is one order of magnitude bigger when CNFs are embedded in silicate matrix. The huge increase of CNFs developed surface area also contributes to high efficiency of the electrode process. For the 2nd scan its value is about 30% for ITO|CNF,SiO_2,$MTMOS_{gel}$ and only 0.5% for ITO|SiO_2,$MTMOS_{gel}$. Therefore one can conclude that CNFs immobilisation creates a much more extended three phase junction: electrode | tBuFc | aqueous electrolyte. The absence of CNFs causes decrease of I_p (Fig.86) and an anion insertion into the organic phase (eq.29) is less favourable than the expulsion of $tBuFc^+$ into the aqueous solution (eq.27).

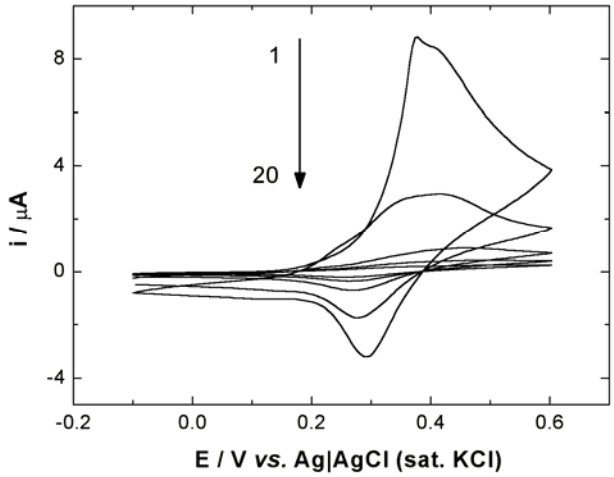

Fig.86. Cyclic voltammograms (1st, 2nd, 3rd, 4th, and 20th scan, scan rate 0.01V s^{-1}) obtained for the oxidation of 19.6 nmole tBuFc immobilised on ITO|SiO_2,$MTMOS_{gel}$ (surface area 0.2 cm^2) and immersed in aqueous 0.1 mol dm^{-3} $NaClO_4$.

Summarising, the electrochemical properties of *t*BuFc modified electrode depend on the content of the matrix. The stable voltammetric response is obtained only in the presence of CNFs together with significant enhancement of the efficiency of the electrode process.

Summary

In this chapter novel substrates for electrodes modified with redox liquid were tested. After deposition of redox probe *t*BuFc as a organic phase its electrochemical process was investigated. In general two processes maintain the neutrality of the organic phase. The expulsion of *t*BuFc cation into the aqueous solution (eq.27) and the counterion insertion into the organic phase (eq.29) or both of them can take place. Apart of the hydrophobic/hydrophilic properties of redox probe and counterion interaction of electrogenerated cation with silicate film affects the mechanism of the electrode process. The dominant electrode reaction mechanism for all studied electrodes is shown in Fig.87 and Fig.88.

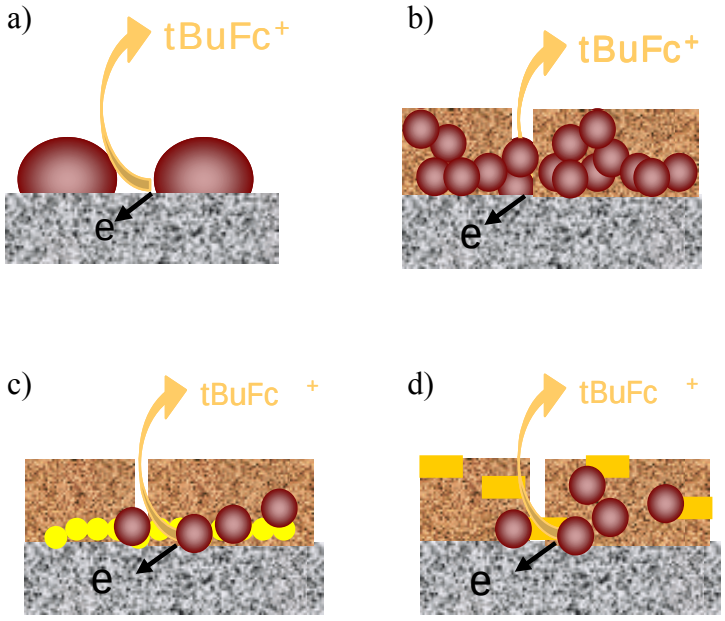

Fig.87. Dominant electrode reaction mechanism on a) Au, ITO, b) Au|MTMOS$_{gel}$, ITO|MTMOS$_{gel}$, c) ITO|ITO$_{part}$|MTMOS$_{gel}$ and d) glass|MTMOS$_{gel}$|Au$_{ev}$ modified with tBuFc.

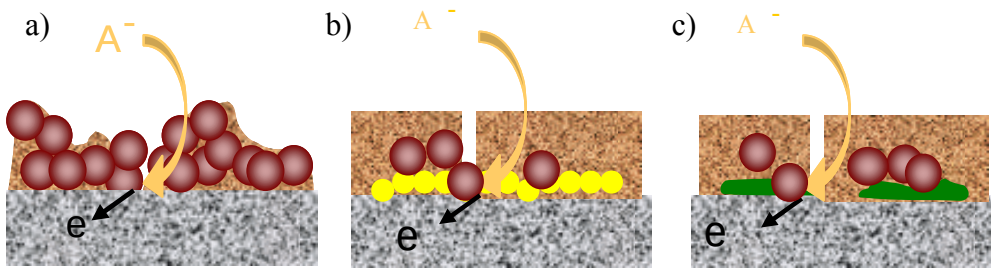

Fig.88. Dominant electrode reaction mechanism on a) Au|MPS$_{gel}$, b) Au|MPS|MTMOS$_{gel}$, c) ITO|CNF,SiO$_2$,MTMOS$_{gel}$ modified with tBuFc.

The comparison of some of their electrochemical properties is presented in the Table 3.

Table 3. The comparison of the electrode process efficiency and electrodes stability for all tBuFc modified electrodes.

Electrode	**scan efficiency (2^{nd} scan) / %**	**Stability**
Au	0.4	no
Au|$MTMOS_{gel}$	0.03	after 10^{th} scan
Au|MPS|$MTMOS_{gel}$	0.03	after 5^{th} scan
Au|MPS_{gel}	1.0	after 5^{th} scan
ITO	0.2	after 10^{th} scan
ITO|$MTMOS_{gel}$	0.1	after 5^{th} scan
glass|Au_{ev}	2.0	after 10^{th} scan
glass|$MTMOS_{gel}$|Au_{ev}	2.0	no
ITO|ITO_{part}|$MTMO_{Sgel}$		
3 layers of ITO_{part}	1.0	no
6 layers of ITO_{part}	2.2	no
9 layers of ITO_{part}	3.7	no
12 layers of ITO_{part}	30.0	no
ITO|CNF,SiO_2,$MTMOS_{gel}$	30.0	after 2^{nd} scan
ITO|SiO_2,$MTMOS_{gel}$	0.5	no

Summarising the presence of the thin silicate film at the electrode surface stabilises voltammetric response in most cases except glass|$MTMOS_{gel}$|Au_{ev} and ITO|ITO_{part}|$MTMO_{Sgel}$ electrodes. However its presence causes the decrease of the efficiency of the electrode process. On the other hand, embedded conductive nanoobjects like ITO nanoparticles or CNFs considerably increase the efficiency of this parameter. Moreover addition of CNFs into the silicate film stabilise voltammetric response.

6.5.2. Neat and diluted *N,N*-didodecyl-*N',N'*-diethylphenylenediamine

For next experiments the *N,N*-didodecyl-*N',N'*-diethylphenylenediamine (DDPD) (Fig.89) was chosen for the reason that neutral and first oxidised form are water insoluble molecules [133] contrary to *t*BuFc redox probe. Therefore electrochemical behaviour of DDPD modified electrodes is expected to be stable. Earlier in this thesis it was used for optimalisation of silicate layer (Chapter 6.1).

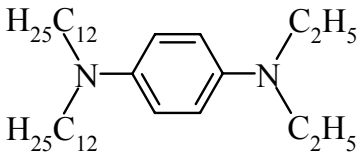

Fig.89. Molecular structure of DDPD.

During the electrooxidation process (in the limited range of potential window) to maintain the neutrality the transfer of the counterion from the aqueous solution into the organic phase occurs [133]. This reaction consists of heterogeneous electron transfer:

$$DDPD_{(org)} - e \leftrightarrow DDPD_{(org)}^{+} \quad (30)$$

and ion transfer from aqueous solution into the organic phase [133]:

$$DDPD_{(org)}^{+} + ClO_4^-{}_{(aq)} \leftrightarrow DDPD^{+}\ldots.ClO_4^-{}_{(org)} \quad (31)$$

The voltammograms obtained with different amount of DDPD deposited on Au|$MTMOS_{gel}$ electrode are presented in Fig.90. The best defined response with small peak-to-peak separation was obtained for 1.9 nmole of this diamine, that is why this concentration was selected for further experiments.

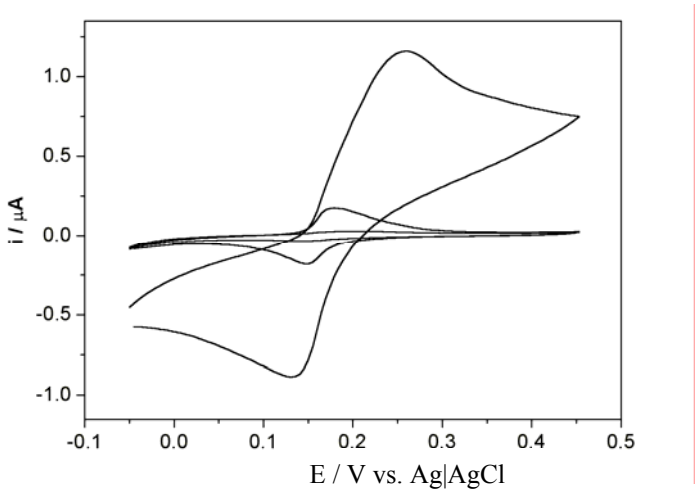

Fig.90. 2nd scan cyclic voltammograms obtained with Au|MTMOS$_{gel}$ electrodes modified with 0.2, 1.9 or 19 nmole DDPD immersed in aqueous 0.1 mol dm^{-3} $KClO_4$ aqueous solution. Scan rate 10 mV s^{-1}; surface area 0.02 cm^2.

Changing the scan rate for Au|MTMOS$_{gel}$ electrode modified with DDPD shows an approximately linear increase of peak current. This indicates adsorptive character of the electrode process. Unfortunately, unstable voltammetric response for this electrode with *t*BuFc deposit prevented doing this type of experiment and comparision of the data. However, approximately linear dependence between peak current and square root of scan rate was exhibited for Au|MPS|MTMOS$_{gel}$ electrode modified with *t*BuFc droplets. Obviously using different redox probes changes the character of electrochemical reaction. The process controlled by diffusion for Au|MPS|MTMOS$_{gel}$ modified with *t*BuFc changes to adsorptive for the same deposit on Au|MPS$_{gel}$ and with DDPD deposited on Au|MTMOS$_{gel}$ (Fig.91). Probably this effect is connected with the volume of microphases presented at the electrode surface. It seems to that adsorptive character appears when smaller microphases are formed.

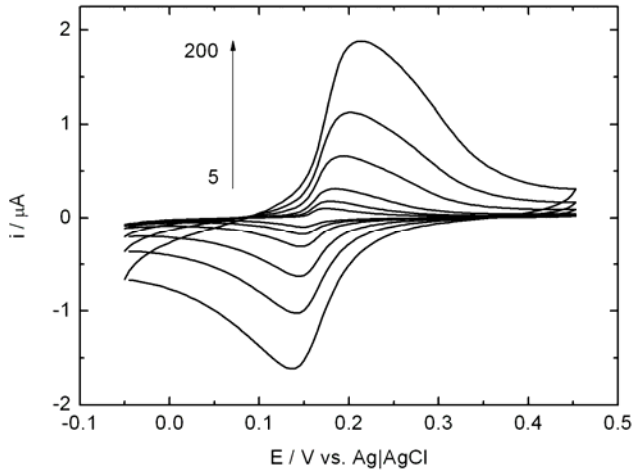

Fig.91. 2nd scan cyclic voltammograms obtained with Au|MTMOS$_{gel}$ electrodes (surface area 0.02 cm^2) modified with 1.9 nmole DDPD solution in hexane and immersed in aqueous 0.1 mol dm^{-3} KClO$_4$ aqueous solution. Scan rate 5, 10, 20, 50, 100 and 200 mV s^{-1}; surface area 0.02 cm^2.

Next, the electrochemical behaviour of DDPD deposit undiluted and diluted with hydrophobic di-(2ethyl-hexyl)phosphate (HDOP) on bare Au and Au|MTMOS$_{gel}$ electrodes was compared (Fig.92).

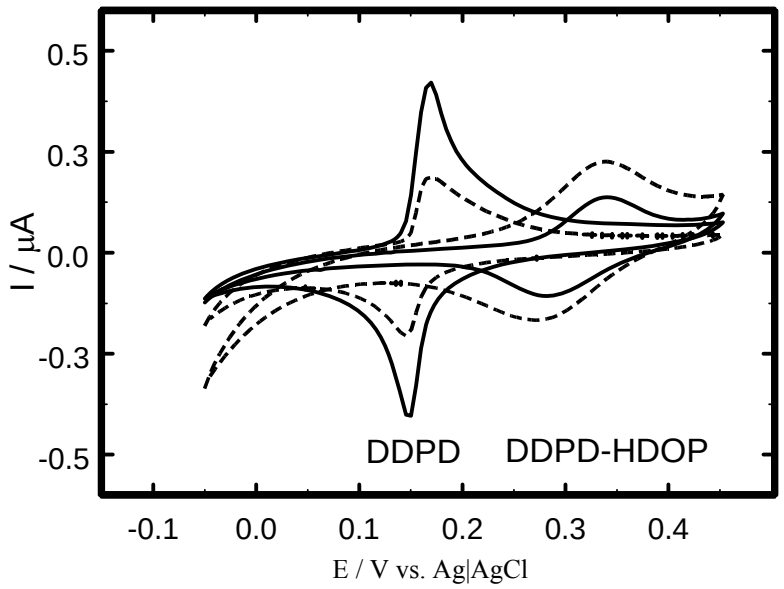

Fig.92. Cyclic voltammograms obtained with Au (solid line) and Au|MTMOS$_{gel}$ (dashed line) electrodes modified with 1.9 nmole of DDPP undiluted or diluted (1:8) with HDOP and immersed in 0.1 mol dm^{-3} KClO$_4$ aqueous solution. Scan rate 10 mV s^{-1}; surface area 0.02 cm^2.

For Au and Au|MTMOS$_{gel}$ electrodes with deposited diamine droplets the stable voltammograms with well defined sharp peaks are obtained. As it was shown above,

the electrode process is described by the eq.31. The smaller peak current obtained for Au|MTMOS$_{gel}$ electrode is probably caused by limited access to the active electrode surface. This indicates that Au|MTMOS$_{gel}$ is partially blocked by silicate film. The efficiency of the electrooxidation process at Au and Au|MTMOS$_{gel}$ electrode is low. Its value is less than 1% and is 10 and 100 times smaller than for CCE [221] and bppg [135] electrodes with the same deposit indicating poor development of the electrode surface. This is consistent with the result obtained for *t*BuFc deposit (Chapter 6.1).

In the presence of DDPD-HDOP droplets wide voltammetric peaks were obtained. Compare to electrodes with DDPD deposit, the shift of the peak potential to positive values was observed. This is because the mechanism of the oxidation process is changed. Instead of anion transfer from the aqueous solution the expulsion of proton from acid-base complex (see below) into the unbuffered solutions takes place [1]:

$$\text{HDOP-DDPD}_{(oil)} \leftrightarrow \text{DPO}\ldots\text{DDPD}^{+}{}_{(oil)} + \text{H}^{+} + \text{e} \qquad (32)$$

Continuous scanning of Au|MTMOS$_{gel}$ electrode with HDOP-DDPD deposit results in re-emerging of the voltammetric signal corresponding to the eg.31 [1]. Analogous experiment with the bare Au electrode (Fig.91) results in the decrease of acid-base complex signal with only a trace of the DDPD signal reappearing similarly as it was observed on bppg electrode [135]. In the case of Au|MTMOS$_{gel}$ electrode the comparable current magnitude are obtained for DDPD and DDPD-HDOP droplets. Contrary to the voltammograms observed for neat DDPD a linear dependence of peak currents upon the square root of scan rate is observed for DDPD–HDOP (not shown), indicating that process described by the eq.32 is diffusion limited. This change in DDPD behaviour can be caused by dilution of redox probe in acid.

The role of the proton in the electrode process was checked by the set of experiments in aqueous phosphate buffer at different pH values [135]. Indeed, for both Au and Au|MTMOS$_{gel}$ electrodes, the midpoint potential is shifted to more negative values with pH increase (Fig.93).

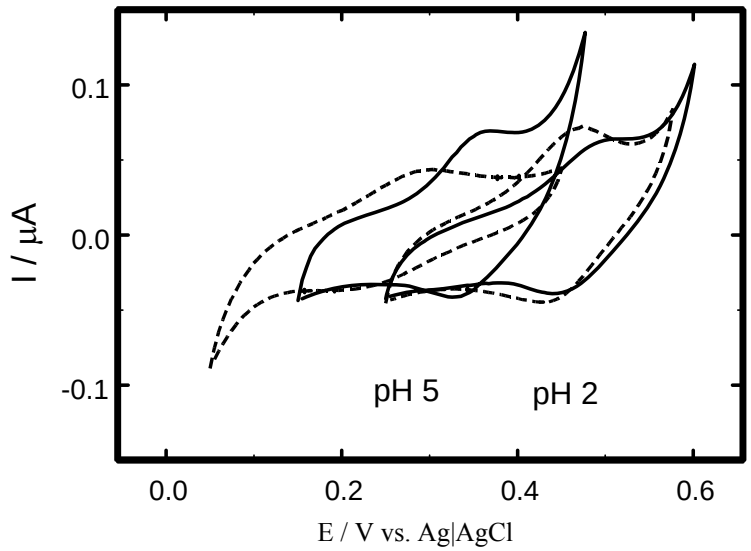

Fig.93. Cyclic voltammograms obtained with Au (solid line) and Au|MTMOS$_{gel}$ (dashed line) electrodes modified with 1.9 nmole nmole of DDPPD diluted (1:8) with HDOP and immersed in 0.1 mol dm^{-3} phosphate buffer at pH = 2 and 5. Scan rate 10 mV s^{-1}; surface area 0.02 cm^2.

Some effect of the hydrophobic thin film on voltammograms is noticeable. The midpoint potential shifts towards more negative values, by 0.03-0.06 V, than for the unmodified electrode.

The pH effect can be described by the Nernst type dependence according to the following equation [134]:

$$E^0 = E^{0\prime} + \frac{RT}{F}\ln\frac{[DPO^- - DDPD^+](oil)}{[HDOP - DDPD](oil)} - 2.303\frac{RT}{F}pH \qquad (33)$$

The linear dependence of E^0 vs. pH is observed for both electrodes (Fig.94). The close to Nernstian slope (0.057 V pH^{-1}) for Au|MTMOS$_{gel}$ and below (0.045 V pH^{-1}) for Au electrode similarly to CCE [3] and bppg [135], confirms the mechanism described by the eq.32. The silicate modified electrode is more sensitive to the pH than unmodified one. This may be connected with specific properties of the organic | silicate | aqueous solution triple interface. The concentration of hydrated protons may be larger than in the bulk of electrolyte due to their attraction to oxygen atoms bridging Si atoms as well to unreacted -OH groups [29]. Therefore a locally lower pH is expected to be sensed by an Au|MTMOS$_{gel}$ electrode. This is actually

observed: the E^0 vs pH dependence obtained with Au|$MTMOS_{gel}$ electrode is shifted towards lower pH by 0.5-2 units.

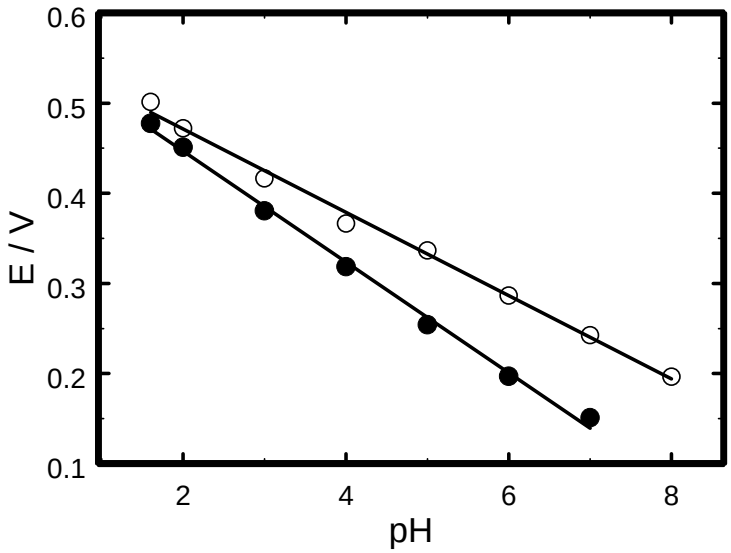

Fig.94. Plot of midpoint potential (E^0) vs. pH obtained for with Au (open circles) and Au|MTMOS (filled circles) modified with 1.9 nmole of DDPPD diluted (1:8) with HDOP and immersed in 0.1 M phosphate buffer at pH from 2 to 8. Scan rate 10 mV s^{-1}; surface area 0.02cm^2; reference electrode Ag|AgCl.

To prove that acid-base complex is formed the FTIRRAS spectroscopy was employed. The droplets of DDPD, HDOP-DDPD and HDOP were deposited on the gold coated glass slides and the IR spectra of these systems were recorded (Fig.95).

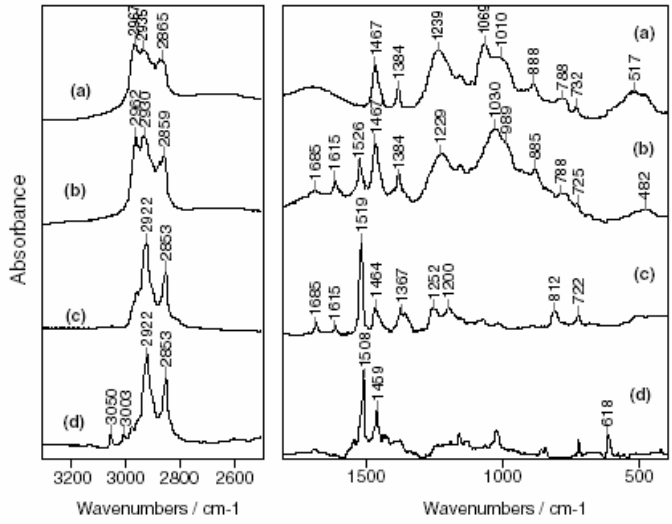

Fig.95. FTIRRAS spectra of a) HDOP, b) HDOP-DDPD, c) DDPD and d) DDPD droplets conditioned in 1 mol dm^{-3} aqueous HCl solution on the gold coated glass slides.

There are minor differences between DDPD and DDPD-HDOP spectra. However comparison of DDPD and DDPD-HDOP spectra shows major differences. The most significant shifts are present in the P-OR and P-OH of stretching vibration range. The bands assigned to acid from 1069 and 1010 cm^{-1} shift to 1030 and 989 cm^{-1} after DDPD was added. This shows strong interaction between DDPD and HDOP. The free pair of electrons placed on nitrogen from DDPD form a bond with hydrogen present in phosphates group of HDOP. On this basis on can state that complex is formed (Fig.96). To exclude amine protonation the experiment with deposited DDPD droplets in 1 mol dm^{-3} HCl aqueous solution was also done. The bands at 3050, 3003 cm^{-1} (stretching) and 618 cm^{-1} (out of plane deformation) can be assigned to $N\text{-}H^{+}$ group (Fig.95c). Since these modes are not found for HDOP-DDPD mixture (Fig.95b), the structure shown in Fig.96 seems to be the most accurate description of HDOP-DDPD complex.

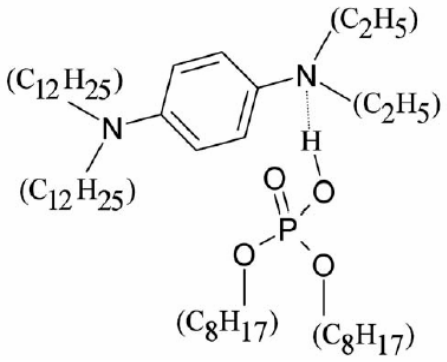

Fig.96. Molecular structure of DDPD-HODP complex.

Summary

In this paragraph the electrochemical behaviour of based on neat and diluted DDPD deposited on Au and Au|$MTMOS_{gel}$ electrodes were compared. Comparing to heterogeneous surface electrodes like CCE or bppg electrodes they exhibits 10 and 100 times smaller efficiency of electrode process. These differences are probably caused by the decrease of active surface area and the shorter length of the three phase junction. The presence of silicate layer clearly affects pH sensitivity of this system. However its application as pH sensor is limited to the acidic and neutral pH, because of silicate film decomposition in basic media [25].

6.6.3. Ionic liquids and NPOE supported system

Next the deposit of redox probe solution in RTIL's was studied. Before the electrode was modified with silicate thin film as electrode support these systems were studied on unmodified electrode. This is because of the absence of such results in literature. For comparison the solution of redox probes and organic salts in polar hydrophobic solvent - NPOE were also used for electrode modification.

At first electrochemical properties of electrodes modified with drop of *t*BuFc solution in three ionic liquids of different hydrophobicity were studied. Two of them have common cation and another pair have a common anion, 1-decyl-3-methylimidazolium bis(trifluoromethylsulfonyl)imide (C_{10}mimN$(Tf)_2$), 1-butyl-3-methylimidazolium bis(trifluoromethylsulfonyl)imide (C_4mimN$(Tf)_2$) and 1-butyl-3-methylimidazolium hexafluorophosphate (C_4mimPF_6), respectively (Fig.97).

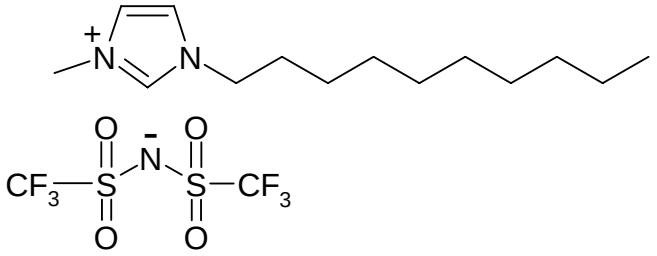

C_{10}mimN$(Tf)_2$

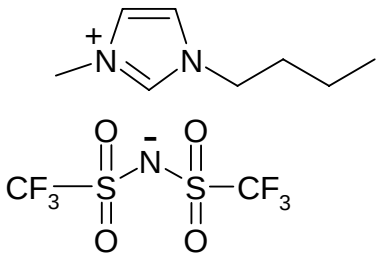

C_4mimN$(Tf)_2$

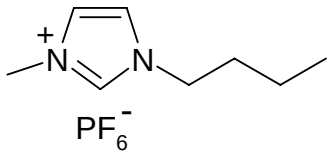

C_4mimPF_6

Fig.97. The structrure of a) 1-decyl-3-methylimidazolium bis(trifluoromethylsulfonyl)imide (C_{10}mimN$(Tf)_2$), b) 1-butyl-3-methylimidazolium bis(trifluoromethylsulfonyl)imide (C_4mimN$(Tf)_2$) and c) 1-butyl-3-methylimidazolium hexafluorophosphate (C_4mimPF_6)

6.6.3.1. Au and Au|MTMOS$_{gel}$

Au and Au|MTMOS$_{gel}$ electrodes were modified with a drop of 0.01 mol dm^{-3} of *t*BuFc solution in RTIL. In the case of C_{10}mimN(Tf)$_2$ after immersion into 0.1 mole dm^{-3} KPF_6 aqueous solution the stable and symmetric voltammogram was obtained (Fig.98).

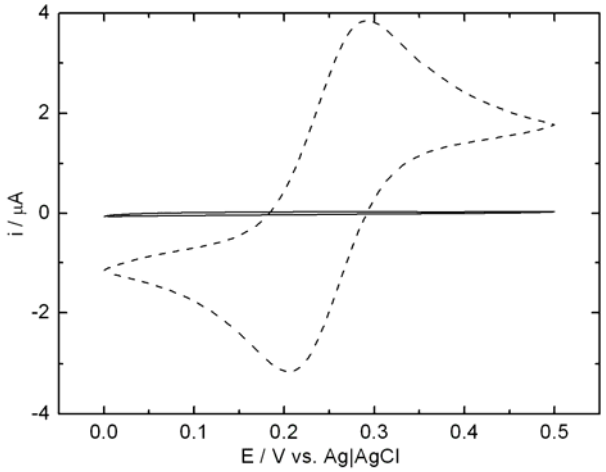

Fig.98. Cyclic voltammograms (3rd scan, scan rate 0.01 V s^{-1}) obtained with Au electrode covered with 2 μl of 0.01 mol dm^{-3} tBuFc solution in C_{10}mimN(Tf)$_2$ immersed in 0.1 mol dm^{-3} aqueous KPF_6 (dashed) and with the same electrode in the absence of tBuFc (solid). Surface area 0.02 cm^2.

The electrooxidation/reduction process occurring at this electrode can be described as follows:

$$t\text{BuFc}_{(\text{RTIL})} - \text{e} \leftrightarrow t\text{BuFc}^{+}_{(\text{RTIL})} \tag{34}$$

To maintain the neutrality of the RTIL phase three following reactions can take place:
an anion insertion from the aqueous solution into RTIL phase:

$$t\text{BuFc}^{+}_{(\text{RTIL})} + \text{X}^{-} \leftrightarrow t\text{BuFc}^{+}_{(\text{RTIL})} + \text{X}^{-}_{(\text{RTIL})} \tag{35}$$

expulsion of oxidised form of the redox probe from RTIL phase into the aqueous solution:

$$t\text{BuFc}^{+}_{(\text{RTIL})} - \text{e} \leftrightarrow \text{tBuFc}^{+}_{(\text{aq})} \tag{36}$$

or ejection of cationic component of RTIL to the aqueous solution:

$$C_{10}mimN(Tf)_2^{+}{}_{(RTIL)} \leftrightarrow C_{10}mimN(Tf)_2^{+}{}_{(aq)} \quad (37)$$

This reaction is probable, because the concentration of nonelectroactive cations is almost three orders of magnitude larger than that of the redox probe If the electrooxidation of *t*BuFc is accompanied by an anion insertion into the RTIL phase (eq.35) the formal potential ($E_{red/ox}$) is described by a Nernstian type of equation [135]:

$$E_{red/ox} = E^0_{tBuFc^+_{RTIL}/tBuFc_{RTIL}} + \Delta^{RTIL}_{aq}\varphi^0_{X^-} + \frac{RT}{F}\ln c_{X^-} + \frac{RT}{F}\ln\frac{c^*_{tBuFc_{aq}}}{2} \quad (38)$$

where $E^0_{tBuFc^+_{RTIL}/tBuFc_{RTIL}}$ is the standard redox potential for the *t*BuFc$^+$/*t*BuFc couple in the ionic liquid solution, $\Delta^{RTIL}_{aq}\varphi^0_{X^-}$ is the standard transfer potential of anion X^- from water into the RTIL phase, and c_{X^-} and $c^*_{tBuFc_{aq}}$ is initial concentration of X^- and *t*BuFc in aqueous solution and RTIL, respectively. The slope of linear plot of $E_{red/ox}$ vs. $\Delta^{RTIL}_{aq}\varphi^0_{X^-}$ is expected to be unity and the slope $E_{red/ox}$ vs. $\log(c_{X^-})$ should be equal 0.059 V dec^{-1} and can be used as diagnostic criteria of the electrode reaction.

At first the experiments in the presence of selected anions in aqueous solution was done. The Au electrodes were modified with drop of 0.01 mol dm^{-3} of *t*BuFc in three studied RTIL and immersed into the aqueous solution of different anions. The redox potentials were estimated from differential pulse voltammograms (Fig.98) and they should be plotted versus standard transfer potential of an anion transfer from the aqueous solution into the RTIL. The latter parameter is unavailable and was replaced with standard potential of anion transfer from aqueous solution into NB (Fig.99) as a measure of an anion hydrophobicity [138].

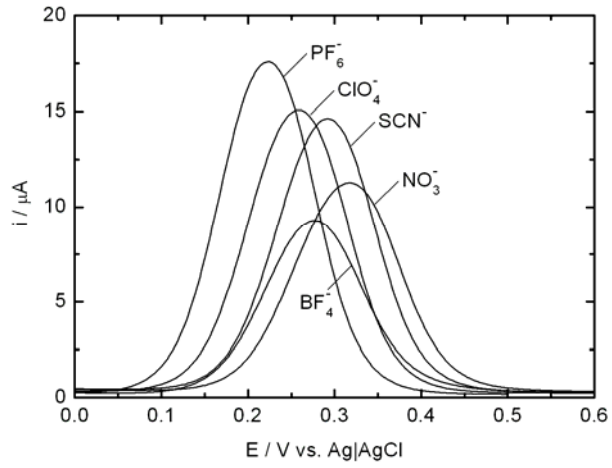

Fig.98. The effect of selected anions on differential pulse voltammograms obtained with Au electrode covered with 2 μl of 0.01 mol dm^{-3} tBuFc solution in C_{10}mimN(Tf)$_2$ immersed in 0.1 mol dm^{-3} aqueous salt solution. Surface area 0.02 cm^2.

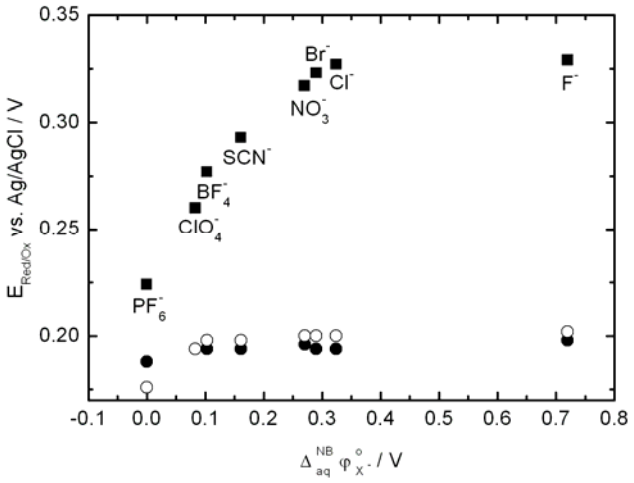

Fig.99. The plot of redox potential, $E_{Red/Ox}$ obtained with Au electrode covered with 2 μl of 0.01 mol dm^{-3} tBuFc solution in C_4mimN(Tf)$_2$ (○), C_4mimPF$_6$ (●) and C_{10}mimN(Tf)$_2$ (■) vs. standard transfer potential of anion transfer from aqueous solution to nitrobenzene, $\Delta_{aq}^{NB}\varphi_{X^-}^0$.

One can easily judge, that probability of an anion transfer into RTIL phase strongly depends on hydrophobic-hydrophilic properties of the ionic liquid and an anion in the aqueous solution. For *t*BuFc dissolved in C_4mimN(Tf)$_2$ or C_4mimPF$_6$ electrooxidation of the redox probe it is almost not affected by the type of anion present in aqueous phase. In this case electrode process is described by the eq.34 and 36 or 37. This is probably because the Gibbs energy of C_4mim^+ cation transfer to an aqueous solution is smaller than for any of selected anions. Moreover, the redox

probe is much easier oxidised in more hydrophilic RTIL's (0.05-0.2 V) than in hydrophobic C_{10}mimN$(Tf)_2$. In the latter case one can observe influence of an anion on peak potential. It is shifted towards more negative values with increasing of hydrophobic properties of X^-. The $E_{red/ox}$ vs. $\Delta_{aq}^{NB}\varphi_{X^-}^0$ dependence is not linear (Fig.99). Its slope changes from slightly below unity for the most hydrophobic anions (PF_6^-, ClO_4^-) to close to zero for the most hydrophilic ones (Cl^-, F^-) as it is shown in Table 4. This behaviour indicates that to maintain the neutrality PF_6^- anion is transferred into RTIL phase. The opposite effect, like ejection of *t*BuFc$^+$ or/and $C_{10}mim^+$ from RTIL phase, occurs in the presence of F^- in the aqueous solution. To prove this hypothesis, additional the experiment with different concentration of selected anions were done (Fig.100).

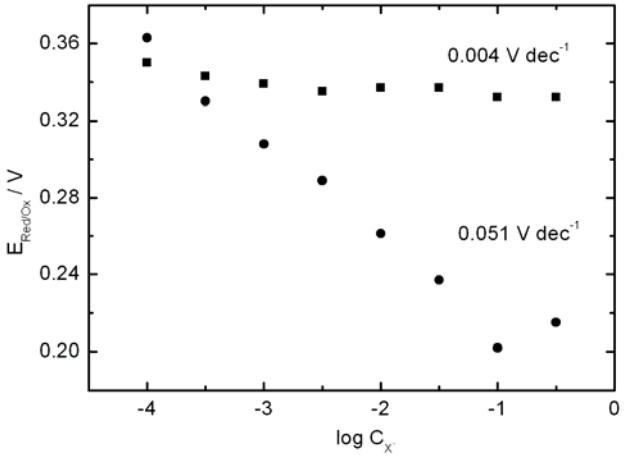

Fig.100. The $E_{Red/Ox}$. vs log c_{X^-} of Cl^- (■) and PF_6^- (●) dependence obtained with Au electrode covered with 2 μl of 0.01 mol dm^{-3} tBuFc solution in $C_{10}mimNTf_2$. Surface area 0.02 cm^2.

Table.4. The slope of $E_{Red/Ox}$. vs log c_{X^-} dependence obtained with Au electrode covered with 2 μl of 0.01 mol dm^{-3} tBuFc solution in $C_{10}mimNTf_2$.

anion	$-\delta E_{Red/Ox}/\delta c$ / V
F^-	0.006
Cl^-	0.004
BF_4^-	0.019
ClO_4^-	0.040
PF_6^-	0.051

The close to Nernstian slope of linear dependence between peak potential $E_{Red/Ox}$. vs. concentration (0.051 V dec $^{-1}$) observed for hydrophobic anion and almost zero for hydrophilic one confirms the mechanism of the electrode process suggested above and can be described by the Fig.101.

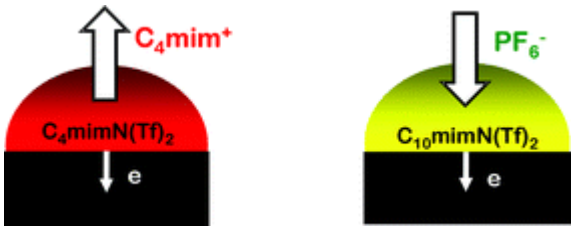

Fig.101. The direction of ion transfer across RTIL's|aqueous electrolyte solution coupled to electrochemical redox reaction.

Next, the Au|MTMOS$_{gel}$ electrode was modified with a drop of 0.01 mol dm^{-3} of *t*BuFc in C_{10}mimN(Tf)$_2$ and immersed into 0.1 mole dm^{-3} aqueous solutions of selected anions. The similar behaviour like for Au electrode was obtained. The shift of peak potential to more positive values was observed together with enhancement of hydrophilic properties of anions presente in aqueous solution.

For comparison the RTIL was replaced by salt solution in 2-nitrophenyloctylether (NPOE) a high water-insoluble solvent. The Au electrode was modified with droplets of 0.01mol dm^{-3} of *t*BuFc in supported NPOE and immersed into aqueous solution of different anions. Contrary to the RTIL drop presents at the electrode surface the NPOE deposit forms thin film. This effect is probably caused by differences in surface energy. The voltammetric response obtained with Au electrode modified with NPOE supported with different hydrophobic properties tetraalkylammonium salt are presented in Fig.102.

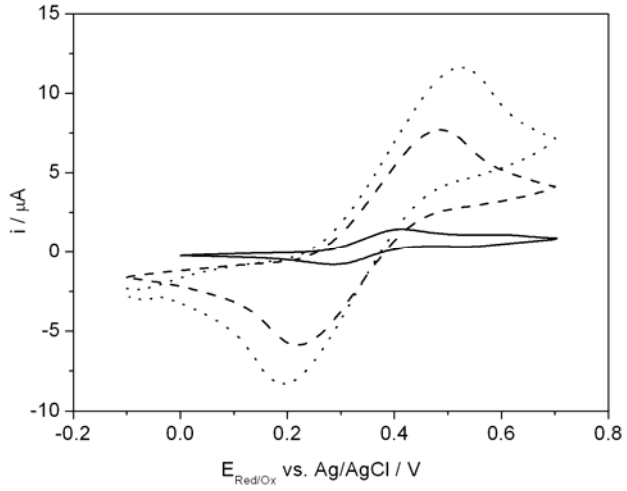

Fig.102. Cyclic voltammograms (3rd scan, scan rate 0.01 V s^{-1}) obtained with Au electrode covered with 2 μl of 0.01 mol dm^{-3} tBuFc solution in 0.1 mol dm^{-3} TBAP (dotted), 0.1 mol dm^{-3} THAP (dashed) and 0.05 mol dm^{-3} TOAP (solid) supported NPOE immersed in 0.1 mol dm^{-3} aqueous KPF_6. Surface area 0.02 cm^2.

The position of voltammetric peaks on potential scale does not depend on salt dissolved in NPOE. On the other hand, peak current decreases in the presence of larger, more hydrophobic cations in organic phase. This may be connected with their adsorption on the electrode surface leading to its partial blocking [222,223].

Also in this case the electrooxidation/reduction process occurring at Au electrode can be described by the eq.34. In order to evaluate direction of the ion transfer following this reaction the similar experiments as for RTIL modified electrode has to be done. Fig.103 clearly shows that contribution of an anion insertion depends on the composition of organic phase. For NPOE phase supported by more hydrophobic salt like THAP or TOAP the linear plot with slope not very far from unity (0.73 and 0.76 respectively) indicates dominating contribution of an anion insertion. On the other hand, the transition from an anion insertion to tBuFc$^+$ cation ejection to the aqueous solution is observed for unsupported NPOE and TBAP supported organic phase. In this case the also the ejection of less hydrophobic non-electroactive TBA^+ cation into the aqueous solution is possible [224]. It has to be emphasised that for unsupported NPOE deposit tBuFc$^+$ ejection occurs.

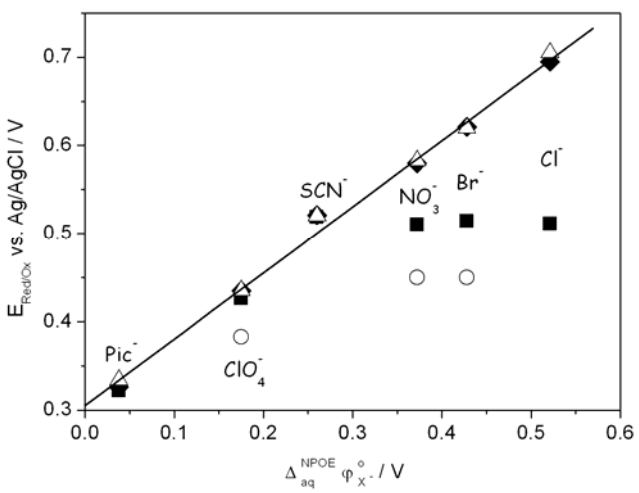

Fig.103. Plot of the peak potential from differential pulse voltammograms, $E_{Red/Ox}$, versus the standard transfer potential for anion transfer from aqueous media to NPOE, $\Delta_{aq}^{NPOE}\varphi_{X^-}^0$. $E_{Red/Ox}$ values were determined from differential pulse voltammograms with Au electrode covered with 2 μl of 0.01 mol dm^{-3} tBuFc and 0.05 mol dm^{-3} TOAP (♦), 0.1 mol dm^{-3} THAP (▲), 0.1 mol dm^{-3} TBAP (■) solution in NPOE and pure NPOE (○) and immersed in aqueous 0.1 mol dm^{-3} salt solutions. The sequence of anions is indicated and the solid line corresponds to linear regression of data obtained with 0.05 mol dm^{-3} TOAP.

The tabulated values of the standard transfer potentials of X^- from water to nitrobenzene ($\Delta_{Aq}^{NB}\varphi_{X^-}^0$) were employed for further data analysis (Fig.104) because this parameter is known for a wider range of anions than for NPOE (Fig.103).

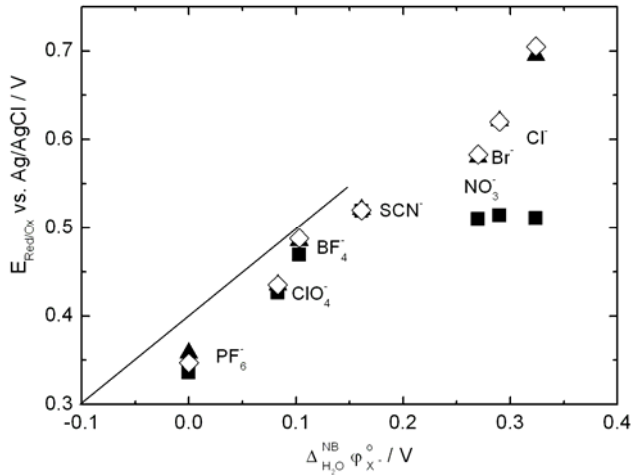

Fig.104. Plot of the peak potential from differential pulse voltammograms, $E_{Red/Ox}$, versus the standard transfer potential for anion transfer from aqueous media to NB, $\Delta_{aq}^{NB}\varphi_{X^-}^0$. $E_{Red/Ox}$ values were determined from differential pulse voltammograms with Au electrode covered with 2 μl of 0.01 mol dm^{-3} tBuFc and 0.05 mol dm^{-3} TOAP (◊), 0.1 mol dm^{-3} THAP (▲), 0.1 mol dm^{-3} TBAP (■) solution in NB and immersed in aqueous 0.1 mol dm^{-3} salt solutions. The sequence of anions is indicated and the slope of solid line is equal unity.

For NPOE supported with lipophilic ammomium slats THAP and TOAP insertion of anions into NPOE phase is observed. This effect is confirmed by the linear plot of $E_{red/ox}$ vs. $\Delta_{Aq}^{NB}\varphi_{X^-}^{0}$ with slope close to unity 0.96 and 0.92 for THAP and TOAP, respectively. When less lipophilic TBAP salt is present in NPOE this dependence decreases from being close to unity for the most hydrophobic anions like PF_6^-, ClO_4^-, BF_4^- and SCN^- to close zero for the hydrophilic anions.

Summary

Summarising, the ability of an anion insertion into the RTIL's from aqueous solution was confirmed for both Au and Au|$MTMOS_{gel}$ electrodes. The obtained results allow to suggest the pattern of $\Delta_{aq}^{RTIL}\varphi_{X^-}^{0}$ as $Cl^- > Br^- > NO_3^- > BF_4^- > SCN^- > ClO_4^- > PF_6^-$similar to the Hofmeister one. When RTIL was replaced by supported NPOE the direction of ion transfer is depends on the hydrophobic properties of cation present in organic phase. The expulsion of electrogenerated or non-electroactive cation is replaced by an anion insertion together with decrease of hydrophilic properties of tetraalkylammonium cation in the organic phase. This is opposite to that reported earlier for similar system: transition from an anion insertion to non-electroactive cation ejection after addition of tetrabutylammonium salt to NPOE [224]. Obviously the preferential solvation of hydrophobic cations in the organic phase prevents them from ejection into the aqueous solution. In this work only ejection of TBA^+ cation can be judged.

6.6.3.2. ITO|CNF,SiO_2,$MTMOS_{gel}$

First, affinity of RTIL towards CNF-silica film the electrode was tested in the absence of redox probe, after its modification with 0.5 μl of RTIL. As one can judge with naked eye this results in complete coverage of the electrode with liquid film. For these experiments C_{10}mim$N(Tf)_2$ was chosen, because the influence of an anion on peak potential was already noticed (Chapter 6.6.3.1). The resulting capacitive current obtained by CV in aqueous salt solution is approximately 2 orders of magnitude larger than that obtain for film deposited on unmodified ITO surface (Fig.105). This indicates quite good wetting of extended CNF surface by C_{10}mim$N(Tf)_2$.

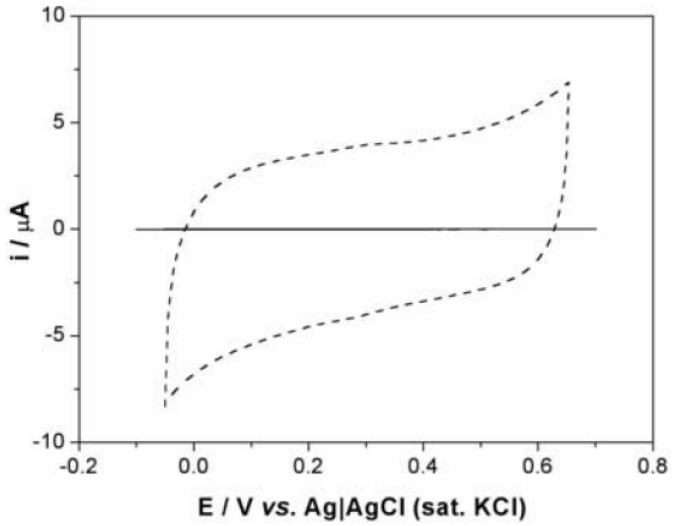

Fig.105. Cyclic voltammetry (2nd scan, scan rate 10 mV s^{-1}) obtained for hydrophobic CNF-silica film modified ITO (dashed line) and unmodified ITO (solid line) electrodes with deposited 0.5 μl of $C_{10}mimN(Tf)_2$ immersed in aqueous 0.1 mol dm^{-3} $NaClO_4$. Surface area 0.2 cm^2

Next, the electrochemical properties of redox probe dissolved in RTIL deposit were investigated. Both ITO and ITO with deposited CNF – silica film were modified with redox probe solution in RTIL. Typical results obtained in the aqueous 0.1 mol dm^{-3} $NaClO_4$ solution are presented in Fig.106.

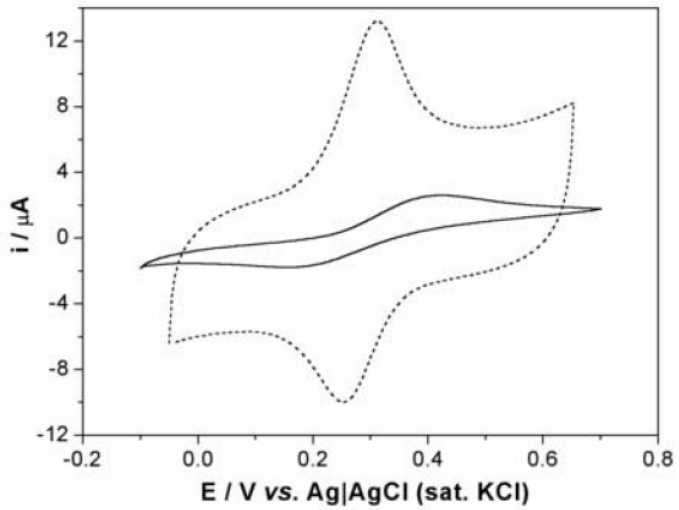

Fig.106. Cyclic voltammetry (2nd scan, scan rate 10 mV s^{-1}) obtained for hydrophobic CNF-silica film modified ITO (dashed line) and unmodified ITO (solid line) electrodes with deposited 0.5 μl 0.01 mol dm^{-3} tBuFc solution in $C_{10}mimN(Tf)_2$ (5 nmole of tBuFc in RTIL) immersed in aqueous 0.1 mol dm^{-3} $NaClO_4$. Surface area 0.2 cm^2.

Both peak shaped voltammograms results from the electrooxidation/reduction process occurring in RTIL phase described by eq.34. However, modification of the electrode with CNF's substantially affects the shape voltammetric response. Namely both the charges and the peak currents are much larger on modified electrode. Clearly, this is because of the increase of both capacitive and faradaic contributions to the current. The smaller effect is observed for the latter, because only about 5-fold increase of peak current is observed. The efficiency of electrode process was determined and its value obtained from 2nd scan is equal to 37 % and 11 %, for CNF – silica ITO and ITO electrode respectively. Therefore, the presence of CNF substantially increases efficiency of this process because of well developed surface.

The continuous scanning ITO|CNF,SiO_2,$MTMOS_{gel}$ electrode with *t*BuFc present in RTIL film affects stability of voltammograms (Fig.107).

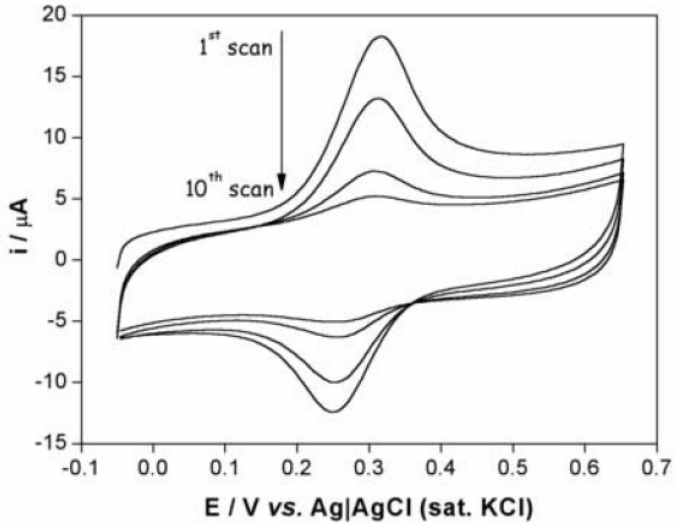

Fig.107. Cyclic voltammograms (1st, 2nd,5th and 10th scan, scan rate 10 mV s^{-1}) obtained for hydrophobic CNF-silica film modified ITO electrode with deposited 0.5 μl 0.01 mol dm^{-3} tBuFc solution in C_{10}mimN(Tf)$_2$ (5 nmole of tBuFc in RTIL) immersed in aqueous 0.1 mol dm^{-3} $NaClO_4$. Surface area 0.2 cm^2.

The decrease of faradaic current during subsequent scans is observed. It probably results from *t*BuFc$^+$ expulsion into the aqueous solution (eq.36.) following eq.34. The value of anodic to cathodic charge ratio (Q_a/Q_c) larger than unity supports this conclusion. Similarly like in the case of Au electrode ejection of C_{10}mim$^+$ cations to the aqueous solution has to be also taken into account (page 109).

The electrochemical behaviour of studied electrodes was examined in the presence of a wide range of anions. The differential pulse voltammetry of the electrooxidation of 5 nmole tBuFc in C_{10}mimN$(Tf)_2$ solution deposited at CNF – silica film after immersion in various aqueous electrolytes is presented in Fig.108.

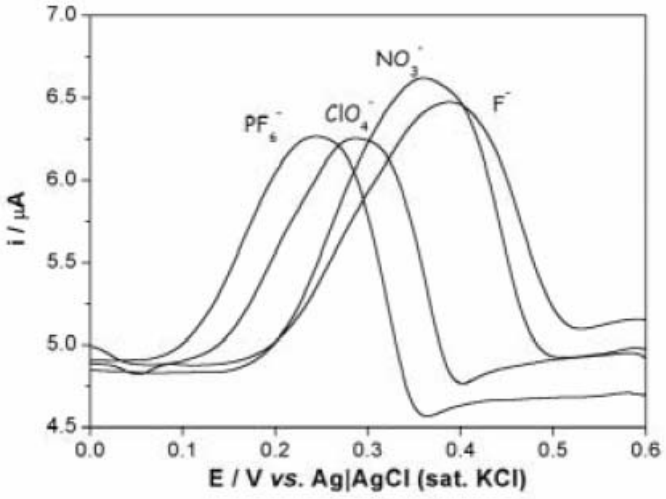

Fig.108. Differential pulse voltammograms obtained for CNF-silica film modified ITO electrode with deposited 0.5 μl 0.01 mol dm^{-3} tBuFc solution in C_{10}mimN$(Tf)_2$ (5 nmole of tBuFc in RTIL) immersed in aqueous 0.1 mol dm^{-3} solution of anions. Surface area 0.2 cm^2.

As before the shift of $E_{red/ox}$ indicates the effect of the anion on ability of *t*BuFc to be electrooxidised. It suggests, that the electrode process is composed of heterogeneous electron transfer (eq.34) followed by anion insertion (35).

Indeed, for all electrodes studied the slope of the dependence of $E_{red/ox}$ vs. $\Delta_{aq}^{RTIL}\varphi_{X^-}^0$ (Fig.109) decreases from being close to unity for most hydrophobic anions like PF_6^- or ClO_4^- to close to zero for most hydrophilic anions. This reflects transistion from hydrophobic anion insertion (eq.35) to cation ejection (eq.36, 37). The mechanism of the electrode process strongly depends on the type of the electrode. As it was shown for Au electrode also for CNF-modified electrodes two zones exists: “electron transfer zone” and “ion transfer zone” (Fig.110).

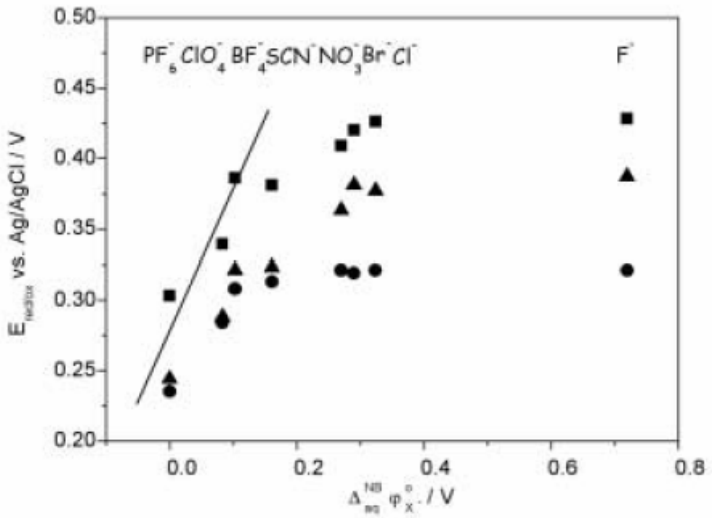

Fig.109. The peak potential ($E_{red/ox}$) vs. standard transfer potential of anion from aqueous solution to NB ($\Delta_{aq}^{NB}\varphi_{X^-}^0$) plot obtained after electrode modification with 0.5 μl 0.01 mol dm^{-3} tBuFc solution in C_{10}mimN(Tf)$_2$. The presented data were obntained on ITO|CNF-silica|RTIL film (■), ITO|RTIL film (▲) and ITO|CNF-silica|RTIL microphases (●) electrodes. The slope of solid line is equal unity. Surface area 0.2 cm^2.

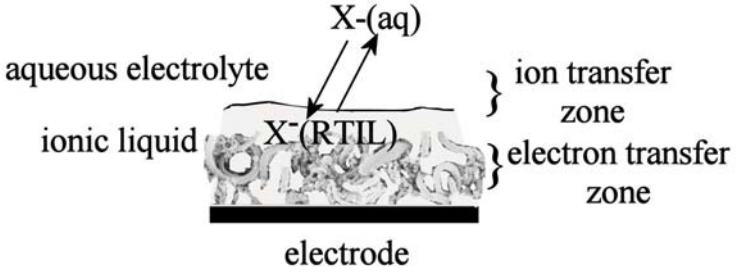

Fig.110. The suggested structure of ITO electrode covered with hydrophobic CNF – silica film and covered with RTIL film. The "electron transfer zone" and "ion transfer zone" are indicated.

It seems to that the increasing gap between these zones limits the loss of $tBuFc^+$ and changes the behaviour of the electrode. For a given anion the value of $E_{red/ox}$ is shifted into the negative direction in order ITO|CNF,SiO_2,$MTMOS_{gel}$ RTIL film > ITO|RTIL film > ITO|CNF,SiO_2,$MTMOS_{gel}$ microphases by 0.07 – 0.11 V. CNF-silica electrode modified with RTIL film the effect of cation ejection became important where NO_3^-, Br^- or Cl^- are present in the aqueous solution. For the same anions this effect is stronger for bare ITO modified with film of RTIL. In the case of ITO|CNF,SiO_2,MTMOSgel modified with microphases, cation expulsion into the

aqueous solution occurs even in the presence of more hydrophobic anions in the aqueous solution.

Next, the RTIL was replaced by supported NPOE. Similarly to RTIL based system, the role of the extended surface of CNFs in the electrode process is important as can be seen from the comparison of the currents for voltammograms obtained in the presence and in the absence of the hydrophobic CNF-silica film (Fig. 111i, 111iii). The capacitive currents are significant for CNF modified electrodes due to both good wetting of CNFs by the NPOE solvent and the presence of supporting electrolyte in the organic phase. For both supporting electrolytes TOAP and TBAP after 2nd scan the stable voltammograms were obtained and electrode process efficiency decreased only from 27% (1st scan) to 14% (10th scan). It is probably because electrogenerated $tBuFc^+$ cations are attracted by hydrophobic CNFs and are not in direct contact with aqueous solution. Therefore they remain in the organic phase.

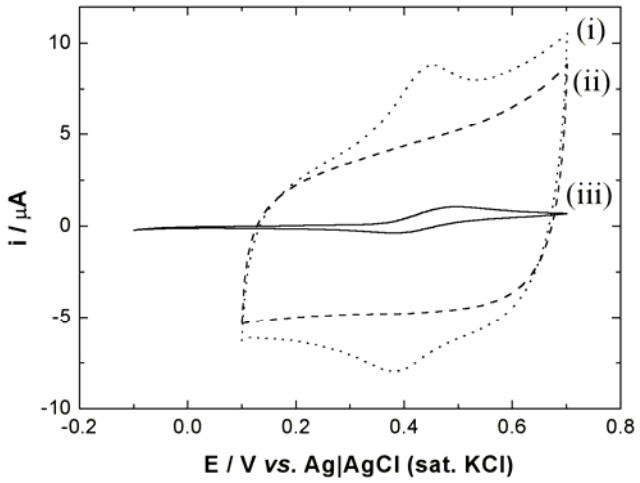

Fig.111. Cyclic voltamogramms (5th scan) obtained for the oxidation of (i) 0.01 mol dm-3 tBuFc and 0.1 mol dm-3 TOAP solution in NPOE (dotted) and (ii) the same solution in ansence of tBuFc (dashed) immobilised in a hydrophobic CNF-silica film deposited onto ITO substrates and immersed in aqueous 0.1 mol dm-3 NaClO4 (iii) the solid line corresponds to the same experiment performed with a bare ITO electrode.

Next, the hydrophobic CNF-silica electrode modified with redox probe solution in NPOE was examined in the presence of a wider range of anions in

aqueous solution. The typical differential pulse voltammograms are presented in (Fig.112)

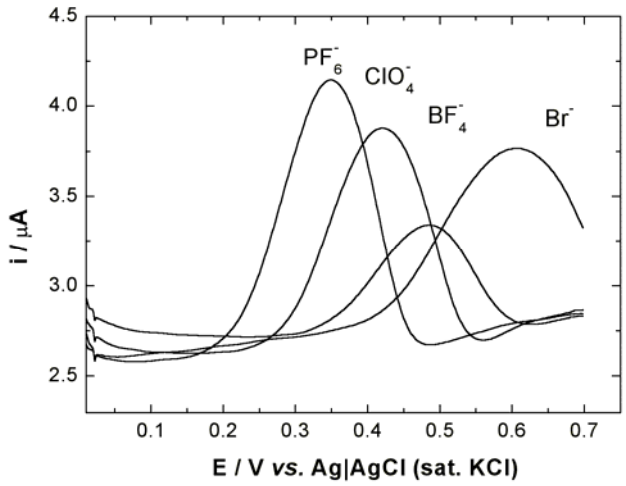

Fig.112. Differential pulse voltammograms obtained for CNF-silica film modified ITO electrode with with deposited 5 μl 0.01 mol dm^{-3} tBuFc solution and 0.1 mol dm-3 TOAP in NPOE(5 nmole of tBuFc in RTIL) immersed in aqueous 0.1 mol dm^{-3} solution of anions. Surface area 0.2 cm^2.

Well-defined peaks are observed for the more hydrophobic anions and broadened peaks for the hydrophilic anions. The characteristic shift of peak potential, E_{peak}, clearly indicates that the anion transfer is dominating the overall process. From the data obtained in four different electrolytes the decrease of the slope from a value close to the expected for anion insertion (eq.35) can be seen for more hydrophilic anions (Fig.111A). This effect is much more pronounced for TBAP solutions in NPOE. Therefore it is likely that tetrabutylammonium or tetraoctylammonium cation transfer from the organic to the aqueous phase is important. Next, similarly to Au electrodes (Chapter 6.6.3.1) the values $\Delta_{Aq}^{NB}\varphi_{X^-}^0$ were employed for further data analysis (Fig.113A,B). Almost linear dependence of E_{peak} vs. $\Delta_{Aq}^{NB}\varphi_{X^-}^0$ with slope close to unity can be seen from the hydrophobic PF_6^- to the relatively hydrophilic Cl^-. Only for most hydrophilic anion, F^-, and in the presence of tetrabutylammonium cations, a deviation from this dependence can be seen indicating important contribution of the cation ejection.

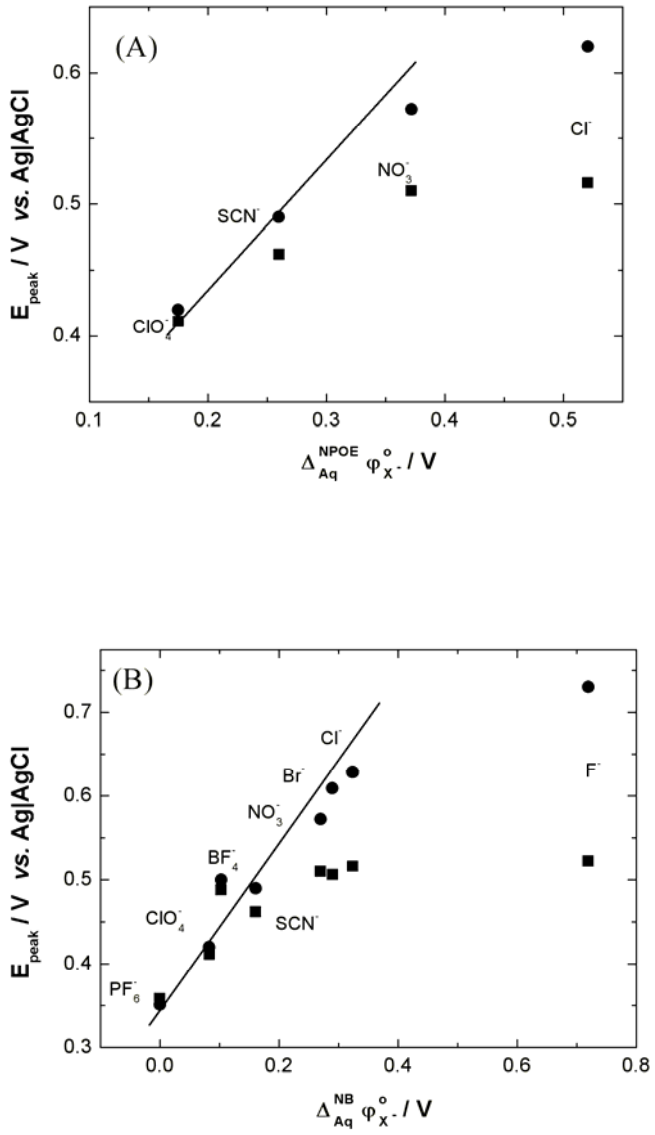

Fig.113. Plot of the peak potential from differential pulse voltammograms, E_{peak}, versus the standard transfer potential for anion transfer (A) from aqueous media to 2-nitrophenyloctylether (NPOE) $\Delta^{NPOE}_{Aq}\varphi^{0}_{X^-}$ and (B) to nitrobenzene (NB) $\Delta^{NB}_{Aq}\varphi^{0}_{X^-}$. E_{peak} values were determined from differential pulse voltammograms for the oxidation of 0.5 μl of 0.005 (0.01) mol dm^{-3} tBuFc and 0.05 (0.1) mol dm^{-3} TOAP (●) (TBAP (■)) solution in NPOE immobilised in a hydrophobic CNF – silica film deposited onto ITO substrates and immersed in aqueous 0.1 mol dm^{-3} aqueous electrolyte solutions. The sequence of anions is indicated and the solid line corresponds to the ideal Nernstian behaviour for a simple anion transfer process.

Summary

Hydrophobic CNF-silica film modified ITO electrodes with the redox probe in RTIL or in supported NPOE exhibits well-defined voltammetric response. The presence of the hydrophobic CNF-silica film enhances both the capacitive background and the magnitude of Faradaic current response. Moreover, it enhances the efficiency of the electrode process. The separation of the "electron transfer zone" (at the CNF surface) and the "ion transfer zone" (at the liquid | liquid interface) is believed to affect the direction of ion transfer.

7. Conclusions

In this work novel type of electrode surface modification by hydrophobic silicates for redox liquid immobilisation were proposed. It has been shown that hydrophobic silicate films based on MTMOS can be deposited on Au, Au pretreated with MPS, ITO or glass support. Furthermore MTMOS based film is a good framework for conducting nanoobjects like ITO nanoparticles or hydrophobic carbon nanofibres.

The composition of hydrophobic silicate films affects its topography. The MTMOS based film is reach of defects, whereas MPS based one is rich in protrusions. The MTMOS based film deposited on Au pretreated with MPS film combines these features. At this surface numerous of holes and objects sticking out of plane are present. The addition of nanoobjects enhances development of the surface. Moreover, carbon nanofibres enhances its hydrophobic properties.

The prepared hydrophobic films are to some extent permeable for the redox probe presented in aqueous solution. Importantly, the embedded conductive nanoobjects retain their electrical properties. The films are less transparent for ionic than for neutral species.

Hydrophobic and well developed films allow for pure and diluted redox liquid or RTIL immobilisation. In most cases the presence of hydrophobic silicate films prevents the expulsion of the electrogenerated cation and thereby stabilises electrode|redox liquid|aqueous solution systems. This effect is enhanced by the presence of MPS or CNFs. It seems to that free pairs of electrons placed on oxygen atoms, porous hydrophobic structure of CNFs and hydrophobic nature of MTMOS film are probably responsible for the stable voltammetric response. Not adsorbed SH groups may also attract the electrogenerated cations enhancing the retention effect of silicate matrix. In the case of CNF probably the hydrophobic sidewalls contribute to stable voltammetric response. Three exemptions of this behaviour were observed. These includes MTMOS based film deposited at Au or glass support with top thin gold layer and the same film with embedded ITO nanoparticles. Probably in both cases the surface of the electrode is not enough hydrophobic. On the other hand for the two latter electrodes significant increase of the electrode process efficiency was observed due to the presence of nanoobjects. The presence of hydrophobic carbon nanofibres enhances both stability of voltametric response and electrode process efficiency.

Additionally the electrochemistry of acid-base complex was also examined at hydrophobic silicate modified electrode. The use of this electrode material affects only to some extent the selectivity of this system towards pH.

Herein for the first time ion transfer across ionic liquid|aqueous solution interface not supported by any material, coupled to the electrochemical redox reaction was detected analysed. It turns that also in this case hydrophilic-hydrophobic properties of counterion present in aqueous phase plays important role. The RTIL based system was successfully immobilised on hydrophobic silicate – CNF's modified electrode and it exhibits large efficiency of the electrode process. The replacement of RTIL by supported organic polar solvent - NPOE does not much affect electrochemical characteristics of the electrode.

It has to be emphasised that all obtained films were mechanically stable and they could be reused after experiments with redox liquid and RTILs deposit after a simple organic solvent rinsing step.

Obviously not all possibilities of preparation of the electrode surface suitable for immobilisation of redox liquid were explored and many materials can be used for this purpose. Especially immobilisation of conducting nanoparticles with tailored surface and their assemblies seems to be promising. These systems can be eventually utilized for electrogenerated ion extraction from the aqueous solution, ion sensing and electrosynthesis at the liquid | liquid interface.

8. References

1. M.M. Collinson, Tr. Anal. Chem., 21 (2002) 30.
2. G. Shustak, S. Marx, I. Turyan, D. Mandler, Electroanalysis 15 (2003) 398.
3. J.D. Wright, N.A.J.M. Sommerdijk, „Sol-Gel Materials. Chemistry and Applications.“ Gordon and Breach Science Publisher 2001.
4. C. Sanchez, F. Ribert, New J. Chem., 18 (1994) 1007.
5. O.Lev, M. Tsionsky, L. Rabinovich, V. Glezer, S. Sampath, I. Pankratov, J. Gun, Anal Chem. 67 (1995) 22A.
6. B. Dunn, J.I. Zink, J. Mater. Chem., 1 (1991) 903.
7. L. Yang, S.S. Saavedra, Anal. Chem., 67 (1995) 1307.
8. V. Glezer, O. Lev, J. Am. Chem. Soc., 115 (1993) 2533.
9. J.A. Cox, J. Electrochem. Soc., 143 (1996) L126.
10. D. Avnir, D. Levy, R. Reisfeld, J. Phys. Chem., 88 (1984) 5956.
11. J. Wang, Anal. Chim. Acta, 399 (1999) 21.
12. A. Walcarius, Electroanalysis, 13 (2001) 701.
13. Y. Guo, L.A. Colon, Chromatographia, 43 (1996) 477.
14. J.D. Hayes, A. Malik, J. Chromatrogr., B 695 (1997) 3.
15. A. Walcarius in: H.S. Nawla (Ed.), Encyclopedia of Nanoscience and Nanotechnology, Vol. 2 American Scientific Publishers, Stevenson Ranch, CA 857
16. L. Rabinowich, J. Gun, O. Lev, D. Aurbach, B. Markovsky, M.D. Levi, Adv. Mater., 10 (1998) 577.
17. M. Opallo, J. Kukulka-Walkiewicz, Electrochimica Acta, 46 (2001) 4235.
18. J. Niedziolka, M. Opallo, Electrochem. Commun., 5 (2003) 924.
19. A. Matsuda, M. Tatsumisago, T. Minami, J. Sol-Gel Sci. Technol., 19 (2000) 581.
20. U. Schubert, New J. Chem., 18 (1994) 1049.
21. L. Rabinovich, O. Lev, Electroanalysis, 13 (2001) 265.
22. J.L. Hedric, R.D. Miller, C.J. Hawker, K.R. Carter, W. Volksen, D.Y. Yoon, M. Trollsas, Adv. Mater., 10 (1998) 1049.
23. H. Fan, H.R. Bently, K.R. Kathan, P.Clem, Y. Lu, C.J. Brinker, J. Non-Crystal. Sol. 285 (2001) 79.
24. C. Sanchez, B. Julian, P. Belleville, M. Popall, J. Mater. Chem., 15 (2005) 3559.
25. A. Walcarius, D. Mandler, J.A Cox, M.M. Collinson, O. Lev, J. Mater. Chem., 15 (2005) 3663.
26. K.A. Andrianov, “Organic Silicone Compounds”, 1955.
27. M. Ebelmen, Ann. Chim. Phys., 15 (1845) 319.
28. D.I. Mendeleyev, Khim. Zhur. Sok. I Eng., 4 (1860) 65.
29. C.J. Brinker, G.W. Scherer “Sol-Gel Science. The Physics and Chemistry of Sol-Gel Processing“, Academic Press 1990.
30. D.J. Shaw, “Colloid and Surface Chemistry” 4th ed., 1992.
31. R. Aelion, A. Loebel, F. Erich, J. Am. Chem. Soc., 72 (1950) 5705.
32. A.C. Peirre, “Introduction to Sol-Gel Process”, Kluwer Academic Publisher 1998.

33. L. Nicole, C. Boissiere, D. Grosso, A. Quach, C. Sanchez, J. Mater. Chem., 15 (2005) 3598.
34. C. Sanchez, G.J. de A.A. Soler-Illia, F. Ribot, T. Lalot, C.R. Mayer, V. Cabuil, Chem. Mater., 13 (2001) 3061.
35. L.E. Scrive in "Better Ceramics Through Chemistry" 3rd ed. C.J. Brinker, D.E. Clark, D.R. Ulrich, 1988.
36. R. Shacham, D. Avnir, D. Mandler, Adv. Mater., 11 (1999) 384.
37. K.Gong, M. Zhang, Y. Yan, L. Su, L. Mao, S. Xiong, Y. Chen, Anal. Chem., 76 (2004) 6500.
38. P. Audebert, G. Cerveau, RJ.P. Corriu, N. Costa, J. Electroanal. Chem., 413 (1996) 89.
39. J. Puetz, G. Gasparro, M.A. Aegerter, Thin Solid Films, 442 (2003) 40.
40. S.E. Alexandrov, M. L. Hitchman, Chem. Vap. Deposition, 11 (2005) 457.
41. D. Vangeneugden, S. Paulussen, O. Goossens, R. Rego, K. Rose, Chem. Vap. Deposition 11 (2005) 491.
42. J. Wang, P.V.A. Pamidi, D. Su Park, Anal. Chem., 68 (1996) 2705.
43. D. Avnir, D. Levy, R. Reisfeld, J. Phys. Chem., 88 (1984) 5956.
44. K.S. Sing, D.H. Everett, R.A. Haul, L. Moscou, J. Pierotti, J. Rouquerol, T. Siemienewska, Pure Appl. Chem., 57 (1985) 603.
45. C.T. Kresge, M.E. Leonowicz, W.J. Roth, J.C. Vartuli, J.S. Beck, Nature, 359 (1992) 710.
46. G.J. de A.A. Soler-Illia, C. Sanchez, B. Labeau, J. Patarin, Chem. Rev., 102 (2002) 4093.
47. C. Sanchez, G.J. de A.A. Soler-Illia, F.Ribot, D. Grosso, C.R. Chim., 6 (2003) 1131.
48. W.J. Hunks, G.A. Ozin, J.Mater. Chem., 15 (2005) 3716.
49. D.A. Doshi, A. Gibaud, V. Goletto, M. Lu, H. Gerung, B. Ocko, S.M. Han, C.J. Brinker, J. Am. Chem. Soc, 125 (2003) 11646.
50. G.S. Attard, J.C. Glyde, C.G. Goltner, Nature, 378 (1995) 366.
51. N. Petkov, M. Holzl, T.H. Metzger, S. Mintova, T. Bein, J. Phys. Chem. B, 109 (2005) 4485.
52. T. Asefa, M.J. MacLachan, N. Coombs, G.A. Ozin, Nature, 402 (1999) 867.
53. Y.F.Lu, H.Y. Fan, N. Doke, D.A. Loy, R.A. Assink, D.A. LaVan, C.J. Brinker, J. Am. Chem. Soc., 122 (2000) 5258.
54. S.L. Burkett, S.D. Sims, S. Mann, Chem. Commun., (1996) 1367.
55. R. Burch, N. Cruise, D. Gleeson, S.C. Tsang, Chem. Commun., (1996) 951.
56. T. Maschmeyer, F. Rey, S. Gopinathan, J.M. Thomas, Nature, 378 (1995) 159.
57. D. Brunel, Micropor. Mesopr. Mater., 27 (1999) 329.
58. K. Moller, T. Bein, Chem. Mater., 10 (1998) 2950.
59. A. Stein, B.J. Melde, R.C. Schroden, Adv. Mater., 12 (2000) 1403.
60. A. Sayari, S. Hamoudi, Chem. Mater., 13 (2001) 3151.
61. J. Widera, A.M. Kijak, D.V. Ca, G.E. Pacey, R.T. Taylor, H. Perfect, J.A. Cox, Electrochim. Acta, 50 (2005) 1703.
62. X.Y. Bao, X.S. Zhao, S.Z. Qiao, S.K. Bhatia, J. Phys. Chem. B, 108 (2004) 16441.
63. J.Wange, G. Wu, J. Shen, T. Yang, Q. Zhang, B. Zhou, Z. Deng, J. Sol-Gel Sci. Technol., 18 (2000) 219.

64. C.J. Brinker, A.J. Hurd, P.R. Schunk, G.C. Frey, C.S. Ashley, J. Non-Crystal. Sol., 147&148 (1992) 424.
65. M.C. Goncalves, G.S. Attard, Rev. Adv. Mater. Sci., 4 (2003) 147.
66. S. Yu, T.K.S. Wong, X. Hu, K. Pita, Thin Solid Films, 462-463 (2004) 311.
67. S. Kumon, K. Nakanishi, K. Hirao, J. Sol-Gel Sci. Technol., 19 (2000) 553.
68. P.N. Deepa, M. Kanungo, G. Claycomb, P.M.A. Sherwood, M.M. Collinson, Anal. Chem., 75 (2003) 5399.
69. A.N. Khramov, J. Munos, M.M. Collinson, Langmuir, 17 (2001) 8112.
70. M. Kanungo, M.M. Collinson, Chem. Commun., 5 (2004) 548.
71. M. Kanungo, P.N. Deepa, M.M. Collinson, Chem. Mater., 16 (2004) 5535.
72. M.M. Collinson, N. Moore, P.N. Deepa, M. Kanungo, Langmuir, 19 (2003) 7669.
73. M. Hunnius, A. Rufinska, W.F. Maier, Micropor. Mesopor. Mater., 29 (1999) 389.
74. D.Y. Sasaki, T.M. Alam, Chem. Mater., 12 (2000) 1400.
75. R. Makote, M.M. Collinson, Chem. Mater., 10 (1998) 2440.
76. R. Makote, M.M. Collinson, Chem. Commun, (1998) 425.
77. S. Fireman-Shoresh, D. Avnir, S. Marx, Chem. Mater., 15 (2003) 3607.
78. R. Tamaki, Y. Chujo, K. Kuraoka, T. Yazawa, J. Mater. Chem., 9 (1999) 1741.
79. M.M. Collinson, H. Wang, R. Makote, A. Khramov, J. Elactroanal. Chem., 519 (2002) 65.
80. S. Sayen, A. Walcarius, Electrochem. Commun., 5 (2003) 341.
81. J.A.M. Sondag-Huethorst, L.G.J. Fokkink, Langumir, 11 (1995) 2237.
82. W.R. Thompson, M. Cai, M. Ho, J.E. Pemberton, Langmuir, 13 (1997) 2291.
83. J. Wang, P.V.A. Pamidi, D.R. Zanette, J. Am. Chem. Soc., 120 (1998) 5852.
84. R.J. Tremont, D.R. Blasini, C.R. Cabrera, J. Electroanal. Chem., 556 (2003) 147.
85. X. Chen, G.S. Wilson, Langmuir, 20 (2004) 8762.
86. C.A. Goss, D.H. Charych, M. Majda, Anal. Chem., 63 (1991) 85.
87. M. Tsionsky, G.Gun, V.Glezer, O. Lev, Anal. Chem., 66 (1994) 1747.
88. L. Rabinovich, O. Lev, Electroanalysis, 13 (2001) 265.
89. T. Hubert, A. Shimamura, A. Klyszcz, Material Science-Poland, Vol. 23, No. 1 (2005) 61.
90. K. Gong, M. Zhang, Y. Yan, L. Su, L. Mao, S. Xiong, Y. Chen, Anal. Chem., 76 (2004) 6500.
91. S. Sakkas, H. Kozuka, J. Sol-gel Sci. Technol., 13 (1998) 701.
92. P. Innocenci, H. Kozuka, J. Sol-gel Sci. Technol., 3 (1994) 229.
93. M. Menning, M. Schmitt, H. Shmitt, J. Sol-Gel Sci. Technol., 8 (1997) 1035.
94. C.C. Trapalis, M. Kokkoris, G. Pedikadis, G. Kordas, J. Sol-Gel Sci. Technol., 26 (2003) 1213.
95. B. Prieto-Simon, G.S. Armtas, P.J. Pomonis, C.G. Nanos, M.I. Prodromidis, Chem. Mater., 16 (2004) 1026.
96. R.F. Lane, A.T. Hubbard, J. Phys. Chem., 77 (1973) 1401.
97. R.W. Murray, Acc. Chem. Res., 13 (1980) 135.
98. L.L. Miller, M.R. Van De Mark, J. Am. Chem. Soc., 100 (1978) 639.
99. F.B. Kaufman, E.M. Engler, J. Am. Chem. Soc., 101 (1979) 547.

100. J.R. Lenhard, R.W. Murray, J. Am. Chem. Soc., 100 (1978) 7870.
101. A. Merz, A.J. Bard, J. Am. Chem. Soc., 100 (1978) 3222.
102. N. Oyama, F.C. Anson, J. Am. Chem. Soc., 101 (1979) 739.
103. P. Daum, R.W. Murray, J. Electroanal. Chem., 103 (1979) 289.
104. J.R. Lenhard, R.W. Murray, J. Electroanal. Chem., 78 (1977) 195.
105. P. Audebert, P. Griesmar, C. Sanchez, J. Mater. Chem., 1 (1991) 699.
106. A. Walcarius, Chem. Mater., 13 (2001) 3351.
107. A. Walcarius, Electroanalysis, 13 (2001) 701.
108. O. Lev, Z. Wu, S. Bharathi, V. Gleser, A. Modestov, J. Gun, L. Rabinovich, S. Sampath, Chem. Mater., 9 (1997) 2354.
109. O. Dvorak, M.K. De Armond, J. Phys. Chem. 97 (1993) 2646.
110. M.E. Tess, J.A. Cox, Anal. Chem., 70 (1998) 187.
111. S.D. Holstrom, J.A. Cox, Electroanalysis, 10 (1998) 597.
112. M.M. Collinson, C.G. Rausch, A. Voigt, Langumir, 13 (1997) 7245.
113. R. Makote, M.M. Collinson, Anal. Chimica Acta, 394 (1999) 195.
114. F. Tian, G. Zhu, Sensor and Actuators B, 97 (2004) 130.
115. W. Song, Y. Liu, N. Lu, H. Xu, C. Sun, Electrochimica Acta, 45 (2000) 1639.
116. Y. Guo, A.R. Guadalupe, J. Pharm. Biomed. Anal., 19 (1999) 175.
117. S. Sayen, A. Walcarius, J. Electroanal. Chem., 581 (2005) 70.
118. P.C. Pandey, S. Upadhyay, H.C. Pathak, C.M.D. Pandey, Electroanalysis 11 (1999) 950.
119. J. Wang, M.M. Collinson, J. Electroanal. Chem., 455 (1998) 127.
120. C.C. Hsueh, M.M. Collinson, J. Electroanal. Chem., 420 (1997) 243.
121. H. Wei, M.M. Collinson, Anal. Chimica Acta, 397 (1999) 113.
122. P. Tien, L.K. Chau, Y.T.Y. Shieh, W.C. Lin, G.T. Wei, Chem. Mater., 13 (2001) 1124.
123. K. Kimura, S. Yajima, H. Takase, M. Yokoyama, Y. Sakurai, Anal. Chem., 73 (2001) 1605.
124. AN. Khramov, M.M. Collinson, Anal. Chem., 72 (2000) 2943.
125. M.D. Petit-Dominguez, H. Shen, W.R. Heineman, C. Seliskar, Anal. Chem., 69 (1997) 703.
126. A. Liu, H. Zhou, I. Honma, Electrochem Commun., 7 (2005) 1.
127. D. Avnir, S. Braun, O. Lev, M. Ottolenghi, Chem. Mater., 6 (1994) 1605.
128. J. Wang, Anal. Chim. Acta, 399 (1999) 21.
129. K. Ogura, K. Nakaoka, M. Nakayama, M. Kobayashi, A. Fujii, Anal. Chimica Acta, 384 (1999) 219.
130. I. Zawisza, J. Rogalski, M. Opallo, J. Electroanal. Chem, 588 (2006) 244.
131. S.C. Barton, H.H. Kim, G. Binyamin, Y.C. Zhang, A. Heller, J. Am. Chem. Soc., 123 (2001) 5802.
132. W.E. Farneth, M.B. D'Amore, J. Electroanal. Chem., 581 (2005) 197.
133. F. Marken, R.D. Webster, S.D. Bull, S.G. Davies, J. Electroanal. Chem. 437 (1997) 209.
134. S.J. Stott, K.J. McKenzie, R.J. Mortimer, C.M. Hayman, B.R. Buckley, P.C. Bulman Page, F. Marken, G. Shul, M. Opallo, Anal. Chem., 76 (2004) 5364.
135. F. Scholz,, R. Gulaboski, Chem. Phys. Chem., 6 (2005) 16.

136. R.W. Murray, in Electroanalytical Chemistry, ed. A.J. Bard, Marcel Dekker, New York, 1987, vol. 13, p. 191 and references therein.
137. C.E. Banks, T.J. Davies, R.G. Evans, G. Hignett, A.J. Wain, N.S. Lawrence, J.D. Wadhawan, F. Marken, R.G. Compton, Phys. Chem. Chem. Phys., 5 (2003) 4053.
138. F. Scholz, U. Schröder, R. Gulaboski „Electrochemistry of Immobilized Particles and Droplets“, Springer 2005.
139. P. Tasakorn, J. Chen, K. Aoki, J. Electroanal. Chem., 533 (2002) 119.
140. F. Scholz, R. Gulaboski, Chem. Phys. Chem., 5 (2004) 1.
141. T.J. Davies, S.J. Wilkins, R.G. Compton, J. Electroanal. Chem., 586 (2006) 260.
142. F. Marken, A. Blythe, R.G. Compton, S.D. Bull, S.G. Davies, Chem. Commun., (1999) 1823.
143. J.D. Wadhawan, A.J. Wain, A.N. Kirham, D.J. Walton, B.Wood, R.R. France, S.D. Bull, R.G. Compton, J. Am. Chem. Soc., 125 (2003) 11418.
144. J.D. Wadhawan, R.G. Evans, R.G. Compton, J. Electroanal. Chem., 533 (2002) 71.
145. A.J. Wain, J.D. Wadhawan, R.R. France, R.G. Compton, Phys. Chem. Chem. Phys., 6 (2004) 836.
146. A.J. Wain, J.D. Wadhawan, R.G. Compton, Chem. Phys. Chem., 4 (2003) 974.
147. F. Scholz, S. Komorsky-Lovrić, M. Lovrić, Electrochem. Commun., 20 (2000) 112.
148. F. Scholz, R. Gulaboski, K. Caban, Electrochem. Commun., 5 (2003) 929.
149. R. Gulaboski, F. Scholz, J. Phys. Chem. B, 107 (2003) 5650.
150. J.D. Wadhawan, R.G. Evans, C.E. Banks, S.J. Wilkins, R.R. France, N.J. Oldham, A.J. Fairbanks, B. Wood, D.J. Walton, U. Schröder, R.G. Compton, J. Phys. Chem. B, 106 (2002) 9619.
151. M. Donten, Z. Stojek, F. Scholz, Electrochem. Commun., 4 (2002) 324.
152. J.C. Ball, F. Marken, Q. Fulian, J.D. Wadhawan, A.N. Blythe, U. Schröder, R.G. Compton, S.D. Bull, S.G. Davies, Electroanalysis, 12 (2000) 1017.
153. E. Bak, M. Donten, Z. Stojek, Electrochem. Commun., 7 (2005) 483.
154. E. Bak, M.L. Donten, M. Donten, Z. Stojek, Electrochem. Commun., 7 (2005) 1098.
155. M.J. Weaver, F.C. Anson, J. Electroanal. Chem., 58 (1975) 95.
156. C. Shi, F.C. Anson, Anal. Chem., 70 (1998) 3114.
157. C. Shi, F.C. Anson, J. Phys. Chem. B., 102 (1998) 9850.
158. H.O. Shafer, T.L. Derback, C.A. Koval, J. Phys. Chem., 104 (2000) 1025.
159. R. Gulaboski, V. Mirceski, C.M. Pereira, M.N.D.S. Cordeiro, A.F. Silva, F. Quentel, M. L'Her, M. Lovric, Langmuir, 22 (2006) 3404.
160. A.L. Baker, P.R. Unwin, J. Phys. Chem. B, 104 (2000) 2330.
161. B. Steiger, F.C. Anson, Inorg. Chem., 39 (2000) 4579.
162. T.D. Chung, F.C. Anson, J. Electroanal. Chem., 508 (2001) 115.
163. J.D. Wadhawan, U. Schröder, A. Neudec, S.J. Wilkins, R.G. Compton, F. Marken, C.S. Consorti, R.F. de Suza, J. Dupont, J. Electroanal. Chem., 493 (2000) 75.
164. M.C. Buzzeo, R.G. Evans, R.G. Compton, Chem. Phys. Chem., 5 (2004) 1106.
165. “Electrochemical Aspects of Ionic Liquid” Ed. By H. Ohno, Jon Wiley & Sons, 2005.

166. J. Zhang, A.M. Bond, Analyst, 130 (2005) 1132.
167. K.A. Fletcher, I.A. Storey, A.E. Hendricks, S. Pandey, S. Pandey, Green Chem., 3 (2001) 210.
168. J.G. Huddleston, A.E. Visser, W.M. Reichert, H.D. Willauer, G.A. Broker, R.D. Rogers, Green Chem., 3 (2001) 156.
169. R.G. Evans, O.V. Klymenko, C. Hardacre, K.R. Seddon, R.G. Compton, J. Electroanal. Chem. 556 (2003) 179.
170. R.P. Swatloski, J.D. Holbrey, R.D. Rogers, Green Chem., 5 (2003) 361.
171. M.C. Buzzeo, O.V. Klymenko, J.D. Wadhawan, C. Hardacre, K.R. Seddon, R.G. Compton, J. Phys. Chem. A, 107 (2003) 8872.
172. I.M. Alnashef, M.L. Leonard, M.A. Matthews, J.W. Weidner, Electrochem. Solid-State Lett., 4 (2001) D16.
173. M.C. Buzzeo, D. Giovanelli, C. Hardacre, K.R. Seddon, R.G. Compton, Electroanalysis 16 (2004) 888.
174. Y. Katayama, S. Dan, T. Miura, T. Kishi, J. Electrochem. Soc., 144 (2001) C 102.
175. P.Y. Chen, I.W. Sun, Electochim. Acta, 45 (1999) 441.
176. F. Endres, Phys. Chem. Chem. Phys., 3 (2001) 3165.
177. I. Mukhopadhyay, W. Freyland, Langumir, 19 (2003) 1951.
178. H. Randriamahazaka, C. Plesse, D. Teyssie, C. Chevrot, Electrochem. Commun., 5 (2003) 613.
179. R.F. de Souza, J.C. Padilha, R.S. Goncalves, J. Dupont, Electrochem. Commun., 5 (2003) 728.
180. R. Maminska, A. Dybko, W. Wroblewski, Sensors and Actuators B, 115 (2006) 552.
181. C. Coll, R. H. Labrador, R.M. Manez, J. Soto, F. Sancenon, M.J. Segui, E. Sanchez, Chem. Commun., (2005) 3033.
182. J.D. Wadhawan, U. Schröder, A. Neudeck, S.J. Wilkins, R.G. Compton, F. Marken, C.S. Consorti, R.F. De Souza, J. Dupont, J. Electroanal. Chem., 493 (2000) 75.
183. B.M. Quinn, Z. Ding, R. Moulton, A.J. Bard, Langmuir, 18 (2002) 1734.
184. K. Tanaka, N. Nishi, T. Kakiuchi, Anal. Sci., 20 (2004) 1553.
185. T. Kakiuchi, N. Tsujioka, Electrochem. Commun., 5 (2003) 159.
186. E. Rozniecka, G. Shul, J. Siriex-Plenet, L. Gaillon, M. Opallo, Electrochem. Commun., 7 (2005) 299.
187. G. Shul, J. Sirieix-Plenet, L. Gaillon, M. Opallo, Electrochem. Commun., 8 (2006) 1111.
188. P.W. Atkins "Physical Chemistry" Oxford University Press 1994.
189. R.G. Greenler, J. Chem. Phys., 44 (1966) 310.
190. J.I. Paredes, A. Martinez-Alonso, J.M.D. Tascon, Micropor. Mesopor. Mater., 65 (2003) 93.
191. E. Meyer "Progress in Surface Science" vol. 41 p 3 Parmagedon Press Ltd. 1992.
192. "Introduction to Nanoscale Science and Technology" Springer 2004.
193. H. Hug, University of Basel, lecture on ESONN, Grenoble, France 2005.
194. R. Jonhson "An introduction to ESEM" 1996 Philips Electron Optics.
195. http: // www.mse.iastate.edu/microscopy/path2
196. A.J. Bard „Electrochemical Methods. Fundamentals and Applications.", J. Wiley & Sons 2001.

197. F. Scholz (Ed.) “Electroanalytical methods. Guide to Experiments and Applicatons”, Springer 2002.
198. H.H. Girault “ Analytical and Physical Electrochemistry” EPFL Press 2004.
199. M. Tsionsky, G. Gun, V. Glezer, O. Lev, Anal. Chem. 66 (1994) 1747.
200. G. Shul, M. Saczek-Maj, M. Opallo, Electroanalysis, 16 (2004) 1254.
201. H.K. Bottcher, H. Kallies, H.Haufe, J.Seidel, Adv. Mater., 11 (1999) 138.
202. R.G. Nuzzo, D.I.Allara, J. Chem. Soc., 105 (1983) 4481.
203. K. Sekimoto, T. Matsubara, Phys. Rev. B, 26 (1982) 3411.
204. R. M. Almeida, Phys. Rev. B, 45 (1992) 161.
205. E. I. Kamitsos, A. P. Patsis G. Kordas, Phys. Rev. B, 48 (1993) 12499.
206. R. M. Almeida, Phys. Rev. B, 53 (1996) 14656.
207. E. I. Kamitsos, Phys. Rev. B, 53 (1996) 14659.
208. R. Brito, V.A. Rodriguez, J. Figueroa, C.R. Cabrera, J. Electroanal. Chem., 520 (2002) 47.
209. X. Chen, G.S. Wilson, Langmuir, 20 (2004) 8762.
210. D. Brassard, M.A. El Khakani, J. Appl. Phys., 98 (2005) 054612.
211. K.J. McKenzie, F. Marken, X. Gao, S.C. Tsang, K.Y. Tam, Electrochem. Commun., 5 (2003) 286.
212. M.M. Collinson, N. Moore, P.N. Deepa, M. Kanungo, Langmuir, 19 (2003) 7669.
213. M.M. Collinson, P. Zambrano, H. Wang, J. Taussig, Langmuir, 15 (1999) 662.
214. R. Szamocki, S. Reculusa, S. Ravaine, P.N. Bartlett, A. Kuhn, R. Hempelmann, Angew. Chem. Int. Ed., 45(2006) 1317.
215. S. Dietz, W.L. Bell, R.L. Cook, J. Organomet. Chem., 545-546 (1997) 67.
216. A.D. Ryabov, E.S. Ryabova, M.D. Reshetova, J. Organomet. Chem., 637-639 (2001) 469.
217. J.R. Pladzewicz, J.H. Espenson, J. Am. Chem. Soc., 95 (1973) 56.
218. G. Denault, M.V. Mirkin, A.J. Bard, J. Electroanal. Chem., 308 (1991) 27.
219. B.R. Scharifker, J. Electroanal. Chem., 240 (1988) 61.
220. S.L. Petersen, D.E. Tallman, Anal. Chem., 62 (1990) 459.
221. G. Shul, K.J. McKenzie, J. Niedziolka, E. Rozniecka, B. Palys, F. Marken, C.M. Hayman, B.R. Buckley, P.C. Bulman Page, M. Opallo, J. Electroanal. Chem., (2005).
222. R.A. Petersen, D.H. Evans, J. Electroanal. Chem., 222 (1987) 129.
223. W.R. Fawcett, M. Fedurco, M. Opallo, J. Phys. Chem., 96 (1992) 9959.
224. S. Komorosky-Lovric, M. Lovric, F. Scholz, J. Electroanal. Chem., 508 (2001) 129.

9. List of papers, which have evolved from doctoral thesis

1. "Stabilising electrode | redox liquid | aqueous solution system with hydrophobic silicate film."
   J. Niedziółka, M. Opałło
   Electrochem. Commun., 6 (2004) 475-479.

2. „ Hydrophobic silicate sol-gel films for biphasic electrodes and porotrodes."
   K.J. McKenzie, J. Niedziółka, C.A. Paddon, F. Marken, E. Rożniecka, M. Opałło
   The Analyst, 129 (12) (2004) 1181-1185.

3. "Characterisation of Biphasic Electrodes based on the Liquid N,N-didodecyl-N'N'-diethylphenylenediamine Redox System Immobilised on Porous Hydrophobic Silicates and Immersed in Aqueous Media."
   G. Shul, K.J. McKenzie, J. Niedziółka, E. Rożniecka, B. Pałys, F. Marken, C.M. Hayman, B.R. Buckley, P.C. Bulman Page, M. Opałło
   Journal of Electroanal. Chem., 582 (2005) 202-208.

4. "Characterisation of gold electrodes modified with methyltrimethoxysilane and (3-mercaptopropyl) trimethoxysilane sol-gel processed films."
   J. Niedziółka, B. Pałys, R. Nowakowski, M. Opałło
   Journal of Electroanal. Chem., 578 (2) (2005) 239-245.

5. „Ion transfer processes at ionic liquid based redox active drop deposited on the electrode surface."
   J. Niedziółka, E. Rożniecka, J. Stafiej, J. Sirieix-Plenet, L. Gaillon, D. di Caprio, M. Opałło
   Chem. Commun., (2005) 2954-2956.

6. „Ion transfer processes at the room temperature ionic liquid | aqueous solution interface supported by a hydrophobic carbon nanofibers – silica composite film."
   E. Rożniecka, J. Niedziółka, J. Sirieix-Plenet, L. Gaillon, M.A. Murphy, F. Marken, M. Opałło
   Journal of Electroanal. Chem., 587 (2006) 133-139.

7. "Characterisation of Hydrophobic Carbon Nanofiber - Silica Composite Film Electrodes For Redox Liquid Immobilisation."
   J. Niedziółka, M.A. Murphy, F. Marken, M. Opałło
   Electrochimica Acta, in press.

8. "Changing the Direction of Ion Transfer Across o-Nitrophenyloctylether | Water Interface Coupled to Electrochemical Redox Reaction."
   J. Niedziółka, E. Rożniecka, J. Chen, M. Opałło
   Electrochem. Commun., 8 (2006) 941-945.